

UC San Diego

UC San Diego Electronic Theses and Dissertations

Title

Singularities of non-Hermitian Photonic Systems and their Applications

Permalink

<https://escholarship.org/uc/item/8hp3f8m0>

Author

Kodigala, Ashok

Publication Date

2017

Peer reviewed|Thesis/dissertation

UNIVERSITY OF CALIFORNIA, SAN DIEGO

Singularities of non-Hermitian Photonic Systems and their Applications

A dissertation submitted in partial satisfaction of the requirements for the degree Doctor
of Philosophy

in

Electrical Engineering (Photonics)

by

Ashok Kodigala

Committee in charge:

Professor Boubacar Kanté, Chair
Professor Anna Devor
Professor Yeshaiahu Fainman
Professor Shayan Mookherjea
Professor George Papen
Professor Justin Roberts

2017

Copyright ©

Ashok Kodigala, 2017

All rights reserved.

The dissertation of Ashok Kodigala is approved, and it is acceptable in quality and form for publication on microfilm and electronically:

Chair

University of California, San Diego
2017

DEDICATION

To my family

◦

EPIGRAPH

I am always doing that which I cannot do, in order that I may learn how to do it.

-Pablo Picasso

TABLE OF CONTENTS

Signature Page	iii
Dedication	iv
Epigraph	v
Table of Contents	vi
List of Figures	viii
List of Tables	x
Acknowledgments	xi
Vita	xiv
Abstract of the Dissertation	xvi
Chapter 1 Introduction	1
1.1 Exceptional Points (EPs)	1
1.2 Bound States in the Continuum (BICs)	2
1.3 Outline of Dissertation	3
References	4
Chapter 2 Resonance Dynamics of Plasmon Hybridized Systems	6
2.1 Introduction	6
2.2 Effective Hamiltonian	7
2.3 Mode Symmetries of Hybridized Shift-bar System	9
2.4 S-Parameters and Rational Fitting	10
2.5 Inversion Point and Degree of Inversion	13
2.6 Static Dipole Approximation	15
2.7 Negative Coupling Regime	19
2.8 Concluding Remarks	20
References	22
Chapter 3 Exceptional Points (EPs) in Three-Dimensional Plasmonic Nanostructures ...	25
3.1 Introduction	25
3.2 Mode Symmetries of Hybridized Three-bar System	26
3.3 Exceptional Point in Three-bar System	32
3.4 Residue Divergence at EP	33
3.5 EPs with Multiple ($N > 1$) Coupled Resonators and Five-bar System	34
3.6 Concluding Remarks	36
References	37
Chapter 4 Lasing from Photonic Bound States in the Continuum (BICs)	40
4.1 Introduction	40
4.2 BIC Cavity Design	42
4.3 Diverging Quality Factor (Q) at BIC Singularity	43
4.4 Device Characterization	47
4.5 Lasing from an Optically Pumped BIC Cavity	48

4.6 Robustness and Scaling of BIC Lasers	49
4.7 Lasing Threshold at BIC Singularity	50
4.8 Threshold Power Density versus Cavity Size.....	51
4.9 Linewidth of BIC Lasers.....	53
4.10 Concluding Remarks.....	55
References.....	56
Chapter 5 Nanofabrication of Suspended PhC Lasing Membranes of InGaAsP Cylinders	60
5.1 Introduction.....	60
5.2 Device Fabrication	62
A. Method I (HSQ Hard Mask).....	63
B. Method II (HSQ with Chrome Hard Mask).....	66
5.3 Results and Discussion	68
5.4 Device Performance.....	76
5.5 Concluding Remarks.....	77
References.....	79
Chapter 6 Summary and Outlook	82
Appendix A (Ch 2).....	85
A.1 S-parameters and eigenvalues of shift-bar (two-bar) system.....	85
Appendix B (Ch 3).....	92
B.1 S-parameters and eigenvalues of three and five-bar systems with EPs	92
References.....	96
Appendix C (Ch 4).....	97
C.1 Odd and Even Modes	97
C.2 Group Theory and Tunable off- Γ BICs.....	98
C.3 Far-field Emission and Polarization of BIC Lasers	100
C.4 Emission Power Estimate.....	104
References.....	105

LIST OF FIGURES

Figure 2.1: (a) Two-port schematic of an optical resonator system with \mathbf{S}^+ (incoming waves) and \mathbf{S}^- (outgoing waves). (b) Block diagram representation of the scattering matrix in terms of the effective Hamiltonian, \mathbf{H}_{eff}	8
Figure 2.2: (a) Physical setup of paired gold bars separated by a dielectric (SiO_2) spacer with dimensions: $L=450$ nm, $W=50$ nm, $t=40$ nm, $p_y=400$ nm, $\epsilon_{\text{sub}}=2.25$ (permittivity of oxide), and variable parameter: h_{sub} , p_x , dx	10
Figure 2.3: Simulated transmission, $ S_{21} ^2$, and reflection, $ S_{11} ^2$, spectra (solid curve) and their rational fits (dots) for $p_x=800$ nm, $h_{\text{sub}}=100$ nm, and $dx=0$	12
Figure 2.4: Simulated absorption, $1- S_{11} ^2- S_{21} ^2$, spectra (solid curve) and its rational fit (dots) for the case above: $p_x=800$ nm, $h_{\text{sub}}=100$ nm, and $dx=0$	12
Figure 2.5: Reflection spectra, $ S_{11} ^2$, as a function of shift ‘ dx ’ for $p_x=900$ nm and $h_{\text{sub}}=75$ nm (a) and corresponding resonant frequencies acquired via rational fitting (b).	14
Figure 2.6: (a) Interaction energy between two dipoles in the symmetric and anti-symmetric configuration.	17
Figure 2.7: (a) Evolution of resonant frequencies as a function of shift, dx , with linewidths pertaining to (b) symmetric and (c) anti-symmetric modes for shift-bar system with dimensions $p_x=1000$ nm and $h_{\text{sub}}=50$ nm.	18
Figure 2.8: (a) Resonant frequencies of shift-bar system acquired via rational fitting (dots) and resonant frequencies from Hamiltonian Model (solid) for the symmetric (red) and anti-symmetric (blue) modes.	20
Figure 3.1: (a) Physical setup of a unit cell with three paired gold bars, with the middle one separated by a variable distance (dx , dy , dz) with respect to the other two.....	28
Figure 3.2: Resonance information in the form of complex poles extracted from scattering parameters and plotted as a function of shift ‘ dx ’ (middle-bar) for $P_x=800$ nm and $dz=60$ nm.	30
Figure 3.3: Resonances approaching an exceptional point (black \blacksquare) plotted in the complex plane ($\gamma+j\omega$) for modes A (\circ) and C (\square) as a function of ‘ dx ’	33
Figure 3.4: Residues of the corresponding modes A (\circ) and C (\square) as a function of shift, dx ,	34
Figure 3.5: Realization of an exceptional point in a system with 5 bars ($2n+1$ with $n=2$) with top, middle and bottom bars shifted by dx	36
Figure 4.1: (a) Tilted electron micrograph of InGaAsP multiple quantum wells cylindrical nanoresonator array suspended in air.....	43
Figure 4.2: (a) Quality factor of high- Q modes at the Γ point around the telecommunication wavelength for different nanoresonator radii.....	46
Figure 4.3: (a) Micro-photoluminescence (PL) setup used to measure laser emission from BIC lasers.....	47

Figure 4.4: (a) Evolution of the normalized output power as a function of both wavelength (μm) and pump power (μW) for a 16-by-16 array with a nanoresonator radius of 525 nm.	49
Figure 4.5: (a) Electron micrographs of fabricated BIC lasers of size 8-by-8, 10-by-10, 16-by-16, and 20-by-20. (b) Lasing wavelength as a function of nanoresonator radius 50	
Figure 4.6: Measured laser threshold power as a function of radii for the lasers clearly shows a minimum ($56 \mu\text{W}$) close to R_{opt} (about 525 nm) reflecting the maximum quality factor around the BIC singularity	51
Figure 4.7: Lasing threshold power densities, P_{th} ($\mu\text{W}/\mu\text{m}^2$), as a function of laser array size, N , for a given resonator radius ($R=530 \text{ nm}$).....	52
Figure 4.8: (a) Lasing linewidths for devices with varying radii at pump powers above threshold (blue markers).	54
Figure 4.9: (a) Linewidth evolution of a laser away from BIC point as a function of pump power in linear scale and (b) log scale with a threshold of $\sim 62 \mu\text{W}$	55
Figure 5.1: (a) Schematic of epitaxially grown InGaAsP layers on InP substrate with nine quantum wells (in red).	63
Figure 5.2: Device fabrication process without a metal hard mask starting with the epitaxially grown multiple quantum wells on InP substrate and ending with the nanocylinders suspended membrane (a-g).....	65
Figure 5.3: Device fabrication process involving a metal hard mask, starting with the epitaxially grown multiple quantum wells on InP substrate (a-f).....	68
Figure 5.4: Electron micrograph images of Reactive Ion Etching (RIE) of InGaAsP/InP test patterns.	70
Figure 5.5: Reduction in bridge widths, W , from the nominal bridge widths as a function of the nominal radius	71
Figure 5.6: Etch requirements and optimization of membrane release. (a) Dependence of InP dry-etch depth on the crystallographic selective wet-etching of InP.	74
Figure 5.7: Electron micrograph images of completed membrane structures with 10x10 cylindrical resonators interconnected by a network of bridges with a visible etch pit below in the InP substrate	75
Figure 5.8: Lasing from fully suspended devices fabricated using a HSQ hard mask (a) and a Cr hard mask (b).....	77

LIST OF TABLES

Table 5.1: Original dimensions of bridge widths and radii defined for HSQ and Cr processes	70
Table 5.2: Summary of wet etch windows and their dimensions for membrane release..	73

ACKNOWLEDGMENTS

I am extremely grateful for my time spent here at UC San Diego. During this time, I have had the privilege of working with and learning from many highly talented individuals. First, I would very much like to thank my advisor, Professor Boubacar Kanté, for his guidance, support, and resolute encouragement through the many challenges over the years. With only a shared interest in nanophotonic research, I started as the first student of Prof. Kanté unsure of what the future held. I remember the early years to be what seemed like a never-ending uphill battle involving everything from setting up the lab to conducting research on multiple challenging projects. In hindsight, having accomplished more than I could have imagined, our shared struggle together seems well worth it.

I would also like to thank my other committee members, Prof. Shaya Fainman for his fruitful advise and support through various stages of my research. Prof. George Papen for initially taking me on as a student, advising me on laser research along with teaching intellectually rewarding courses on lasers and statistical optics. Prof. Shayan Mookherjea for his broadly encompassing courses on silicon photonics and our many interactions over the years. Prof. Anna Devor and Justin Roberts for fruitful discussions on the utility of my research in various other fields.

I have many to thank due to the interdisciplinary nature of my research. I owe a great deal of thanks to Thomas Lepetit for his mentorship and useful feedback on research over the years. Thanks to Qing Gu for our many discussions on fabrication. I would also like to thank the nano3 staff (Larry Grissom, Ivan Harris, Ryan Anderson, Sean Parks, Xuekun Lu) for their help in the cleanroom over the years. A special thanks to Maribel

Montero for the many nanolithography writing jobs. I would also like to thank my many colleagues in the group: LiYi Hsu, Babak Bahari, Junhee Park, Ricardo Tellez-Limon, Wanwoo Noh, Jeongho Ha, Matthieu Dupré, and Abdoulaye Ndao.

Lastly, a million thanks to Julie Moritz for helping me with the countless orders in building the lab, from computers to lab equipment.

Of course, none of this would have been possible without the love and undying support of my parents, Mitra and Subba, and my younger brother, Sri.

Chapter 2, in part, is a reprint of the material as it appears in A. Kodigala, T. Lepetit, and B. Kanté, "Engineering resonance dynamics of plasmon hybridized systems," *Journal of applied physics* **117**, 023110 (2015). The dissertation author was the primary researcher and author of this paper.

Chapter 3, in part, is a reprint of the material as it appears in A. Kodigala, T. Lepetit, and B. Kanté, "Exceptional points in three-dimensional plasmonic nanostructures," *Physical Review B* **94**, 201103(R) (2016). The dissertation author was the primary researcher and author of this paper.

Chapter 4, in part, is a reprint of the material as it appears in A. Kodigala, T. Lepetit, Q. Gu, B. Bahari, Y. Fainman and B. Kanté, "Lasing action from photonic bound states in the continuum," *Nature* **541**, 196 (2017). The dissertation author was the primary researcher and author of this paper.

Chapter 5, in part, is a reprint of the material as it appears in A. Kodigala, Q. Gu, T. Lepetit, B. Bahari, and B. Kanté, "Mechanically stable conjugate and suspended lasing membranes of bridged nano-cylinders," *Optical Materials Express* **7**, 2980 (2017). The dissertation author was the primary researcher and author of this paper.

Appendix C, in part, is a reprint of the material as it appears in the supplement of A. Kodigala, T. Lepetit, Q. Gu, B. Bahari, Y. Fainman and B. Kanté, "Lasing action from photonic bound states in the continuum," *Nature* **541**, 196 (2017). The dissertation author was the primary researcher and author of this paper.

VITA

- 2017 Doctor of Philosophy, Electrical Engineering (Photonics),
University of California, San Diego
USA
- 2013 Master of Science, Electrical Engineering (Electronics & Photonics),
University of California, Santa Barbara
USA
- 2011 Bachelor of Science, Electrical Engineering,
University of California, Santa Barbara
USA

JOURNAL PUBLICATIONS

A. Kodigala, Q. Gu, T. Lepetit, B. Bahari, and B. Kanté, “Mechanically stable conjugate and suspended lasing membranes of bridged nano-cylinders,” *Optical Materials Express* **7**, 2980 (2017).

A. Kodigala, T. Lepetit, Q. Gu, B. Bahari, and B. Kanté, “Lasing action from photonic bound states in the continuum,” *Nature* **541**, 196 (2017).

A. Kodigala, T. Lepetit, and B. Kanté, “Exceptional points in three-dimensional plasmonic nanostructures,” *Physical Review B* **92**, 201103(R) (2016).

A. Kodigala, T. Lepetit, and B. Kanté, “Engineering resonance dynamics of plasmon hybridized systems,” *Journal of Applied Physics* **117**, 023110 (2015).

J. Park, **A. Kodigala**, A. Ndao, and B. Kanté, “Hybridized metamaterial platform for nano-scale sensing,” *Optics Express* **25**, 15590 (2017).

A. Chen, **A. Kodigala**, T. Lepetit, and B. Kanté, “Multipoles of even/odd split-ring resonators,” *Photonics* **2**, 883 (2016).

ABSTRACT OF THE DISSERTATION

Singularities of non-Hermitian Photonic Systems and their Applications

by

Ashok Kodigala

Doctor of Philosophy in Electrical Engineering (Photonics)

University of California, San Diego, 2017

Professor Boubacar Kanté, Chair

The following dissertation focuses on a new class of devices based on singularities of non-Hermitian photonic systems for applications pertaining to sensing and lasing. These are systems with electromagnetic resonances that exhibit peculiar behavior. One in which multiple resonances of shared symmetry coalesce to form so called Exceptional Point (EP) singularities. Systems at EPs are known to be highly sensitive to environmental perturbations making them conducive for sensing applications. The first half of this dissertation is centered on investigating resonance dynamics of plasmonic nanostructures, comprised of metallic nano-particles, as they have the ability to confine light to an extremely small space (*i.e.* sub-wavelength) which in turn helps detect particles of

equivalent size. Herein, a framework for designing EPs in coupled metallic nano-particle arrays is presented. The latter half is centered on another type of peculiarity in which a resonance lifetime in a cavity diverges to infinity (i.e. infinite quality factor). These are resonance states that defy conventional wisdom by remaining localized, or bound, to a cavity while residing in a continuum of radiating or leaky states. These singularities are appropriately termed Bound States in the Continuum (BICs). This dissertation presents the first experimental demonstration of a BIC laser. It is constructed on a III-V semiconductor material platform (InGaAsP) which emits in the telecommunication band ($\sim 1.55 \mu\text{m}$) and operates at room temperature. This laser is intrinsically low threshold (*i.e.*, power efficient) and can be compact in size. It offers some unique and useful properties in terms of its tunability in emission wavelength and emission angle. It has the ability to naturally generate vector beams and the potential for high-power emission. A brief discussion on challenges to real-world applications is provided for these technologies.

Chapter 1

Introduction

Most physical systems are open or non-conservative in nature meaning they are free to exchange energy with their environment in the form of radiation and absorption. This is in contrast with closed systems where energy remains in the system and the system deemed conservative. Resonances of open and closed systems can be modeled with a Hamiltonian formalism from non-Hermitian quantum mechanics [1, 2]. In Hermitian or closed systems, eigenmodes do not decay and their eigenvalues are real. However, in non-Hermitian or open systems, eigenmodes can decay or grow and consecutively their eigenvalues are complex [1]. It is the singularities or peculiar behavior of these non-Hermitian systems that are primarily of interest as they yield interesting applications for sensing and lasing. Two such singularities called Exceptional Points (EPs) and Bound States in the Continuum (BICs) described below are the focus of this dissertation.

1.1 Exceptional Points (EPs)

EPs are special singularities of systems described by non-Hermitian Hamiltonians. At an EP, at least two eigenfrequencies and their corresponding eigenstates truly coalesce to become one [3, 4]. EPs are ubiquitous in physics, having been demonstrated in various fields such as quantum mechanics, acoustics, and photonics. They are highly sensitive to

external perturbations as even a minute variation will lift the degeneracy and cause splitting of both resonant frequencies and linewidths. As such, EP based nanophotonic devices are highly conducive for sensing applications with enhanced sensitivity [5]. Recent experimental demonstration of EPs on nanophotonic platforms such as whispering gallery mode micro-toroid cavities [6] and micro-ring resonator systems [7] has energized the topic. However, an experimental realization of an EP in a plasmonic platform is yet to be done. Sensing with plasmonics, or metallic nano-particles, can benefit from large field enhancements and the ability to control light at a sub-wavelength scale. The work presented in the first half of this dissertation explores a plasmonic shift-bar system, originally used for the demonstration of negative refraction or negative index media [8, 9], as the basis for plasmonic EPs for sensing.

1.2 Bound States in the Continuum (BICs)

Different from EPs, BICs are peculiar states that manifest themselves as resonances that do not decay. These resonances defy conventional wisdom as they remain confined, or bound, to a cavity while residing in a continuum of radiating or leaky states. They were first explored mathematically by von Neumann and Wigner in 1929 at the advent of quantum mechanics [10]. Since then BICs have been shown to occur in physical systems in many areas of physics including acoustics, microwaves and very recently in photonics [11-13]. BIC cavities are intrinsically high quality (Q) factor cavities have the potential to function as laser cavities. However, they were strictly limited to passive systems and have not been realized in active systems for lasing until the work in this dissertation. The inspiration for our work started with investigation of resonances in high-permittivity

subwavelength dielectric cylindrical resonators in the microwave domain [14, 15]. The lasers experimentally demonstrated here are based on resonance trapped BIC modes different from symmetry protected BICs, both of which exist in photonic crystal slabs [16, 17]. These resonance trapped BIC lasers are constructed on a III-V semiconductor material platform (InGaAsP) and are optically pumped. They emit in the telecommunication band ($\sim 1.55 \mu\text{m}$) and operate at room temperature. The remaining half of this dissertation explores BIC lasing cavities and their unique properties.

1.3 Outline of Dissertation

This dissertation work focuses on the two singularities as described above and is organized as follows. Chapter 2 provides an in-depth background for describing open systems with Hamiltonian formalism derived from Coupled Mode Theory (CMT) and non-Hermitian quantum mechanics in the context of exploring hybridized plasmonic resonances of the shift-bar system. Chapter 3 judiciously builds on this and explores EPs and their properties in more complicated plasmonic structures. Chapter 4 is an extensive study on single-mode resonance trapped BIC lasers and their properties with details on experimental characterization and results. Chapter 5 follows up with the fabrication details of these suspended membrane BIC lasers and its challenges. Lastly, in Chapter 6, I discuss future research directions as it pertains to EPs and BICs while summarizing the present work.

References

1. N. Moiseyev, *Non-Hermitian Quantum Mechanics* (Cambridge University Press, United Kingdom 2011).
2. F-M. Dittes, “The decay of quantum systems with a small number of open channels,” *Phys. Rep.* **339**, 215 (2000).
3. T. Kato, *Perturbation Theory of Linear Operators* (Springer, Berlin 1966).
4. W.D. Heiss, “The physics of exceptional points,” *J. Phys. A: Math. Theor.* **45**, 444016 (2012).
5. J. Wiersig, “Enhancing the Sensitivity of Frequency and Energy Splitting Detection by Using Exceptional Points: Application to Microcavity Sensors for Single-Particle Detection,” *Phys. Rev. Lett.* **112**, 203901 (2014).
6. H. Hodaei, A. U. Hassan, S. Wittek, H. Garcia-Garcia, R. El-Ganainy, D. N. Christodoulides, and M. Khajavikhan, “Enhanced sensitivity at higher-order exceptional points,” *Nature* **548**, 192 (2017).
7. W. Chen, S. K. Ozdemir, G. Zhao, J. Wiersig, and L. Yang, “Exceptional points enhance sensing in an optical microcavity,” *Nature* **548**, 187 (2017).
8. B. Kanté, S.N. Burokur, A. Sellier, A. de Lustrac, and J.-M. Lourtioz, “Controlling Plasmon hybridization for negative refraction metamaterials,” *Phys. Rev. B* **79**, 075121 (2009).
9. V. M. Shalaev, W. Cai, U. K. Chettiar, H-K. Yuan, A. K. Sarychev, V. P. Drachev, and A. V. Kildishev, “Negative index of refraction in optical metamaterials,” *Opt. Lett.* **30**, 3356 (2005).
10. J. von Neumann and E. Wigner, “On some peculiar discrete eigenvalues,” *Phys. Z* **30**, 467 (1929).
11. C. W. Hsu, B. Zhen, A. Douglas Stone, J. D. Joannopoulos, and M. Soljacic, “Bound states in the continuum,” *Nat. Rev. Mater.* **1**, 16048 (2016).
12. D. C. Marinica, A. G. Borisov, and S. V. Shabanov, “Bound states in the continuum in photonics,” *Phys. Rev. Lett.* **100**, 183902 (2008).
13. E. N. Bulgakov and A. F. Sadreev, “Bound states in the continuum in photonic waveguides inspired by defects,” *Phys. Rev. B* **78**, 075105 (2008).

14. T. Lepetit, E. Akmansoy, J.-P. Ganne, and J.-M. Lourtioz, “Resonance continuum coupling in high-permittivity dielectric metamaterials,” *Phys. Rev. B* **82**, 195307 (2010).
15. T. Lepetit and B. Kanté, “Controlling multipolar radiation with symmetries for electromagnetic bound states in the continuum,” *Phys. Rev. B* **90**, 241103(R) (2014).
16. C. W. Hsu, B. Zhen, J. Lee, S-L. Chua, S. G. Johnson, J. D. Joannopoulos, and M. Soljacic, “Observation of trapped light within the radiation continuum,” *Nature* **499**, 188-191 (2013).
17. B. Zhen, C. W. Hsu, L. Lu, A. Douglas Stone, and M. Soljacic, “Topological nature of optical bound states in the continuum,” *Phys. Rev. Lett.* **113**, 257401 (2014).

Chapter 2

Resonance Dynamics of Plasmon Hybridized Systems

2.1 Introduction

Over the past decade, there has been considerable interest and progress in the field of plasmonics. Primarily, the focus has been in realizing devices that leverage plasmonics' ability to manipulate light at a sub-wavelength scale. These devices have enabled a wide range of applications spanning plasmon-lasers [1], amplifiers [2], sub-wavelength imaging [3], enhanced photovoltaics [4], and chemical and biological sensing [5]. Resonances are an integral part of said devices and control over them will propel the next wave of plasmonic technology. Usually, the approach to analyzing plasmonic resonances, which is inspired by Lorentzian resonances, is to locate the peaks and troughs of transmission and reflection spectra. However, this approach fails for the general case of non-symmetric or Fano resonances [6], especially if there are overlapping resonances [7]. Naturally, the question arises as to how resonances can be quantitatively observed.

In this chapter, we model resonances in a plasmonic system by using a formalism similar to that of the effective Hamiltonian formalism from non-Hermitian quantum mechanics [8, 9]. In electromagnetism, it has been derived within the framework of Coupled Mode Theory (CMT) [10, 11]. The model system we study has resonances that

arise from strong coupling between closely packed particles and can be understood intuitively as plasmon hybridization [12, 13]. By computing the complex poles of the scattering matrix, we obtain a quantitative estimate of both resonance frequencies and linewidths corresponding to the real and imaginary terms respectively. As such, we are able to track the evolution of these resonances in the complex plane during the hybridization process. We thoroughly investigate a specific system comprising two coupled plasmonic bars and demonstrate that it supports an inverted hybridization scheme. The effective Hamiltonian model is used to identify a negative coupling regime that is at the origin of this hybridization inversion.

2.2 Effective Hamiltonian

We introduce a form of the scattering matrix borrowed from CMT and non-Hermitian quantum mechanics as the basis for analyzing Fano resonances of an optical resonator (see Figure 2.1) [8, 10, 11, 14]. In this formalism, plasmonic resonators are free to interact with their environment *via* radiation and such systems are commonly referred to as being open. Hence, a closed resonator by itself may be viewed as being in constant feedback with its environment. Scattering parameters of the full system can be represented as a superposition between a feedback term which includes the resonances of interest and a background term, \mathbf{C} , as written in Equation (1) and schematically drawn in Figure 2.1b.

$$\mathbf{S} = \mathbf{C} + j\mathbf{V}[\omega\mathbf{I} - \mathbf{H}_{\text{eff}}]^{-1}\mathbf{V}^\dagger \quad (1)$$

Here, \mathbf{C} is a background scattering matrix accounting for resonances away from the frequency range of interest [10, 11, 14, 15]. \mathbf{V} is a complex coupling matrix that captures

the interaction between the environment and the resonator. Lastly, \mathbf{H}_{eff} is an effective Hamiltonian matrix that describes individual resonances that are simultaneously coupled to each other and the environment. This effective Hamiltonian term can be decomposed into two primary components [16], -- one describing the discrete resonator states, \mathbf{H}_0 , -- and another describing the coupling between discrete states and the environment (continuum), $\mathbf{V}\mathbf{V}^\dagger$, as shown in Equation (2).

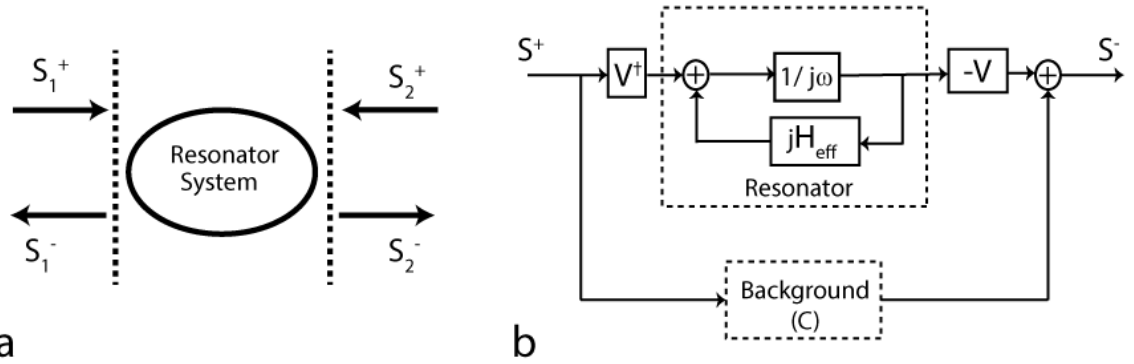


Figure 2.1: (a) Two-port schematic of an optical resonator system with \mathbf{S}^+ (incoming waves) and \mathbf{S}^- (outgoing waves). (b) Block diagram representation of the scattering matrix in terms of the effective Hamiltonian, \mathbf{H}_{eff} , background term, \mathbf{C} , coupling matrix, \mathbf{V} , and its conjugate transpose. The scattering matrix is abstractly represented as a superposition of background term and a resonator system that is in constant feedback with the environment.

$$\mathbf{H}_{\text{eff}} = \mathbf{H}_0 + j \frac{1}{2} \mathbf{V}\mathbf{V}^\dagger + j\Lambda_L \quad (2)$$

The third term, $j\Lambda_L$, in the equation represents extraneous losses. In our case, this term mostly accounts for plasmonic losses. \mathbf{H}_0 is an $n \times n$ Hermitian matrix with ‘ n ’ being the number of resonances. \mathbf{V} is an $n \times m$ coupling matrix with ‘ m ’ representing the number of ports (decay channels) making the second term, $(j/2) \mathbf{V}\mathbf{V}^\dagger$, an $n \times n$ anti-Hermitian matrix. Collectively, this makes the effective Hamiltonian a non-Hermitian matrix with complex eigenvalues signifying the location of resonance frequencies and their respective linewidths (decay rates).

Equation (1) can be appropriately rewritten in rational form where it can be seen at once that the complex poles of the scattering matrix are also the eigenvalues of the effective Hamiltonian, \mathbf{H}_{eff} (see Eq. (3)).

$$S_{nm} = C_{nm} + j \sum_k \frac{\langle \Psi_n | \mathbf{V} | \Psi_k \rangle \langle \tilde{\Psi}_k | \mathbf{V}^\dagger | \Psi_m \rangle}{\omega - \omega_k} \quad (3)$$

Here, ω_k are the eigenvalues of \mathbf{H}_{eff} and Ψ_k , $\tilde{\Psi}_k$ are the eigenvectors of \mathbf{H}_{eff} and its conjugate transpose [9].

2.3 Mode Symmetries of Hybridized Shift-bar System

The plasmonic system based on coupled identical gold bars, depicted in Figure 2.2(a), is considered. The dimensions of a single bar are chosen such that the dipolar resonance resides in the optical domain at a wavelength of 1.55 μm . The reconfigurability and controllability of coupling parameters in such systems have proven advanced opportunity in resonance tuning beyond the capability of isolated antennas [17]. Pairing gold bars in close proximity hybridizes their plasmon modes into modes of opposite symmetries with current oscillating in-phase (symmetric) and out-of-phase (anti-symmetric). The spectral locations of these symmetric and anti-symmetric resonances can be tuned by spatially translating one bar in relation to its counterpart. Such a hybridization scheme has previously been used to demonstrate negative refraction [18, 19], but the quantitative description of resonance dynamics remains unexplored.

We consider the unit cell of an array consisting of paired gold bars separated by a thin silicon dioxide spacer as illustrated in Figure 2.2. An incident plane wave with the electric field parallel to the length of the bars is used to excite the system.

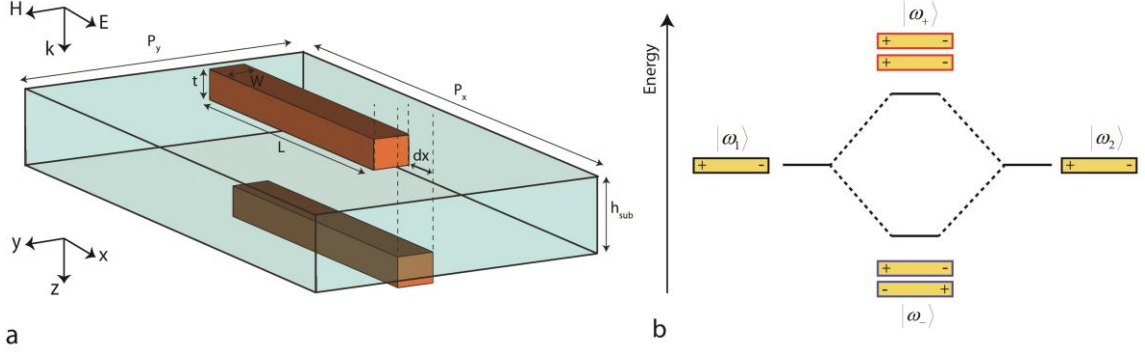


Figure 2.2: (a) Physical setup of paired gold bars separated by a dielectric (SiO_2) spacer with dimensions: $L=450$ nm, $W=50$ nm, $t=40$ nm, $p_y=400$ nm, $\epsilon_{\text{sub}}=2.25$ (permittivity of oxide), and variable parameter: h_{sub} , p_x , dx . The gold bars are described using the Drude model with a plasma frequency ($\omega_p=1.367 \times 10^{16}$ rad/sec) and collision frequency ($\omega_c=6.478 \times 10^{13}$ rad/sec) based on values from Reference 20. (b) Energy-level diagram describing the plasmon hybridization in the shift-bar system with modes: ω_+ (Symmetric) and ω_- (Anti-symmetric). ω_1 and ω_2 are the decoupled resonances of each bar.

2.4 S-Parameters and Rational Fitting

We compute the scattering parameters using full-wave finite-element simulations and observe two resonances. The resonances we observe share an asymmetric line-shape characteristic of Fano resonances [6, 21]. In general, Fano resonances occur as a result of interference between a narrow resonance and a broader continuum. Due to the asymmetric line-shape of a Fano resonance, it is difficult to pinpoint a resonance frequency and its linewidth from transmission and reflection spectra. To clarify this, we provide here the expressions capturing Fano behavior for reflection, $|S_{11}|^2$, and transmission, $|S_{21}|^2$, spectra derived from CMT pertaining to a single resonance and single continuum [11, 15].

$$|S_{11}(\omega)|^2 = |r|^2 \frac{|E \pm 1/q|^2}{E^2 + 1} \quad (4)$$

$$|S_{21}(\omega)|^2 = |t|^2 \frac{|E \mp q|^2}{E^2 + 1} \quad (5)$$

Here, E is the reduced energy ($E = (\omega - \omega_0)/\gamma_0$), q is the asymmetry parameter ($q = r/t$), ω_0 is the resonant frequency, γ_0 is the linewidth, with r and t denoting the complex

background reflection and transmission coefficients respectively. For cases when q is either zero or infinity, the line-shape is symmetric and Lorentzian. When q is between zero and infinity, the line-shape is asymmetric for a single resonance. From the above equations, we see that the transmission tends to zero when $\omega = \omega_0 \pm \gamma_0 q$ and the reflection is zero when $\omega = \omega_0 \mp \gamma_0/q$. As such, it can be clearly seen that the resonance information cannot be inferred from the peaks and troughs of transmission and reflection spectra when the resonance is asymmetric. Besides, this is insufficient for cases with multiple resonances as is the case for our plasmonic system.

In our system, the quantitative values of the two resonance frequencies and their respective linewidths are not immediately apparent. The scattering amplitude matrix provides information on the frequency evolution of transmission and reflection coefficients which are fitted by a rational function of the form given by Eq.(6), based on Eq.(3). The fit yields complex poles corresponding to the symmetric, $\omega_+ + j\gamma_+$, and anti-symmetric, $\omega_- + j\gamma_-$, modes as well as background poles in S_b . The real and imaginary parts of the complex poles indicate the resonant frequencies and linewidths respectively.

$$S_{mn}(\omega) = \frac{c_+}{\omega - (\omega_+ \pm j\gamma_+)} + \frac{c_-}{\omega - (\omega_- \pm j\gamma_-)} + S_b \quad (6)$$

Figure 2.3 and Figure 2.4 show the excellent fit of scattering parameters with rational functions, yielding reliable values for the resonance frequencies and linewidths. Note that the extracted poles affiliated with the resonances are the same for both transmission, $|S_{21}|^2$, and reflection, $|S_{11}|^2$.

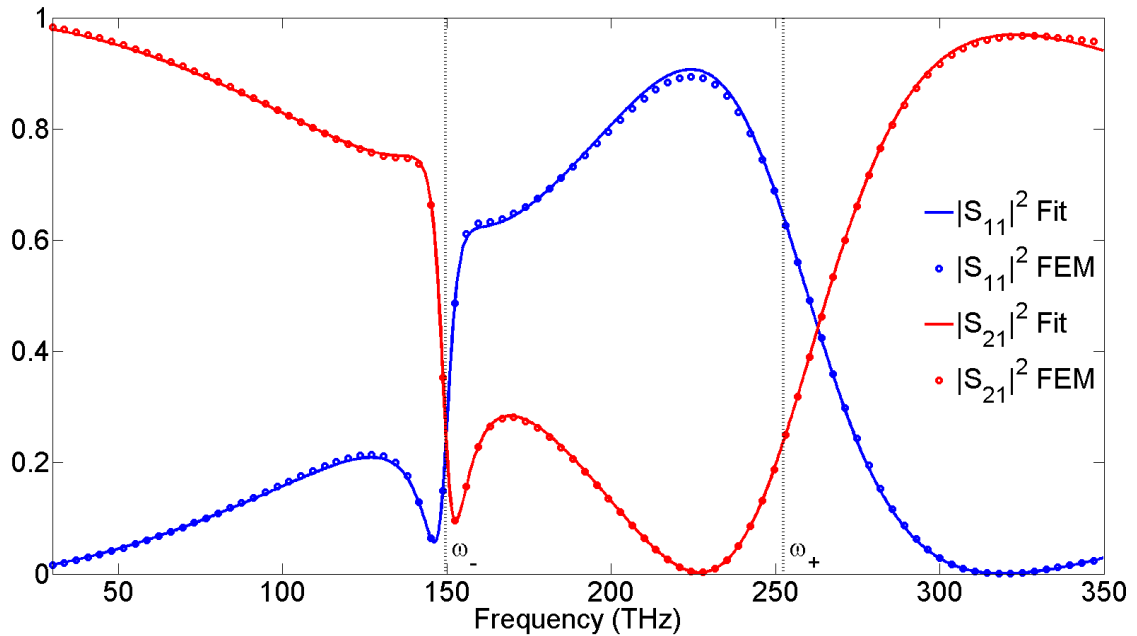


Figure 2.3: Simulated transmission, $|S_{21}|^2$, and reflection, $|S_{11}|^2$, spectra (solid curve) and their rational fits (dots) for $p_x=800$ nm, $h_{\text{sub}}=100$ nm, and $dx=0$. ω_- and ω_+ are the resonant frequencies of the anti-symmetric and symmetric modes in that order indicated here by dashed vertical black lines. γ_- and γ_+ are the corresponding linewidths. The resonance information extracted is as follows: $\omega_-=149.6$ THz, $\gamma_-=9.8$ THz, $\omega_+=252.5$ THz, $\gamma_+=97$ THz.

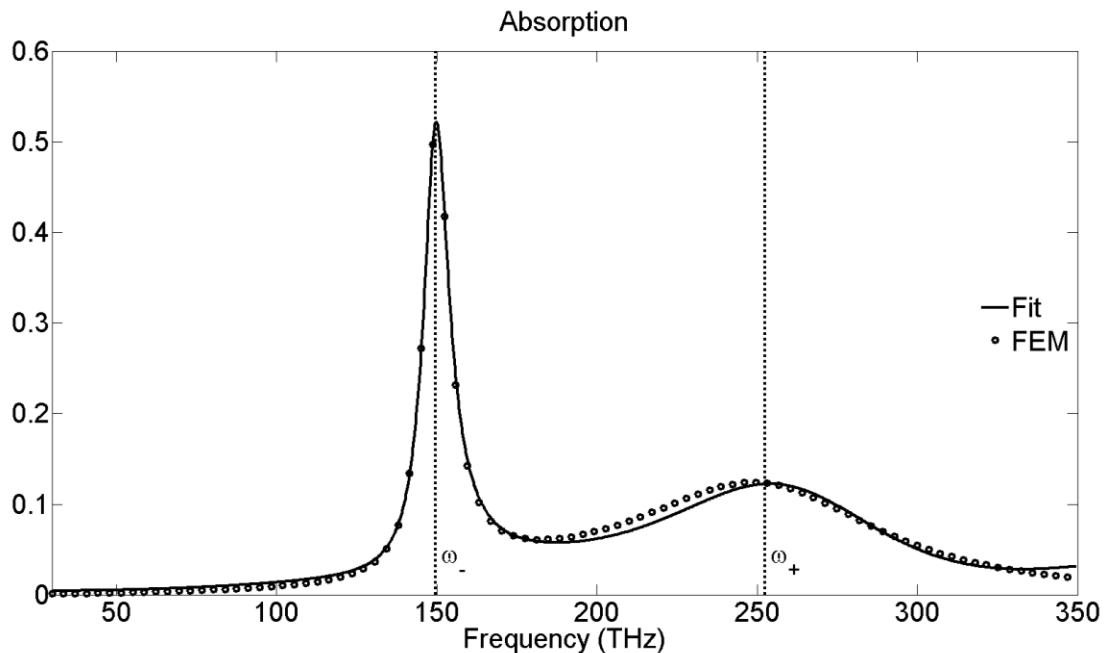


Figure 2.4: Simulated absorption, $1-|S_{11}|^2-|S_{21}|^2$, spectra (solid curve) and its rational fit (dots) for the case above: $p_x=800$ nm, $h_{\text{sub}}=100$ nm, and $dx=0$.

This method of tracking resonance behavior is general and is not limited to the shift-bar system and can be readily applied in situations involving more complex geometries such as dimers, core-shells, and other systems [12, 13, 22]. This method should be used for resonances away from any diffraction thresholds arising from the periodicity. The structures need not be of sub-wavelength dimensions to apply this method, i.e., it is valid in between diffraction thresholds [23]. This convenient technique will be used to study the dynamics of resonances for the shift-bar system as physical parameters such as the x-shift, dx , oxide thickness, h_{sub} , and x-periodicity, p_x , are varied.

2.5 Inversion Point and Degree of Inversion

Using the model previously presented, we examine the effect of shifting a bar in the x-direction on the symmetric and anti-symmetric resonances. We note that such symmetry-breaking has not been quantitatively studied so far. Initially at no-shift, the symmetric mode resides at a higher energy (higher frequency) due to repelling forces and the anti-symmetric mode is at a lower energy (lower frequency) as a result of attractive forces (see Figure 2.2(b)). As the setup is modified by shifting one bar, the initial symmetry, along the plane bisecting the thickness of the substrate, is broken [18, 24, 25]. The degree to which this symmetry is broken between the bars determines the strength of the Coulomb forces pertaining to the two plasmon modes. As one of the bars is progressively displaced, the repelling forces associated with the symmetric mode weaken and at some point become attractive. Similarly, the attractive forces relating to the anti-symmetric mode weaken to become repulsive. This is clearly observed in Figure 2.5(b) where the frequency of the high frequency resonance, ω_+ , decreases with increasing shift,

dx , and the frequency of the low frequency resonance, ω_- , increases with shift. In the following, the point at which the two resonances cross will be termed the ‘inversion point’ and the difference between the resonant frequencies ($\Delta\omega=\omega_+-\omega_-$) referred to as the ‘degree of inversion’.

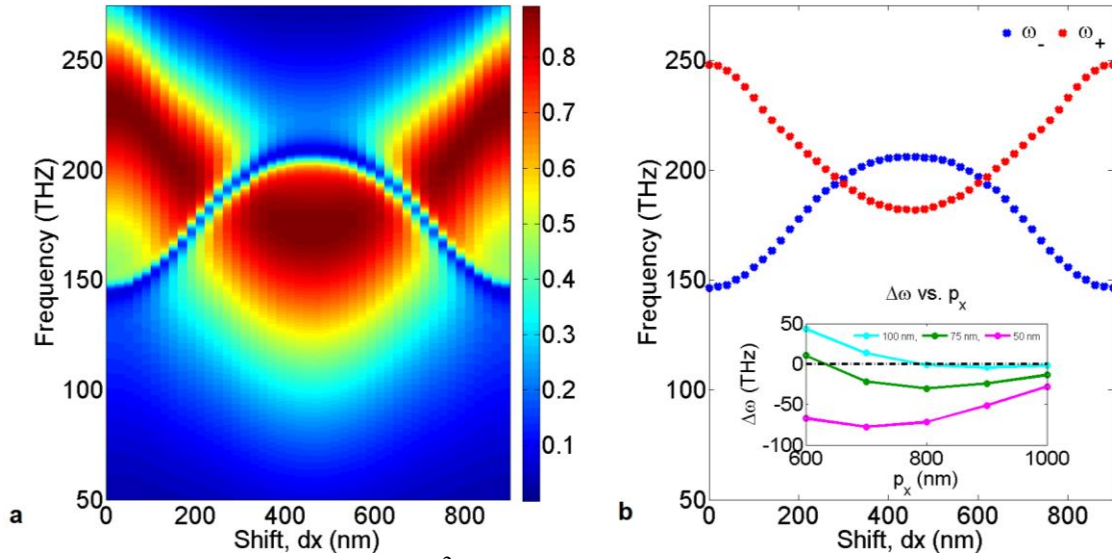


Figure 2.5: Reflection spectra, $|S_{11}|^2$, as a function of shift ‘ dx ’ for $p_x=900$ nm and $h_{\text{sub}}=75$ nm (a) and corresponding resonant frequencies acquired via rational fitting (b). The inset plot indicates the degree of inversion, $\Delta\omega$, at $dx=p_x/2$ as a function of periodicity and oxide thickness, $h_{\text{sub}}=100$ nm (cyan), 75 nm (green), 50 nm (magenta). Positive $\Delta\omega$ indicates the resonances have not crossed and negative means they have crossed to reach inversion. The inset shows that inversion is not always achieved. See Appendix A for full scattering parameters and inversion computation.

Figure 2.5(a) is a color plot of the reflection spectra, $|S_{11}|^2$, as a function of the shift, dx . The locations of the resonance frequencies, corresponding to either the symmetric or anti-symmetric modes, are not easily discernible. Discerning the resonance frequency for the symmetric mode is particularly difficult due to its broader nature. Therefore, by employing the previously outlined rational fitting scheme, we can quantitatively track the resonances. The results are presented in Figure 2.5(b). It is worth noting here that the resonances exhibit periodic behavior with dx due to the periodicity, p_x , of structure under

consideration. The plot in Figure 2.5(b) is symmetric along the point $dx=p_x/2$ just as the physical geometry is symmetric with respect to a shift of $p_x/2$. Hence, the periodicity in the x -direction has an influence on the maximum degree of inversion as does the substrate thickness, h_{sub} . Reducing the substrate thickness increases the near-field coupling between the bars thereby increasing the likelihood of achieving inversion as shown in the inset of Figure 2.5(b). For a substrate thickness of 100 nm, the inversion is either inconspicuous or nonexistent as a consequence of a weaker near-field coupling compared to thicknesses of 75 and 50 nm. The inversion is thus a consequence of near-field coupling and also depends on the x -periodicity of the unit cell. Once the resonance frequencies are extracted for a certain parameter space as seen in Figure 2.5(b), we are able to choose a distinct dx parameter value in order to tailor the resonance frequency of the shift-bar system.

2.6 Static Dipole Approximation

Thus far, we have analyzed the resonant behavior of the shift-bar system in the context of scattering parameters. We may also view these bars as interacting static dipoles with finite dipole moments. This approximation can be made due to the particles' sub-wavelength dimensions. The length of a bar is a third of the free-space wavelength, i.e. $L \sim \lambda_0/3$. We now consider a pair of static and point-like dipoles as a substitute for gold bars. The interaction energy between them can be written as

$$W_{12} = \frac{\mathbf{p}_1 \cdot \mathbf{p}_2 - 3(\mathbf{n} \cdot \mathbf{p}_1)(\mathbf{n} \cdot \mathbf{p}_2)}{4\pi\epsilon_0|\mathbf{x}_1 - \mathbf{x}_2|^3} \quad (7)$$

where $\mathbf{p}_1, \mathbf{p}_2$ are the individual dipole moments and $\mathbf{x}_1, \mathbf{x}_2$ are the position vectors from the origin, and \mathbf{n} is the unit normal vector pointing in the direction of $\mathbf{x}_1 - \mathbf{x}_2$ [26, 27]. The

interaction energies for the symmetric and anti-symmetric cases are plotted in Figure 2.6(a) as a function of shift, dx . The symmetric case describes like dipoles pointing in the same direction and the anti-symmetric case describes like dipoles pointing in opposite directions with dipoles separated by distance, d , in both cases. The energies are greatest when both dipoles are aligned, and they approach each other eventually crossing before reaching a maxima. After the maxima, they slowly asymptote to zero as the two dipoles grow farther apart. A similar situation arises when we consider a finite array (N-by-N) of dipoles arranged into two sheets also separated by distance, d , as seen in Figure 2.6(b). Here, the interaction energy is calculated in the perspective of the center dipole of a single sheet as described by Equation (8).

$$W_{1_total} = \sum_{n=2}^{N^2} W_{1n} + \sum_{k=1}^{K^2} W_{1k} \quad (8)$$

The first term is the sum of all in-plane dipole interactions and the second term captures the out-of-plane interactions. The energies plotted in Figure 2.6(b) for an array size of 9x9 as a function of shift, dx , clearly show the periodic nature of the system. The tail asymptote here occurs as a consequence of a shift larger than half the sheet length when the center dipole is no longer in close proximity with a dipole in the adjacent plane. Note that this asymptotic tail is not observed for an infinite array when N approaches infinity.

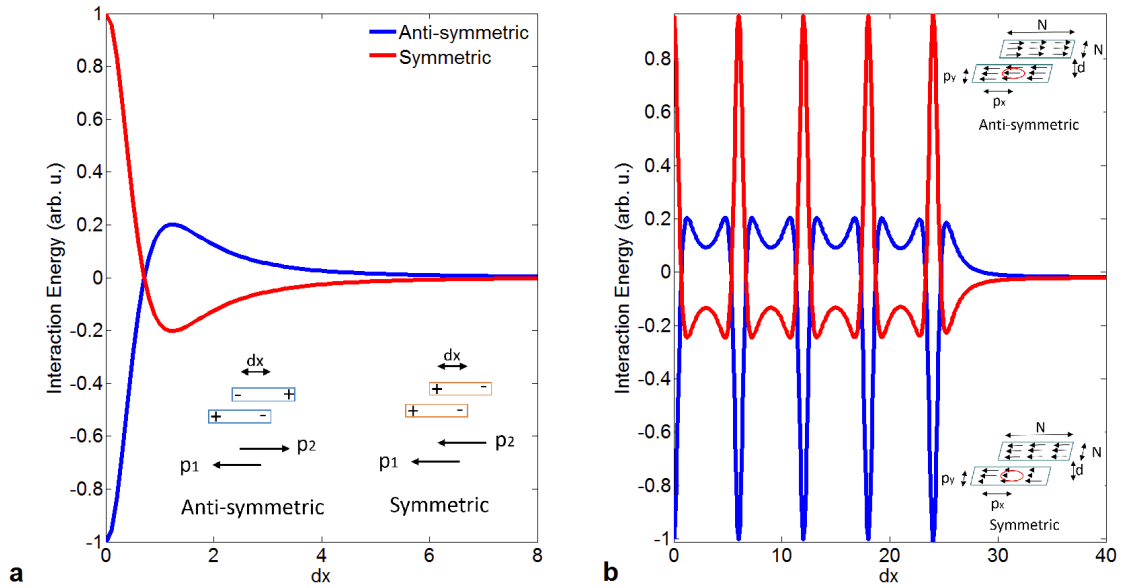


Figure 2.6: (a) Interaction energy between two dipoles in the symmetric and anti-symmetric configuration. (b) Interaction energy for symmetric and anti-symmetric case seen by center dipole embedded in the first sheet of $N \times N$ array of dipoles with $N=9$, $p_x=6$, $p_y=12$, $d=1$, and dipole moments of unit magnitude. The insets portray a schematic view of different dipole configurations.

The behavior of the interaction energies in the inversion region is also of interest. For an array, the interaction energies reach their respective maxima before declining similar to the two-dipole scenario. The energies start approaching a local asymptote within the inversion region if the x -periodicity is large. The asymptotic behavior within the inversion region in an ensemble of interacting static dipoles is reminiscent of our original shift-bar system with a large x -periodicity, p_x . However, if the periodicity is small, the energies do not reach their absolute maxima and in extreme cases inversion is not achieved.

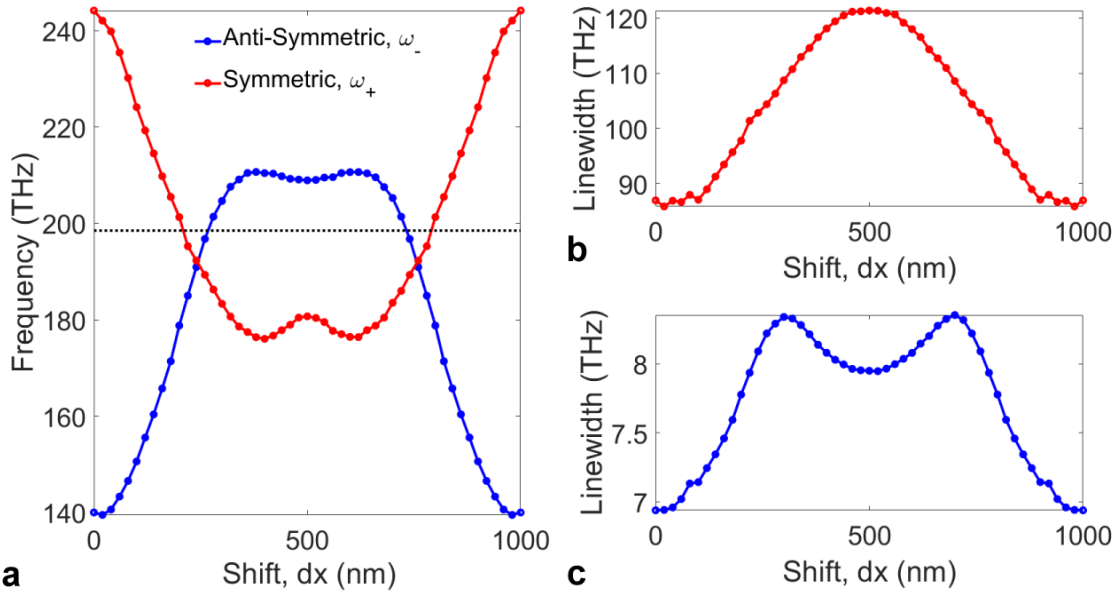


Figure 2.7: (a) Evolution of resonant frequencies as a function of shift, dx , with linewidths pertaining to (b) symmetric and (c) anti-symmetric modes for shift-bar system with dimensions $p_x=1000$ nm and $h_{\text{sub}}=50$ nm. The dotted line indicates the uncoupled resonance frequency at 198.5 THz. See Appendix A for full set of complex eigenvalues.

We show in Figure 2.7 the resonant frequencies and linewidths for the shift-bar system with a large x -periodicity of 1000 nm. In the inversion region, we noticeably observe that the resonance frequencies approach a local asymptote after reaching their maxima in a manner similar to the static dipole model. The linewidth of the symmetric mode is an order of magnitude greater than that of the anti-symmetric mode. We note that a pair of anti-symmetric dipoles has a combined dipole moment that is zero whereas the symmetric pair has a combined moment that is additive and non-zero. Therefore, considering dynamic effects, the symmetric mode corresponding to the symmetric dipole pair will strongly radiate into the continuum thus exhibiting a broad Fano resonance. Conversely, the anti-symmetric mode will be sub-radiant and will have a much narrower Fano resonance. A more rigorous dynamic model, considering retardation effects, of the shift-bar system would be needed to capture some of the asymmetries that the static dipole

model does not explain. At optical frequencies, retardation effects play an important role in determining resonances due to the large size of structures [28].

2.7 Negative Coupling Regime

The shift-bar systems can also be described by expanding the effective Hamiltonian, \mathbf{H}_{eff} , in Equation (2) to a 2x2 matrix given by Equation (9). Here, ω_1 is the resonant frequency of a single gold bar, κ is the complex coupling constant between the two bars, γ_1 and γ_2 are the diagonal terms of $\mathbf{V}\mathbf{V}^+$ matrix, γ_0 and its conjugate are the cross terms. Lastly, γ_{1L} and γ_{2L} are the extraneous material losses.

$$\mathbf{H}_{eff} = \begin{bmatrix} \omega_1 & \kappa \\ \kappa^* & \omega_1 \end{bmatrix} + \frac{j}{2} \begin{bmatrix} \gamma_1 & \gamma_0 \\ \gamma_0^* & \gamma_2 \end{bmatrix} + j \begin{bmatrix} \gamma_{1L} & 0 \\ 0 & \gamma_{2L} \end{bmatrix} \quad (9)$$

Starting with a simple but periodic form for the coupling constant, κ , described in Equation (10), we compute the eigenvalues of the effective Hamiltonian. The coupling constant is taken to be periodic as we expect resonances to be periodic with shift, dx . We assume the following modulation for κ :

$$\kappa = \kappa_0 + \beta \cos\left(\frac{2\pi}{p_x} dx\right) \quad (10)$$

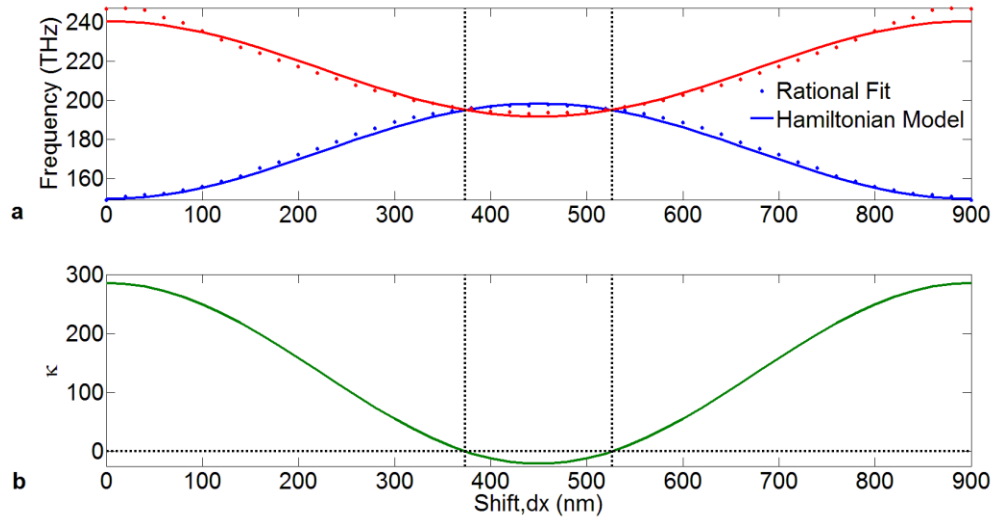


Figure 2.8: (a) Resonant frequencies of shift-bar system acquired via rational fitting (dots) and resonant frequencies from Hamiltonian Model (solid) for the symmetric (red) and anti-symmetric (blue) modes. (b) Coupling constant, κ , in green used to compute the resonant frequencies with parameters: $p_x=900$ nm, $h_{\text{sub}}=100$ nm, $\kappa_0=132$, $\beta=153$, and $\omega_1=195$ THz. The vertical dotted lines denote the zero-crossing points for κ .

The resonant frequencies extracted by rational fitting to the scattering parameters are superimposed with resonant frequencies computed using the Hamiltonian model as seen in Figure 2.8(a). There is good agreement between the two. Results in the figure show that the coupling constant is negative within the inversion region which is indicative of an inverted plasmon hybridization [24]. This behavior is typical of coupled electric dipoles and can thus be expected to hold for many different plasmonic resonators around their electric dipole resonance. The shift-bar system described above was experimentally realized on a glass substrate and is in agreement with the predictions (see Reference 29).

2.8 Concluding Remarks

In this chapter, we have demonstrated that the effective Hamiltonian formalism can be used to explain the negative coupling behavior within the inversion region for our

plasmonic shift-bar system. Due to a strong dependence on near field interactions, the inversion is contingent on the periodicity and substrate thickness. To this end, we employed a static dipole approximation to provide an intuitive description of the effects of periodicity on interaction energies. For large periodicities, we find the energies approach a local asymptote within the inversion region and small periodicities may not achieve inversion. The degree of inversion and the location of the inversion point are easily and widely tuned by varying the periodicity, substrate thickness, and shift. Hence, resonances in the shift-bar system are highly tunable. Additionally, we experimentally and quantitatively show the inversion of the two fundamental resonances. Moreover, we accurately extracted resonance information, both resonant frequencies and linewidths, solely from experimental and numerical scattering parameters. The quantitative approach to extracting complex poles presented here can be generalized to any system exhibiting asymmetric Fano resonances. This powerful approach is still valid for cases with multiple overlapping resonances. Therefore, this work will greatly enhance the ability to engineer resonances of future plasmonic devices. Lastly, the work presented in this chapter serves as the groundwork for a more complex plasmonic system studied in Chapter 3 that has great potential for sensing applications.

Chapter 2, in part, is a reprint of the material as it appears in A. Kodigala, T. Lepetit, and B. Kanté, "Engineering resonance dynamics of plasmon hybridized systems," *Journal of applied physics* **117**, 023110 (2015). The dissertation author was the primary researcher and author of this paper.

References

1. R-M. Ma, R. F. Oulton, V. J. Sorger, G. Bartal, and X. Zhang, "Room-temperature sub diffraction-limited plasmon laser by total internal reflection," *Nature Mater.* **10**, 110 (2011).
2. P. Berini, and I. De Leon, "Surface plasmon-polariton amplifiers and lasers," *Nature Phot.* **6**, 16 (2012).
3. J. A. Schuller, E. S. Barnard, W. Cai, Y. C. Jun, J. S. White, and M. L. Brongersma, "Plasmonics for extreme light concentration and manipulation," *Nature Mater.* **9**, 193 (2010).
4. H. A. Atwater and A. Polman, "Plasmonics for improved photovoltaic devices," *Nature Mater.* **9**, 205 (2010).
5. N. Liu, M. Hentschel, T. Weiss, A. P. Alivisatos, and Harald Giessen, "Three-Dimensional Plasmon Rulers," *Science* **332**, 1407 (2011).
6. U. Fano, "Effects of Configuration Interaction on Intensities and Phase Shifts," *Phys. Rev.* **124**, 1866 (1961).
7. S. Klaiman, and N. Moiseyev, "The absolute position of a resonance peak," *J. Phys. B: At. Mol. Opt. Phys.* **43**, 185205 (2010).
8. N. Moiseyev, *Non-Hermitian Quantum Mechanics* (Cambridge University Press, United Kingdom 2011).
9. F-M. Dittes, "The decay of quantum systems with a small number of open channels," *Phys. Rep.* **339**, 215 (2000).
10. W. Suh, Z. Wang, and S. Fan, "Temporal Coupled-Mode Theory and the Presence of Non-Orthogonal Modes in Lossless Multimode Cavities," *IEEE J. Quant. Electron.* **40**, 1511 (2004).
11. S. Fan, W. Suh, and J.D. Joannopoulos, "Temporal coupled-mode theory for the Fano resonance in optical resonators," *J. Opt. Soc. Am. A* **20**, 569 (2003).
12. P. Nordlander, C. Oubre, E. Prodan, K. Li, and M.I. Stockman, "Plasmon Hybridization in Nanoparticle Dimers," *Nano Lett.* **4**, 899 (2004).
13. E. Prodan, C. Radloff, N. J. Halas, P. Nordlander, "A Hybridization Model for the Plasmon Response of Complex Nanostructures," *Science* **302**, 419 (2003).
14. J. P. Hespanha, *Linear Systems Theory* (Princeton University Press, New Jersey 2009).

15. T. Lepetit, E. Akmansoy, J.-P. Ganne, and J.-M. Lourtioz, "Resonance continuum coupling in high-permittivity dielectric metamaterials," *Phys. Rev. B* **82**, 195307 (2010).
16. H. Feshbach, "Unified theory of nuclear reactions," *Ann. Phys.* **19**, 287 (1962).
17. L. Novotny and N. Van Hulst, "Antennas for light", *Nature Photon.* **5**, 83 (2011).
18. B. Kanté, S.N. Burokur, A. Sellier, A. de Lustrac, and J.-M. Lourtioz, "Controlling Plasmon hybridization for negative refraction metamaterials," *Phys. Rev. B* **79**, 075121 (2009).
19. V. M. Shalaev, W. Cai, U. K. Chettiar, H-K. Yuan, A. K. Sarychev, V. P. Drachev, and A. V. Kildishev, "Negative index of refraction in optical metamaterials," *Opt. Lett.* **30**, 3356 (2005).
20. P. B. Johnson and R. W. Christy, "Optical Constant of the Noble Metals," *Phys. Rev. B* **6**, 4370 (1972).
21. B. Luk'yanchuk, N. I. Zheludev, S. A. Maier, N. J. Halas, P. Nordlander, H. Giessen, and C. T. Chong, "The Fano resonance in plasmonic nanostructures and metamaterials," *Nature Mater.* **9**, 707 (2010).
22. J.A. Fan, C. Wu, K. Bao, J. Bao, R. Bardhan, N. J. Halas, V. N. Manoharan, P. Nordlander, G. Shvets, F. Capasso, "Self-Assembled Plasmonic Nanoparticle Clusters," *Science* **328**, 1135 (2010).
23. N. A. Gippius, T. Weiss, S. G. Tikhodeev, and H. Giessen, "Resonant mode coupling of optical resonances in stacked nanostructures," *Opt. Exp.* **18**, 7569 (2010).
24. B. Kanté, Y.-S. Park, K. O'Brien, D. Shuldman, N. D. Lanzillotti-Kimura, Z. J. Wong, X. Yin, and X. Zhang, "Symmetry breaking and optical negative index of closed nanorings," *Nat. Commun.* **3**, 1180 (2012).
25. A. Christ, Y. Ekinici, H. H. Solak, N. A Gippius, S. G. Tikhodeev, and O. J. F. Martin, "Controlling the Fano interference in a plasmonic lattice," *Phys. Rev. B* **76**, 201405(R) (2007).
26. J. D. Jackson, *Classical Electrodynamics*, Chapter 4 (3rd ed.) (John Wiley & Sons, Inc., New York 1998).
27. S. A. Maier, *Plasmonics: Fundamentals and Applications*, Chapter 5 (Springer Science, New York 2007).
28. F. Tam, A. L. Chen, J. Kundu, H. Wang, and N. J. Halas, "Mesoscopic nanoshells: Geometry-dependent plasmon resonances beyond the quasistatic limit," *J. Chem. Phys.* **127**, 204703 (2007).

29. J. Park, A. Kodigala, A. Ndao, and B. Kanté, “Hybridized metamaterial platform for nano-scale sensing,” *Opt. Exp.* **25**, 15590 (2017).

Chapter 3

Exceptional Points (EPs) in Three-Dimensional Plasmonic Nanostructures

3.1 Introduction

In this section of the chapter, we expand on the discussion of open systems started in Chapter 1 in the context of EPs. As stated previously, most physical systems are open in nature, *i.e.* energy flows in and out and is exchanged with the environment as radiation and absorption which is in contrast with closed systems where energy stays put and is conserved. Closed systems benefit from the well-established theory for conservative systems, *i.e.* Hermitian systems. A remarkable difference is that in Hermitian systems, eigenmodes do not decay and their corresponding eigenvalues are real whereas in non-Hermitian systems eigenmodes do decay and consequently their corresponding eigenvalues are complex [1]. Over the last decade many have sought to bridge the gap between physics of open and closed systems. This renewed attention has underlined one of the fundamental differences between Hermitian and non-Hermitian systems: their singularities. In Hermitian systems, modes couple to induce singularities called diabolical points (DPs), where only the respective eigenvalues are equal whereas for non-Hermitian

systems modes couple to induce singularities called exceptional points (EPs), where both eigenvalues and eigenvectors coalesce [2-3].

In conjunction with theoretical inquiries, recent experimental work has given a glimpse of the many promises that an increased understanding of open systems holds. For instance, there has been ample effort in realizing novel photonic devices in the realm of lasers such as: PT-symmetric lasers [4-5], lasers operating near EPs [6], Bound State in Continuum lasers [7-9]. Concurrently, there has also been theoretical progress with strictly passive devices exploiting EPs for a superior sensing scheme that offers enhanced sensitivity [10-11]. Recently, however, there is experimental realization of EPs demonstrating enhanced sensitivity in a whispering gallery resonator system and a micro-ring resonator system [12-13]. Thus far, EPs have been experimentally studied in a variety of physical systems including 2D microwave cavities [14], electronic circuits [15], 2D chaotic optical microcavities [16], and coupled atom-cavity systems [17]. However, to date, exceptional points have not been realized in a fully three-dimensional plasmonic system. This is of importance because it is highly desirable to have a sensitive sub-wavelength sensing system compatible with biologically relevant substances. Plasmons resulting from the interaction between photons and free electrons are ideally suited for biological sensing given the field enhancement and resonance sensitivity to environment.

3.2 Mode Symmetries of Hybridized Three-bar System

Here, we report the first evidence of the existence of EPs in an open plasmonic system made of coupled plasmonic nanoresonators. We show that the control of the near-field and far-field interactions lead to a systematic construction of EPs. We subsequently

propose a general class of plasmonic architecture exhibiting designer exceptional points. We consider the plasmonic system based on three coupled nanobars, depicted in Figure 3.1a. The dimensions of an individual gold nanobar are chosen such that the fundamental resonance falls in the optical domain at a frequency of 193.5 THz (1.55 μm). Placing these gold nanobars in close proximity couples their individual plasmon modes into hybrid modes as shown in Figure 3.1b [18]. Here, the instantaneous charge profiles of the first three modes are depicted. Intrinsicly, the system has reflection symmetry with respect to the xy -plane that bisects the central nanobar and its modes are thus either even or odd. In our case, modes A and C have an even symmetry whereas Mode B has an odd symmetry. Mode A, with eigenfrequency ω_A , has charges in all the bars oscillating in-phase and mode C, with eigenfrequency ω_C , has charges in all bars oscillating out-of-phase. Mode B, ω_B , has no charges in the central bar as seen in Figure 3.1b. Therefore, mode A resides at a higher energy (higher frequency) due to all repelling Coulomb interactions and mode C resides at a lower energy (lower frequency) as a result of attractive Coulomb interactions. Lastly, mode B resides between mode A and mode C on the energy scale.

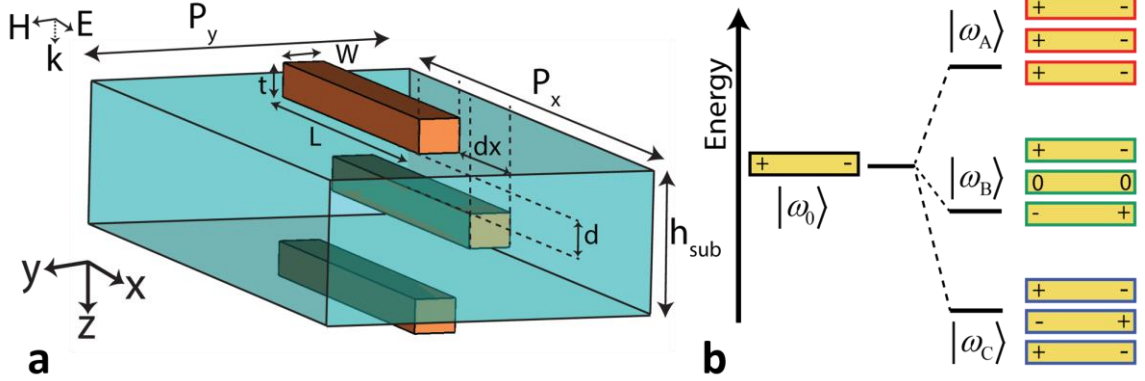


Figure 3.1: (a) Physical setup of a unit cell with three paired gold bars, with the middle one separated by a variable distance (dx , dy , dz) with respect to the other two. The dimensions of each nanobar are given by L (450 nm), W (50 nm), and t (40 nm). The periodicity in x and y -directions are given by P_x (800 nm) and P_y (400 nm). The dielectric (SiO₂) spacer is shown in blue. The gold bars are described using a Drude model with a plasma frequency ($\omega_p=1.367 \times 10^{16}$ rad/sec) and collision frequency ($\omega_c=6.478 \times 10^{13}$ rad/sec) [19]. (b) Energy-level diagram describing the plasmon hybridization in the gold-bar system with three modes: ω_A , ω_B , ω_C where $\omega_A > \omega_B > \omega_C$ for $dx=0$. ω_0 corresponds to the resonance of an individual bar. See Appendix B for further description of modes and their symmetries.

The formation of an EP can be understood as a specific case of mode coupling and can thus be described by Coupled-Mode-Theory (CMT) as previously stated in Chapter 2. In this framework, mode coupling is described by a non-Hermitian effective Hamiltonian matrix [20, 21].

$$\mathbf{H}_{\text{eff}} = \mathbf{H}_0 + j\mathbf{\Lambda}_L + j\frac{1}{2}\mathbf{V}\mathbf{V}^\dagger \quad (11)$$

Where \mathbf{H}_0 is a Hermitian Hamiltonian matrix that describes the system without coupling (closed system). The second term, $j\mathbf{\Lambda}_L$, in the equation represents extraneous losses. In our case, this term accounts for plasmonic losses. The third term, $\mathbf{V}\mathbf{V}^\dagger$, describes the coupling with the environment. Hence \mathbf{H}_{eff} describes the full system (open system). Here, the eigenmodes of the system are represented by the complex eigenvalues and eigenvectors of the effective Hamiltonian. Experimentally, however, these eigenvalues are not directly

available. Nevertheless, we can measure the scattering spectra and extract eigenvalues as they directly correspond to the complex poles of the scattering spectra [22, 23].

An EP is a singularity of the effective Hamiltonian, which arises due to its non-Hermitian nature, at which two modes coalesce [2]. To achieve an EP, both the real and imaginary parts of the eigenvalues (resonance frequency and linewidth) need to coincide simultaneously. For an EP of order 2, such coalescence is dependent on at least two physical parameters [3]. A method is thus needed to select among the geometrical parameters of the system (dx, dy, dz).

For the three-nanobar setup portrayed in Figure 3.1, a closed system Hamiltonian can be used for an intuitive understanding of the mode behavior as described below.

$$\mathbf{H}_0 = \begin{pmatrix} \omega_0 & \kappa_n & \kappa_{n2} \\ \kappa_n & \omega_0 & \kappa_n \\ \kappa_{n2} & \kappa_n & \omega_0 \end{pmatrix} \quad (12)$$

Here, ω_0 is the uncoupled resonance of an individual nanobar. κ_n and κ_{n2} are the nearest and next-to-nearest neighbor coupling constants acting between two individual nanobars. We note that this matrix is bisymmetric and hence has eigenvectors that are either symmetric (even) or skew-symmetric (odd) [24]. For a 3x3 \mathbf{H}_0 , there are always two even (modes A and C) and one odd (mode B) eigenvectors. For the initial three-nanobar setup ($dx=0, dy=0, dz=0$), κ_n is much larger than κ_{n2} and the Hamiltonian is almost tridiagonal. This is not favorable for coalescence as even and odd modes are then interlaced. Hence, we need to reduce κ_n with respect to κ_{n2} to move away from a diagonally dominant Hamiltonian (1st constraint). Besides, since even and odd modes do not couple, we are only interested in the coalescence of the two even modes. Therefore, we seek a parameter that does not introduce coupling between even and odd modes, *i.e.* does not break the system's

mirror symmetry (2nd constraint). Both constraints can be met by shifting the middle bar along the x-direction [23, 25].

Since plasmonic losses in these identical nanobars are represented by a scalar matrix, the losses only contribute an overall complex shift. Moreover, the coupling to the environment adds to the imaginary part of the eigenvalues.

$$\lambda_i = \omega_i + j\gamma_L^i - j \frac{1}{2} \frac{\mathbf{x}_L^i \mathbf{V} \mathbf{V}^\dagger \mathbf{x}_R^i}{\mathbf{x}_L^i (\mathbf{H}_0 + j\Lambda_L) \mathbf{x}_R^i} \quad i \in \llbracket a, b, c \rrbracket \quad (13)$$

Here, \mathbf{x}_L and \mathbf{x}_R are the left and right eigenvectors respectively. For a sufficient shift, dx and dz , mode A and mode C become degenerate (complex eigenvalue).

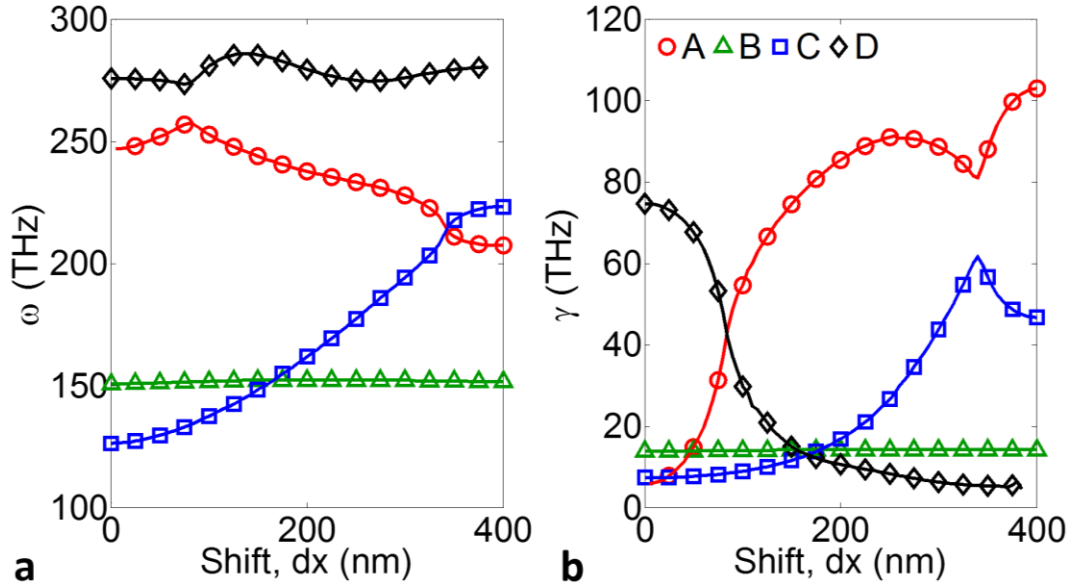


Figure 3.2: Resonance information in the form of complex poles extracted from scattering parameters and plotted as a function of shift ‘ dx ’ (middle-bar) for $P_x=800$ nm and $dz=60$ nm. (a) Resonance frequency of modes A (\circ), B (\triangle), C (\square) and higher order mode D (\diamond) with varying ‘ dx ’ and their corresponding (b) linewidths. There is observable coupling between neighboring modes that share a symmetry, i.e. mode A with C at $dx=350$ nm and mode A with D at $dx=80$ nm. Mode B is unperturbed by both the shift and neighboring modes due to its symmetry. Coupling of modes A and C is of interest for this parameter set as the resonance frequency cross with ‘ dx ’ and linewidths experience an avoided resonance crossing. See Appendix B1 for full scattering parameters for three-bar system.

We now numerically examine the effect of shifting the middle bar in the x-direction on all three modes of the coupled plasmonic system (see Figure 3.2). As the middle bar is progressively displaced, the repelling forces associated with mode A weaken to become attractive. Similarly, the attractive forces of mode C weaken to become repulsive. Lastly, the Coulomb forces associated with mode B remain constant with shift of the central bar as there is no field present in this bar. This behavior is noticeable in the resonances of this system as seen in Figure 3.2a. Mode A moves to lower frequencies with shift and mode C moves to higher frequencies with shift whereas mode B remains unperturbed. Due to the presence of a higher-order resonance (mode D), also with an even symmetry, mode A does not monotonously decrease with shift. For values of 'dx' below 80 nm, mode A increases in frequency with shift due to coupling to mode D. As evident from the coupling between even modes A and D around $dx=100$ nm and between modes A and C at $dx=340$ nm, neighboring resonances of shared symmetry couple to each other. Having an odd symmetry, mode B never couples to any of the even modes. The coupling between modes is further evident in their linewidth behavior as seen in Figure 3.2b. As modes A and D are avoided in frequency at $dx=80$ nm, their respective linewidths cross. Similarly, modes A and C cross in frequency at $dx=340$ nm and their linewidths exhibit an avoided resonance crossing. In terms of the near-field coupling terms, at no shift, *i.e.* $dx=0$, κ_n is the dominant coupling term. With an increase in dx , κ_n weakens with respect to κ_{n2} . It is precisely this interplay that forces the eigenvalues associated with modes A and C to converge towards one another, which is mandatory for engineering an EP. Note that the present system is not exactly at an EP.

3.3 Exceptional Point in Three-bar System

In the close vicinity of an order-2 EP, the effective Hamiltonian of this system can be written in its reduced form as a 2x2 matrix considering only the two concerned even modes [2].

$$\mathbf{H}_{eff} = \begin{bmatrix} \omega_A & 0 \\ 0 & \omega_C \end{bmatrix} + j \begin{bmatrix} \gamma_A & \sqrt{\gamma_A \gamma_C} \\ \sqrt{\gamma_A \gamma_C} & \gamma_C \end{bmatrix} \quad (14)$$

As stated earlier, realization of an EP via two modes requires at least two physical parameters. The two parameters used for the above system to reach an EP are a shift, dx , in the central bar and the inter-spacing between nanobars, dz , in the z -direction where both parameters influence κ_n and κ_{n2} . By performing detailed full-wave finite element simulations, we present here a numerical proof of an EP in our nanobars system (see Figure 3.3). An EP occurs at a frequency of ~ 212 THz for a 345 nm lateral shift of the middle bar and an inter-particle spacing close to 61 nm. For $dz=61$ nm, the two resonance frequencies (ω_A, ω_C) cross each other with increasing shift, dx , and the linewidths (γ_A, γ_C) avoid each other as seen in Figure 3.3a. Conversely, for $dz=61.5$ nm, the linewidths cross and frequencies are avoided as seen in Figure 3.3b. For a value between 61 and 61.5 nm, there is a definite occurrence of an EP singularity where both resonance frequencies and linewidths coalesce.

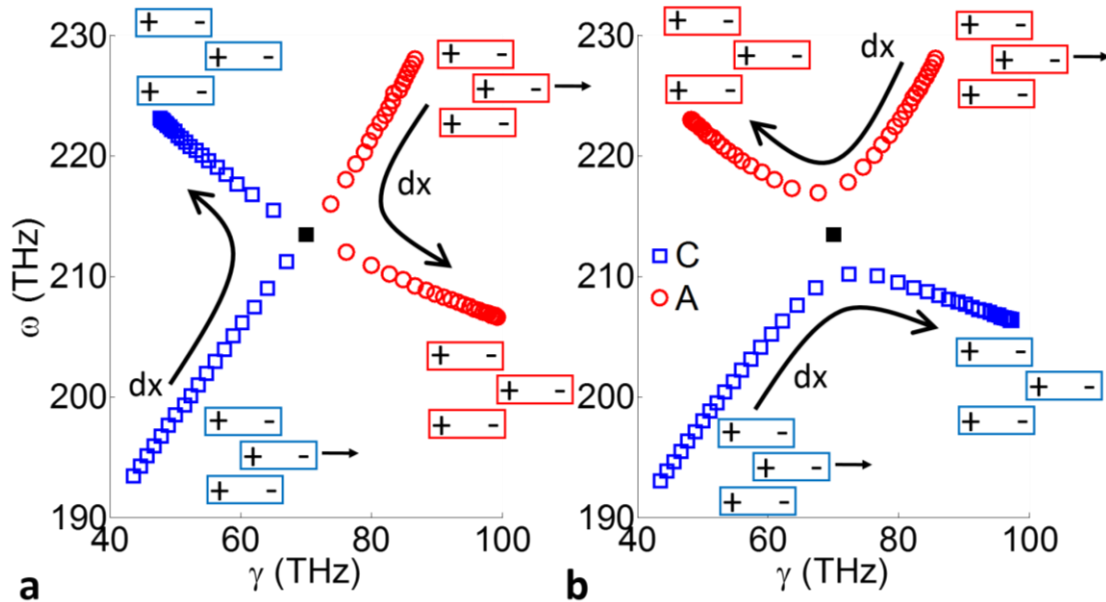


Figure 3.3: Resonances approaching an exceptional point (black ■) plotted in the complex plane ($\gamma+j\omega$) for modes A (○) and C (□) as a function of ‘dx’ (300 to 400 nm) for two different values of inter-bar spacing, $d_z=61$ and 61.5 nm (increasing ‘dx’ indicated by arrows). (a) For $d_z=61$ nm, the resonance frequencies of modes A and C cross as the center bar is shifted (dx) but the linewidths are avoided whereas (b) for $d_z=61.5$ nm, the linewidths cross and the resonance frequencies are avoided. An EP singularity occurs at a value of ‘dz’ between 61 and 61.5 nm for a dx of ~ 345 nm where both resonance frequencies and linewidths coalesce.

3.4 Residue Divergence at EP

Another indication of an occurrence of an EP lies with the complex residues of the corresponding complex poles associated with the resonances [26, 27]. In the case of the three-nanobar system, both the real and imaginary components of the residues diverge as one approaches the EP (see Figure 3.4a-b). As the EP is approached from the left, or increasing dx, the real parts diverge and similarly the imaginary parts diverge as the EP is approached from the right. However, the sum of the residues for both the real and imaginary remain finite (see Figure 3.4c-d) [28].

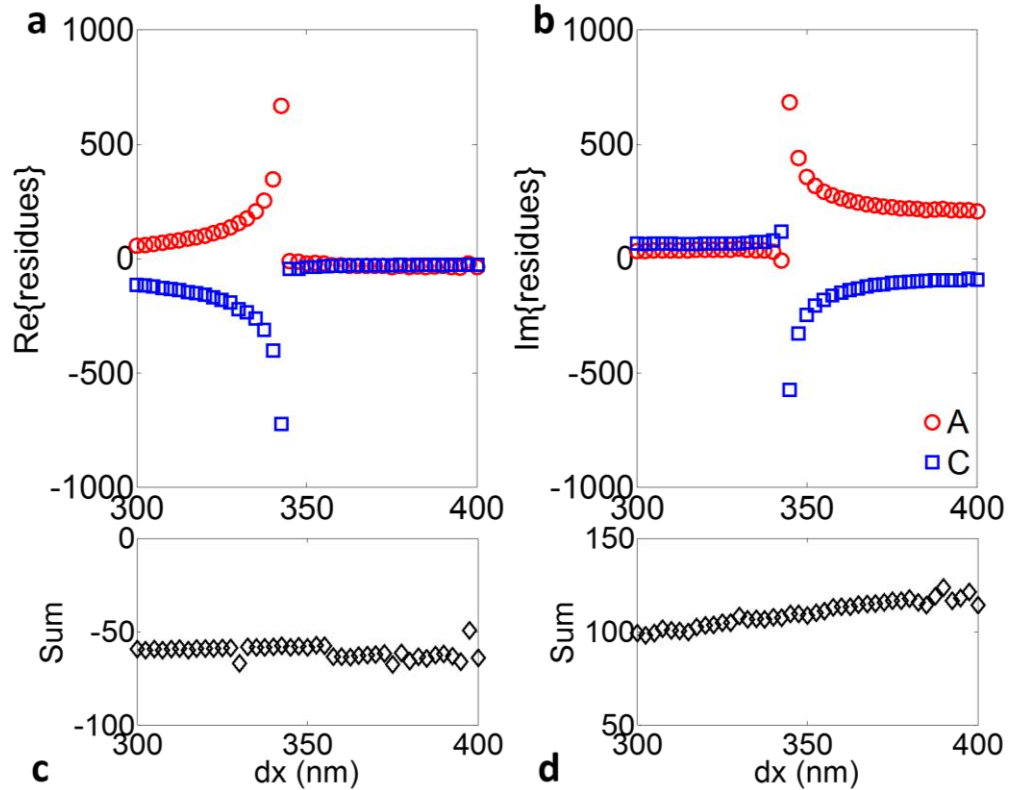


Figure 3.4: Residues of the corresponding modes A (\circ) and C (\square) as a function of shift, dx , for $dz=61$ nm. (a) Real and (b) Imaginary parts of the residues diverging when approaching the EP ($dx=345$ nm). Sum of the (c) real and (d) imaginary parts of the residues which remain finite.

3.5 EPs with Multiple ($N>1$) Coupled Resonators and Five-bar System

Furthermore, an EP is not exclusive to the three-bar system. An EP can also be realized in systems with more plasmonic resonators in a given unit cell. Here, we address the general case of having an odd number of bars ($N=2n+1$) in a unit cell and once again guided by an $N \times N$ closed system Hamiltonian. In general, for such a matrix of order N , there are $\lfloor N/2 \rfloor$ even and $\lfloor N/2 \rfloor$ odd eigenvectors. These eigenvectors are alternately even and odd with eigenvalues arranged in descending order given that the eigenvalues are distinct. The resulting eigenvectors of eigenvalues (see Eq. 3) can be expressed as

$$(\mathbf{u} \quad \alpha \quad +\mathbf{J}\mathbf{u})^T \quad (\text{even eigenvectors}) \quad (15)$$

$$(\mathbf{u} \quad 0 \quad -\mathbf{J}\mathbf{u})^T \quad (\text{odd eigenvectors})$$

Here, \mathbf{J} is the exchange matrix [24]. Note for an odd eigenvector, there is no excitation or field in the central bar as was the case for Mode B earlier.

As an example, we take the case with five coupled bars ($n=2$) described by 5x5 Hamiltonian, \mathbf{H}_0 , written as follows when all bars are perfectly aligned in the z -direction, *i.e.* $dx=0$.

$$\mathbf{H}_0 = \begin{pmatrix} \omega_0 & \kappa_n & \kappa_{n2} & 0 & 0 \\ \kappa_n & \omega_0 & \kappa_n & \kappa_{n2} & 0 \\ \kappa_{n2} & \kappa_n & \omega_0 & \kappa_n & \kappa_{n2} \\ 0 & \kappa_{n2} & \kappa_n & \omega_0 & \kappa_n \\ 0 & 0 & \kappa_{n2} & \kappa_n & \omega_0 \end{pmatrix} \quad (16)$$

Here, we can neglect the coupling terms κ_{n3} and κ_{n4} as they are simply dominated by κ_n and κ_{n2} . Similar to the three-bar case, we must choose physical parameters to modify so as to weaken κ_n and strengthen κ_{n2} . In order to retain the bisymmetric nature of the Hamiltonian, we note that all nearest-neighbor and next-to-nearest-neighbor coupling terms need to be the same as you modify the geometry of the system in accordance with the two constraints outlined earlier. Therefore, we concurrently shift the top, middle and the bottom bars in the x -direction which satisfies this condition and appropriately modifies κ_n and κ_{n2} . For an order $N=5$, there are three even and two odd eigenvectors. For an EP, we focus our attention on interaction between two of the even modes. The two parameters are still the inter-spacing, dz , along the z -direction and shift, dx (see Figure 3.5). Similar to the three-bar case, we observe resonances crossing in frequency and an avoided crossing in linewidths as evidence of an EP. An EP occurs at a frequency of ~ 227 THz for a 345 nm lateral shift of the bars and an inter-particle spacing, dz , close to 42 nm. This approach is general and

can be utilized to engineer an EP in coupled nanoresonator structures which can be physically realized [29].

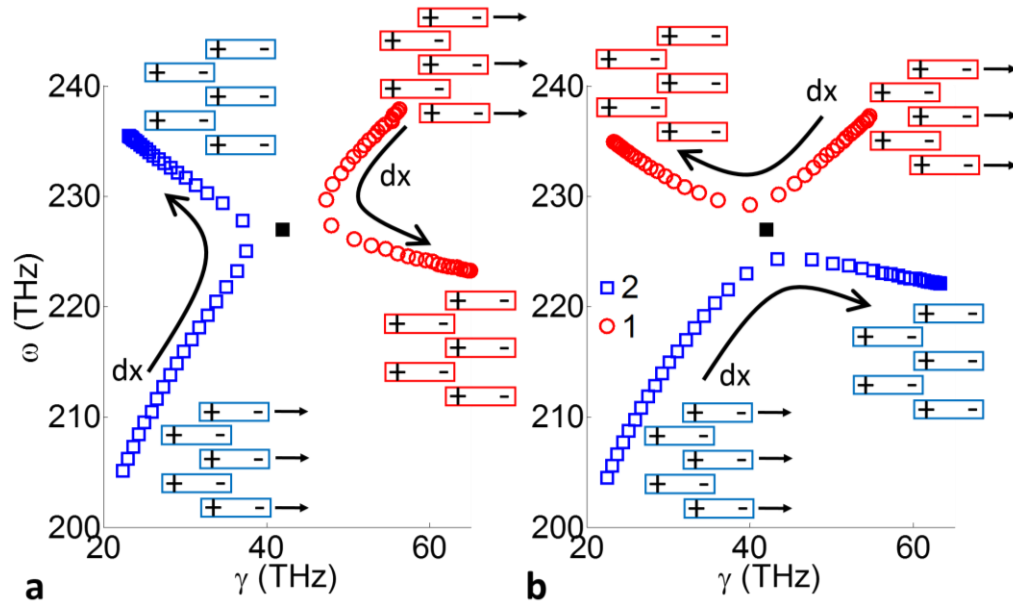


Figure 3.5: Realization of an exceptional point in a system with 5 bars ($2n+1$ with $n=2$) with top, middle and bottom bars shifted by dx (300 to 400 nm) for $dz=42$ nm and 43 nm. Mode 1 (\circ) and Mode 2 (\square): two modes of shared symmetry interact to form an EP (\blacksquare) at a value of d between 42 and 43 nm for a dx of ~ 345 nm. (a) For $dz=42$ nm, the resonance frequencies of modes 1 and 2 cross as the bars, indicated by arrows, are shifted (dx) but the linewidths are avoided whereas (b) for $dz=43$ nm, the linewidths cross and the resonance frequencies are avoided. See Appendix B2 for full scattering parameters for five-bar system.

3.6 Concluding Remarks

We have demonstrated the existence of exceptional points in three dimensional systems of coupled plasmonic nanostructures. The EP is constructed by coalescing symmetry-compatible modes and its existence is further evident from the diverging complex residues in the vicinity of the EP singularity. A thorough discussion on the importance of mode symmetries for EPs was presented.

The general approach to designing EPs in systems of coupled resonators proposed here can be used to construct EPs of higher order in physical systems where more than two modes coalesce. These ideas could be applied to other areas of wave physics such as acoustic and matter waves. We believe this work paves the way to the experimental observation of exceptional points in various physical systems and will foster further research towards unprecedented sensing schemes. With the experimental progress presented in Chapter 2 for the plasmonic shift-bar system, an experimental demonstration of an EP in a plasmonic system is soon to come.

Chapter 3, in part, is a reprint of the material as it appears in A. Kodigala, T. Lepetit, and B. Kanté, "Exceptional points in three-dimensional plasmonic nanostructures," *Physical Review B* **94**, 201103(R) (2016). The dissertation author was the primary researcher and author of this paper.

References

1. N. Moiseyev, *Non-Hermitian Quantum Mechanics* (Cambridge University Press, United Kingdom 2011).
2. T. Kato, *Perturbation Theory of Linear Operators* (Springer, Berlin 1966).
3. W.D. Heiss, "The physics of exceptional points," *J. Phys. A: Math. Theor.* **45**, 444016 (2012).
4. L. Feng, Z. J. Wong, R-M. Ma, Y. Wang, and X. Zhang, "Single-mode laser by parity-time symmetry breaking," *Science* **346**, 6212 (2014).
5. H. Hodaei, M-A. Miri, M. Heinrich, D. N. Christodoulides, M. Khajavikhan, "Parity-time-symmetric microring lasers," *Science* **346**, 6212 (2014).

6. B. Peng, S. K. Ozdemir, S. Rotter, H. Yilmaz, M. Liertzer, F. Monifi, C. M. Bender, F. Nori, L. Yang, "Loss-induced suppression and revival of lasing," *Science* **346**, 6207 (2014).
7. D. C. Marinica, S. V. Shabanov, and A. G. Borisov, "Bound States in the Continuum in Photonics," *Phys. Rev. Lett.* **100**, 183902 (2008).
8. A. Kodigala, T. Lepetit, Q. Gu, B. Bahari, Y. Fainman, B. Kanté, "Lasing action from photonic bound states in continuum," *Nature* **541**, 196 (2017).
9. A. Lovera, B. Gallinet, P. Nordlander, and O. J. F. Martin, "Mechanisms of Fano Resonances in Coupled Plasmonic Systems," *ACS Nano* **7**, 4527 (2013).
10. J. Wiersig, "Enhancing the Sensitivity of Frequency and Energy Splitting Detection by Using Exceptional Points: Application to Microcavity Sensors for Single-Particle Detection," *Phys. Rev. Lett.* **112**, 203901 (2014).
11. A. M. Armani, R. P. Kulkarni, S. E. Fraser, R. C. Flagan, K. J. Vahala, "Label-Free, Single-Molecule Detection with Optical Microcavities," *Science* **317**, 783 (2007).
12. H. Hodaei, A. U. Hassan, S. Wittek, H. Garcia-Garcia, R. El-Ganainy, D. N. Christodoulides, and M. Khajavikhan, "Enhanced sensitivity at higher-order exceptional points," *Nature* **548**, 192 (2017).
13. W. Chen, S. K. Ozdemir, G. Zhao, J. Wiersig, and L. Yang, "Exceptional points enhance sensing in an optical microcavity," *Nature* **548**, 187 (2017).
14. C. Dembowski, H.-D. Graf, H. L. Harney, A. Heine, W. D. Heiss, H. Rehfeld, and A. Richter, "Experimental Observation of the Topological Structure of Exceptional Points," *Phys. Rev. Lett.* **86**, 787 (2001).
15. T. Stehmann, W. D. Heiss, and F. G. Scholtz, "Observation of exceptional points in electronic circuits," *J. Phys. A: Math. Gen.* **37**, 7813 (2004).
16. S.-B. Lee, J. Yang, S. Moon, S.-Y. Lee, J.-B. Shim, S. W. Kim, J.-H. Lee, and K. An, "Observation of an Exceptional Point in a Chaotic Optical Microcavity," *Phys. Rev. Lett.* **103**, 134101 (2009).
17. Y. Choi, S. Kang, S. Lim, W. Kim, J.-R. Kim, J.-H. Lee, and K. An, "Quasieigenstate Coalescence in an Atom-Cavity Quantum Composite," *Phys. Rev. Lett.* **104**, 153601 (2010).
18. E. Prodan, C. Radloff, N. J. Halas, P. Nordlander, "A Hybridization Model for the Plasmon Response of Complex Nanostructures," *Science* **302**, 419 (2003).
19. P. B. Johnson and R. W. Christy, "Optical Constant of the Noble Metals," *Phys. Rev. B* **6**, 4370 (1972).

20. S. Fan, W. Suh, and J.D. Joannopoulos, "Temporal coupled-mode theory for the Fano resonance in optical resonators," *J. Opt. Soc. Am. A* **20**, 569 (2003).
21. T. Lepetit and B. Kanté, "Controlling multipolar radiation with symmetries for electromagnetic bound states in the continuum," *Phys. Rev. B* **90**, 241103(R) (2014).
22. F-M. Dittes, "The decay of quantum systems with a small number of open channels," *Phys. Rep.* **339**, 215 (2000).
23. A. Kodigala, T. Lepetit, and B. Kanté, "Engineering Resonance Dynamics of Plasmon Hybridized Systems," *J. Appl. Phys.* **117**, 023110 (2015).
24. A. Cantoni and P. Butler, "Eigenvalues and Eigenvectors of Symmetric Centrosymmetric Matrices," *Linear Algebra and Its Applications* **13**, 275-288 (1976).
25. B. Kanté, S.N. Burokur, A. Sellier, A. de Lustrac, and J.-M. Lourtioz, "Controlling Plasmon hybridization for negative refraction metamaterials," *Phys. Rev. B* **79**, 075121 (2009).
26. W. D. Heiss and R. G. Nazmitdinov, "Resonance scattering and singularities of the scattering function," *Eur. Phys. J. D* **58**, 53-56 (2010).
27. H. Cartarius, J. Main, and G. Wunner, "Exceptional Points in the spectra of atoms in external fields," *Phys. Rev. A* **79**, 053408 (2009).
28. J. Fuchs, J. Main, H. Cartarius, and G. Wunner, "Harmonic inversion analysis of exceptional points in resonance spectra," *J. Phys. A: Math. Theor.* **47**, 125304 (2014).
29. B. Kanté, Y.-S. Park, K. O'Brien, D. Shuldman, N. D. Lanzillotti-Kimura, Z. J. Wong, X. Yin, and X. Zhang, "Symmetry breaking and optical negative index of closed nanorings," *Nat. Commun.* **3**, 1180 (2012).

Chapter 4

Lasing from Photonic Bound States in the Continuum (BICs)

4.1 Introduction

In 1929, only three years after the advent of quantum mechanics, von Neumann and Wigner showed that Schrödinger's equation can have bound states above the continuum threshold [1]. These peculiar states, called bound states in the continuum (BICs), manifest themselves as resonances that do not decay. For several decades afterwards the idea lay dormant, regarded primarily as a mathematical curiosity. In 1977, Herrick and Stillinger revived interest in BICs when they suggested that BICs could be observed in semiconductor superlattices [2, 3]. BICs arise naturally from Feshbach's quantum mechanical theory of resonances, as explained by Friedrich and Wintgen, and are thus more physical than initially realized [4]. Recently, it was realized that BICs are intrinsically a wave phenomenon and are thus not restricted to the realm of quantum mechanics. They have since been shown to occur in many different fields of wave physics including acoustics, microwaves and nanophotonics [5-16]. However, experimental observations of BICs have been limited to passive systems and the realization of BIC lasers has remained elusive. Here we report, at room temperature, lasing from an optically pumped BIC cavity. Our results show that the lasing wavelength of the fabricated BIC cavities, each made of

an array of cylindrical nanoresonators suspended in air, scales with the radii of the nanoresonators according to the theoretical prediction for the BIC mode. Moreover, lasing from the designed BIC cavity persists even after scaling down the array to as few as 8-by-8 nanoresonators. BIC lasers open up new avenues in the study of light–matter interaction because they are intrinsically connected to topological charges [17] and represent natural vector beam sources (that is, there are several possible beam shapes) [18], which are highly sought after in the fields of optical trapping, biological sensing and quantum information.

Cavities play a fundamental role in wave phenomena from quantum mechanics to electromagnetism and dictate the spatiotemporal physics of lasers. In general, they are constructed by closing all channels through which waves can escape. We report, at room temperature (295 K), a BIC laser that harnesses optical modes residing in the radiation continuum but, nonetheless, possess arbitrarily high quality factors, Q . These counterintuitive cavities are based on resonance-trapped, symmetry-compatible modes that destructively interfere.

Generally, open systems are described by non-Hermitian effective Hamiltonians that have multivariate and complex eigenvalues describing modes of the system. These eigenvalues exist in a multidimensional hyperspace but, in a given frequency range, the investigation can be reduced to a finite number of variables, thus limiting the complexity of the effective Hamiltonian [7]. When eigenvalues come close to crossing as a function of a geometrical parameter that modifies the system, avoided resonance crossing occurs, that is, eigenvalues repel each other in the entire complex plane [19-21]. Friedrich and Wintgen showed that resonance-trapped BICs represent a particular type of avoided resonance crossing for which coupling occurs predominantly in the far-field.

4.2 BIC Cavity Design

Our system consists of a thin membrane of semiconductor material suspended in air. We subsequently structure the membrane at the nanometer scale. The field in the air is a superposition of independent waves, which are interpreted as decay channels, and can be either propagating or evanescent. The field in the membrane, which becomes a superposition of coupled waves owing to structuring, is also coupled to the field in air. In the resulting open system described by a non-Hermitian Hamiltonian, the imaginary part of the complex eigenfrequency serves to quantify the decay of modes via the resonance lifetime. This lifetime is governed by coupling amongst different waves within the membrane through the Fourier coefficients of the periodic permittivity. A precise engineering of coupling among relevant waves in reciprocal space can lead to total destructive interference, that is, an infinite lifetime. BICs arise in the limit when a complex eigenfrequency mode tend towards a purely real eigenfrequency mode. They are very peculiar discrete modes in that they are actually embedded within the continuous spectrum but intrinsically possess an infinitely high radiation quality factor as a result of their non-decaying nature. BICs are thus ideally suited for the design of perfect nanophotonic cavities.

As shown in Figure 4.1, our BIC cavity is composed of a periodic array of nanoresonators of radius R interconnected by a network of supporting bridges used for the mechanical stability of the system. The membrane consists of several $\text{In}_x\text{Ga}_{1-x}\text{As}_y\text{P}_{1-y}$ multiple quantum wells, specially designed to operate around the telecommunication wavelength ($\lambda \approx 1.55 \mu\text{m}$). The radius of the cylindrical nanoresonators is the only parameter

we use to tune the modes of the membrane and alter the effective Hamiltonian. The structure is fabricated using electron-beam lithography and reactive ion etching to define the cylindrical nanoresonators, followed by a wet etching step to create the membrane (see Chapter 5). It is worth noting that the radii of the fabricated nanoresonators are always smaller than their nominal design values, a consequence of reactive ion etching. As a result, the maximum achievable radius is strictly smaller than $a/2$ where a is the period of our structure.

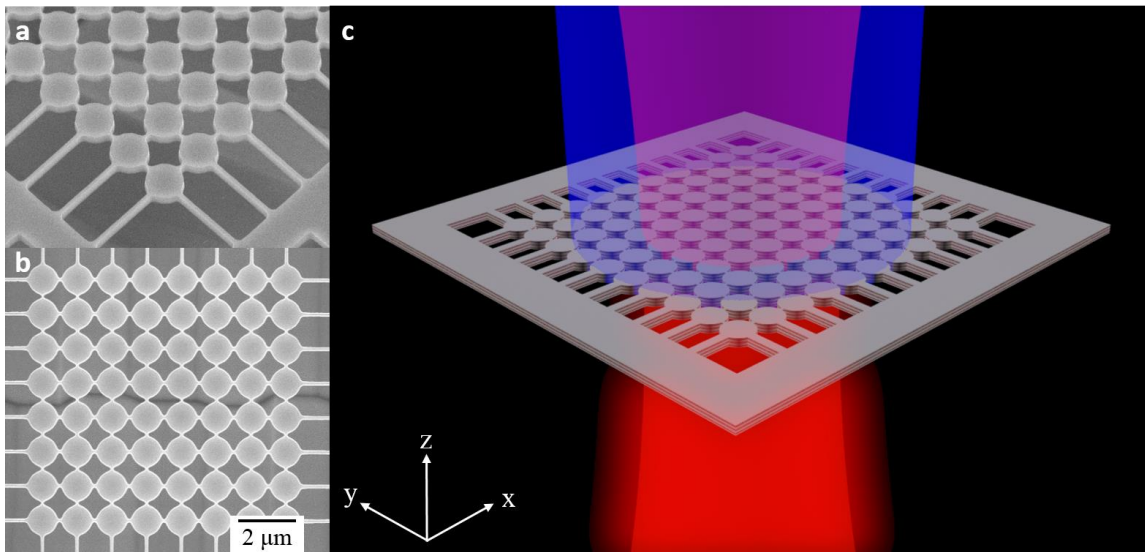


Figure 4.1: (a) Tilted electron micrograph of InGaAsP multiple quantum wells cylindrical nanoresonator array suspended in air. All structures are fabricated using electron beam lithography followed by reactive ion etching to form the cylinders. We subsequently use wet etching to suspend the structure (see Chapter 5 for details). (b) Top view of an 8-by-8 array with supporting bridges, which are used for the mechanical stability of the membrane. The dimensions of the structure are the period (1200 nm), the thickness (300 nm) and the bridge width (200 nm). (c) Schematic of the fabricated system illustrating the pump beam (blue) and lasing from the BIC mode (red). The radius of the cylindrical nanoresonators is the key parameter in our BIC design.

4.3 Diverging Quality Factor (Q) at BIC Singularity

To analyze our system, we calculate the quality factors at normal incidence around $1.55 \mu\text{m}$, that is, within the gain bandwidth of the material. The system was modelled using

a three-dimensional finite element-method eigenfrequency solver. We restrict the discussion to odd modes (transverse-magnetic-like) as they have much higher quality factors than even modes (transverse-electric-like) in the wavelength range of interest (see Appendix C1). We find three modes around $1.55 \mu\text{m}$ with appreciable quality factors, one doubly degenerate mode (modes 1 and 2) and one singly degenerate mode (mode 3). Figure 4.2a shows their quality factor as a function of the radius ($522 \text{ nm} \leq R \leq 534 \text{ nm}$). The quality factor of mode 3 is independent of the radius and remains high throughout the calculated range. This mode corresponds to a symmetry-protected mode [22]. In contrast, the quality factor of modes 1 and 2 depends strongly on the radius and reaches a maximum at an optimum radius of $R_{\text{opt}} = 528.4 \text{ nm}$. At this optimum radius, modes 1 and 2 completely decouple from the radiation continuum and thus become BICs. This mode corresponds to a resonance-trapped mode (see Appendix C2).

The quality factor can diverge in two different situations. In the first situation (mode 3), coupling to the outside vanishes solely as a result of symmetry mismatch. Any perturbation that preserves symmetry, such as a modification of the radius, has no impact on its quality factor. This type of mode has been extensively studied before [23]. In the second situation (modes 1 and 2), coupling to the outside vanishes as a result of total destructive interference [13, 24]. This BIC mode (resonance-trapped) is fundamentally different from previous works on band-edge lasers [25-27] (symmetry-protected) that are restricted to high symmetry points of the reciprocal lattice. Resonance-trapped BICs achieve an infinite quality factor at the singular radius R_{opt} but the quality factor remains very high for radii around R_{opt} . Figure 4.2b shows the transmission spectrum at normal

incidence of our structure, in which the quality factor of modes 1 and 2 can be seen to tend slowly to infinity from its vanishing linewidth.

Figure 4.2c shows the dispersion relation of the BIC structure at $R = R_{\text{opt}}$ along the $M\Gamma$ and ΓX directions. Here Γ , X, and M are high-symmetry points of the first Brillouin zone for a square lattice. We also plot the complex dispersion relation of modes 1 and 2 (Figure 4.2d, e) and mode 3 (Figure 4.2f). Figure 4.2f shows that mode 3 is extremely sensitive to symmetry-breaking perturbations as its quality factor drops sharply away from the Γ point. Quality factors of modes 1 and 2, which are no longer degenerate away from the Γ point (as seen in Figure 4.2c), do not drop as sharply as that of mode 3. Modes 1 and 2 are thus much less sensitive to symmetry-breaking perturbations. Additionally, the resonance-trapped BIC is robust because a variation in radius only induces its displacement in k -space (reciprocal space, where k is the wavevector), whereas a symmetry breaking perturbation destroys the symmetry-protected mode [13]. This is of utmost importance in device design as fabrication tolerances will have less impact on resonance-trapped BICs than on modes that rely on symmetry protection. Moreover, designing a mode with a high quality factor in a large region of k -space is of practical importance because fabricated devices, which are never spatially infinite, always sample the dispersion relation in a finite neighborhood in k -space [28]. Therefore, for a given quality factor, we can achieve a much smaller device footprint with a resonance-trapped BIC mode than with symmetry-protected modes.

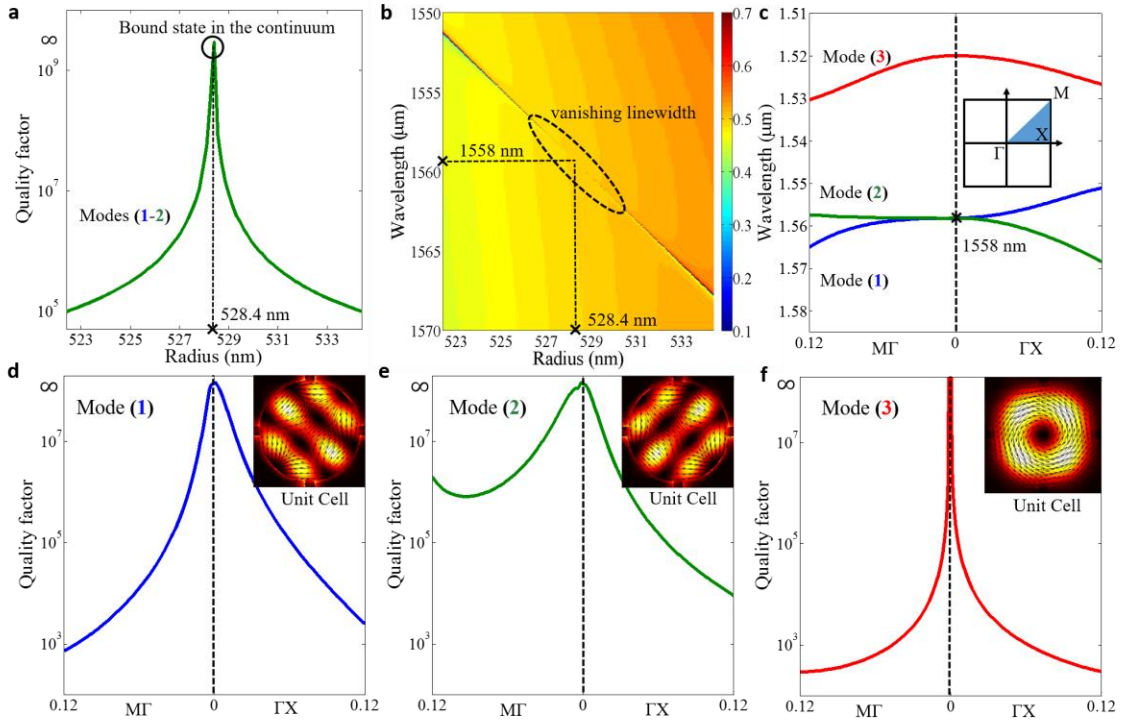


Figure 4.2: (a) Quality factor of high- Q modes at the Γ point around the telecommunication wavelength for different nanoresonator radii. The quality factors of modes 1 and 2, which are doubly degenerate at the Γ point, are strongly dependent on the radius R . For $R = R_{\text{opt}}$ at 528.4 nm, this quality factor approaches infinity to form a resonance-trapped BIC. For radii around R_{opt} the quality factor remains very high. (b) Transmission spectrum at normal incidence showing the vanishing linewidth of modes 1 and 2 when the radius approaches R_{opt} . The wavelength of the modes is a function of the radius and it continuously varies between the smallest radius ($R = 522$ nm) and the largest radius ($R = 534$ nm). (c) Dispersion relation around $1.55 \mu\text{m}$ for high- Q modes (1, 2 and 3) in both $M\Gamma$ and ΓX directions as a function of $k(a/2\pi)$. The inset shows the first Brillouin zone of the square lattice and irreducible contour for cylindrical nanoresonators (shaded area). The contour connects high-symmetry points Γ , X , and M . (d–f) Quality factor of high- Q modes in both the $M\Gamma$ and the ΓX direction for mode 1 (d), mode 2 (e), and mode 3 (f). Insets represent the normalized electric field on the surface of a unit cell. Modes 1 and 2 are identical under 90-degree rotation. Mode 3 is a symmetry-protected mode and is thus not affected by geometrical changes that preserve symmetry, such as the change of radius. The quality factor of mode 3, however, drops rapidly away from the high-symmetry point Γ . It drops more rapidly compared to the quality factor of modes 1 and 2. The sharper drop of the quality factor of mode 3 away from Γ implies that the integrated quality factor of this mode will be smaller than those of modes 1 and 2 in the case of finite-sized samples.

4.4 Device Characterization

To experimentally demonstrate lasing from our BIC cavity, we optically pump the membranes at room temperature with a pulsed laser ($\lambda = 1064 \text{ nm}$, $T = 12 \text{ ns}$ pulse at a repetition rate $f = 300 \text{ kHz}$) using a micro-photoluminescence setup and record the resulting spectral emission (see Figure 4.3). A 20x long working distance microscope objective with a numerical aperture (NA) of 0.4 is used to focus the pump beam and simultaneously collect the emission from the sample. To minimize chromatic aberration, a telescope is introduced (lenses L-6 and L-7) to adjust the divergence of the pump beam such that the focal planes of the pump and emission wavelengths coincide. Using a double 4-f imaging system in conjunction with a pump filter, laser structures are either imaged onto an IR CCD camera (Indigo Alpha NIR), or spectroscopically measured with a monochromator (CVI Digikrom DK480) in conjunction with a cooled InGaAs detector in lock-in detection configuration. The monochromator can resolve a linewidth of $\sim 0.33 \text{ nm}$.

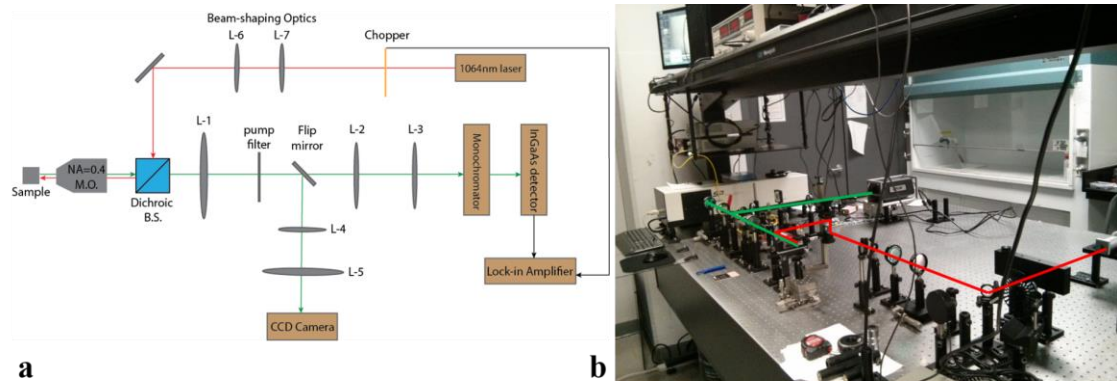


Figure 4.3: (a) Micro-photoluminescence (PL) setup used to measure laser emission from BIC lasers. Red color connection represents the pump path; green color connection represents the collection/imaging path; and black color connection represents electrical cables. The microscope objective (M.O.) with L-1,2,3 and L-1,4,5 compose a double 4-f imaging system for the IR CCD Camera and the monochromator, respectively. (b) Photograph of the micro-PL setup including laser in the far-right, IR camera, and monochromator.

4.5 Lasing from an Optically Pumped BIC Cavity

Figure 4.4a shows the evolution of the output power as a function of both the pump power and the wavelength. At low pump power, we observe a spectrally broad photoluminescence spectrum, while at high pump power, we observe a drastic overall suppression of the photoluminescence in favor of one extremely narrow peak, that is, lasing. As depicted in Figure 4.4a, three modes show amplification at first ($P_{\text{pump}} \approx 48 \mu\text{W}$) but, ultimately, only one remains. Lasing occurs at a wavelength of 1551.4 nm with a detection-limited linewidth of about 0.33 nm (see inset of Figure 4.4b). Figure 4.4b shows the evolution of the output power as a function of the pump power around this lasing wavelength. We observe a clear threshold behavior with a threshold power of 56 μW or a density of 140 mW mm^{-2} .

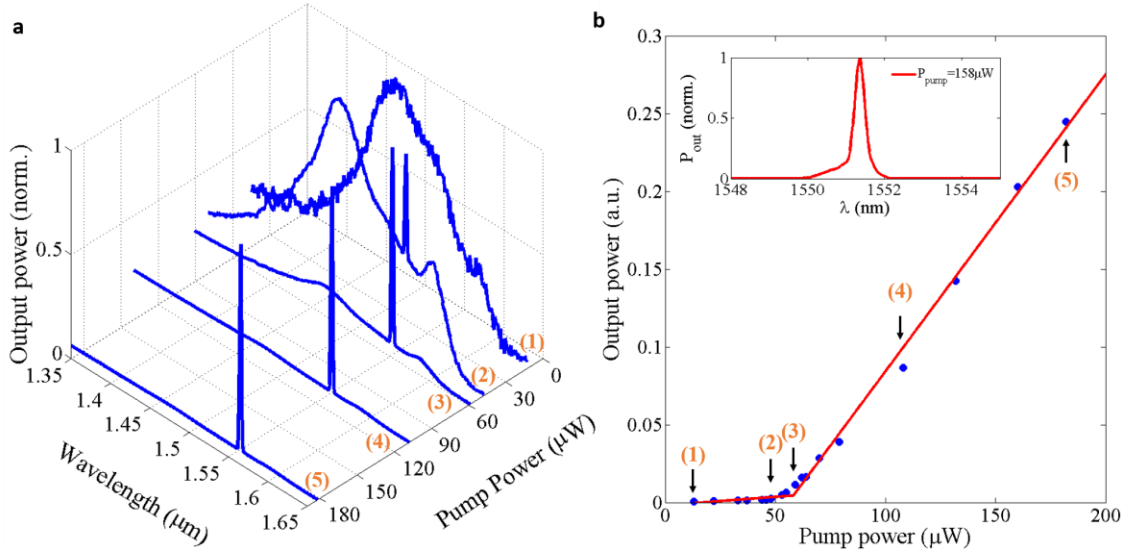


Figure 4.4: (a) Evolution of the normalized output power as a function of both wavelength (μm) and pump power (μW) for a 16-by-16 array with a nanoresonator radius of 525 nm. We observe the transition from a broad spontaneous emission to a single lasing peak at 1551.4 nm. (b) Output power as a function of the average pump power (light-light curve) around the lasing wavelength. We observe the onset of lasing at a threshold power of 56 μW . The red lines are linear fit to the data indicating the regions of spontaneous and stimulated emission. The blue dots correspond to measurements and numbers 1 through 5 denote spectra plotted in (a) (see Appendix C4 for emission power estimate). The inset shows the lasing spectrum at a pump power of 158 μW with a measured linewidth of ~ 0.33 nm (detection limited).

4.6 Robustness and Scaling of BIC Lasers

To further demonstrate the robustness and scalability [29, 30] of the BIC lasers, we fabricated several devices (36 devices) with a range of radii and array sizes as seen in Figure 4.5a. Figure 4.5b shows the measured lasing wavelength of devices of different array size (8-by-8, 10-by-10, 16-by-16 and 20-by-20), and different radii of nanoresonators. The solid and dashed lines represent, respectively, the theoretical resonant wavelength of modes 1 and 2 and mode 3 for different radii of nanoresonators in the infinite array. We observe a very good agreement between the experimental lasing wavelengths and the theoretical resonant wavelengths of the resonance-trapped BIC mode (modes 1 and

2). This agreement confirms that lasing is indeed from the BIC mode over the entire range of radii. Moreover, the persistence of lasing for all array sizes down to as few as 8-by-8 nanoresonators shows the scalability of our BIC laser, thanks to the large quality factor of the resonance-trapped BIC mode in a wide region of k -space.

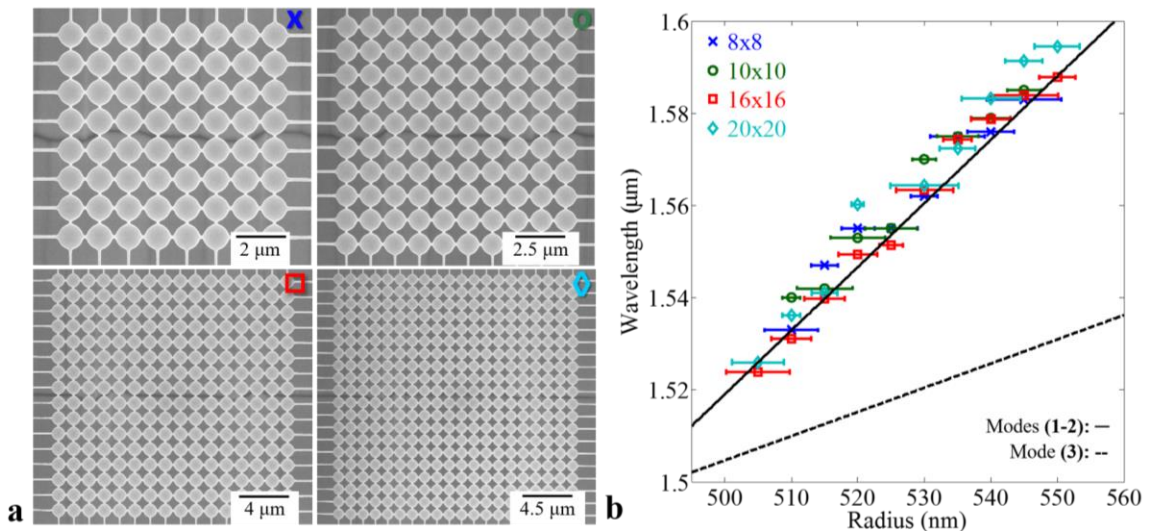


Figure 4.5: (a) Electron micrographs of fabricated BIC lasers of size 8-by-8, 10-by-10, 16-by-16, and 20-by-20. (b) Lasing wavelength as a function of nanoresonator radius, from 500 nm to 550 nm, with array sizes of 8-by-8 (cross), 10-by-10 (circle), 16-by-16 (square), and 20-by-20 (diamond). Each point corresponds to a device with a specific radius, bridge width and array size. Error bars indicate the standard deviation of radii measured from fabricated devices. The lines represent the theoretical resonant wavelength of modes 1 and 2 (solid line) and 3 (dashed line) for different radii of nanoresonators, for the infinite array. The good agreement between the experimental lasing wavelengths and the theoretical resonant wavelengths of the resonance-trapped BIC mode (modes 1 and 2) confirms that lasing is indeed from the BIC mode.

4.7 Lasing Threshold at BIC Singularity

Further evidence of lasing from the BIC mode can directly be observed in the measured threshold power of the lasers. The threshold power has a clear minimum close to R_{opt} (about 525 nm), reflecting a maximum quality factor at the BIC singularity as seen in

Figure 4.6. The inverse relationship between quality factor and threshold is evident here in comparison to Figure 4.2a.

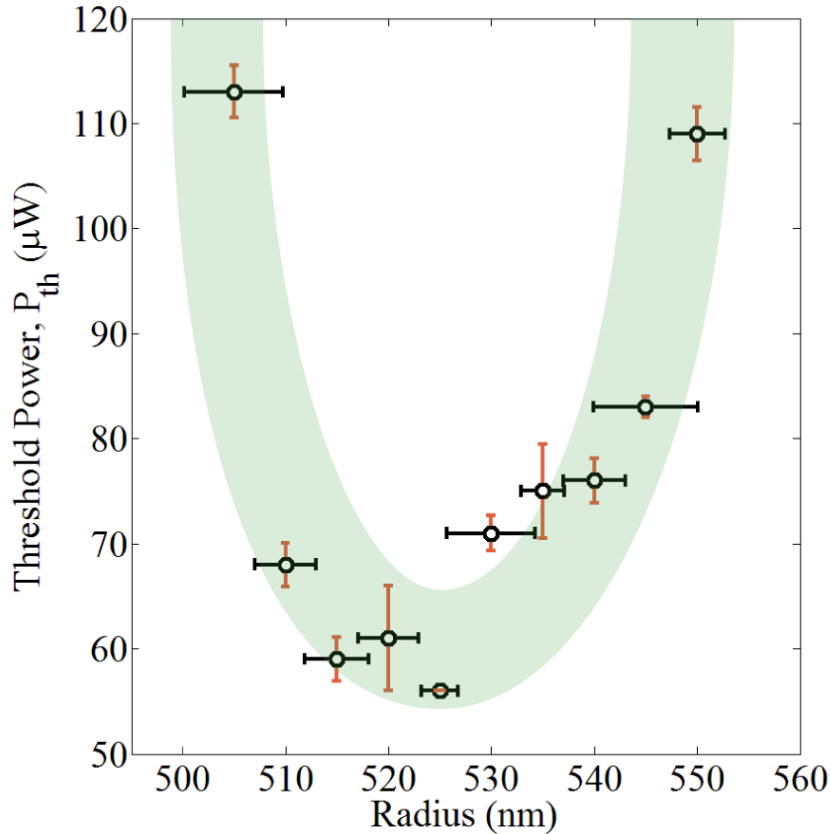


Figure 4.6: Measured laser threshold power as a function of radii for the lasers clearly shows a minimum ($56 \mu\text{W}$) close to R_{opt} (about 525 nm) reflecting the maximum quality factor around the BIC singularity and offers further proof of lasing from the BIC mode (modes 1 and 2). The inverse relationship between quality factor and threshold is evident. Mode 3 has no variation in quality factor with radii. The vertical error bars are the standard error in the threshold power estimated over multiple measurements (varying pump power) repeated more than three times whereas the horizontal error bars represent the standard deviation of measured radii. The green shaded area is a guide to the eye.

4.8 Threshold Power Density versus Cavity Size

Similarly, in these laser devices, the effect on the quality factor as a function of array size is easily discernible from the measured laser threshold powers. Here, we

uniformly pump lasers of varying size and compare their threshold power densities (see Figure 4.7 below). For any given radius, the lasing threshold power density, P_{th} , decreases with increasing array size, N . This is clearly indicative of an increase in the quality factor as the laser array size increases [30]. Furthermore, the material loss contribution to lasing threshold power is intrinsic to all lasers. Ideally, at the BIC singularity, the material loss is the only significant loss mechanism as the array size approaches infinity. Additional characterization such as far-field profiles and polarization measurements of these lasing devices are provided in Appendix C3.

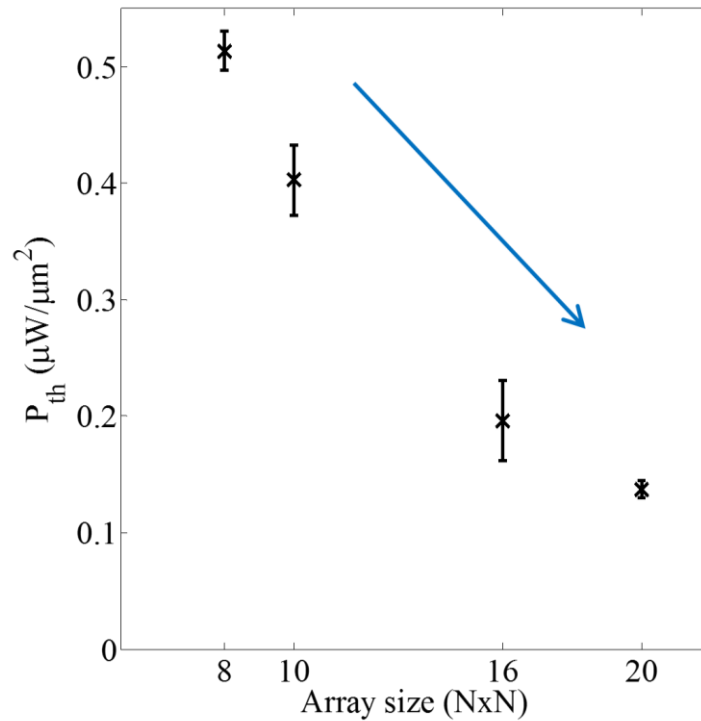


Figure 4.7: Lasing threshold power densities, P_{th} ($\mu\text{W}/\mu\text{m}^2$), as a function of laser array size, N , for a given resonator radius ($R=530$ nm). The effect on the quality factor due to the finiteness of the laser arrays is evident from the decreasing lasing thresholds with increasing size. As the array size increases, the cavity more closely resembles that of an infinite structure. This effect is observable irrespective of the resonator radius. The vertical error bars are the error in the threshold power over multiple measurements.

4.9 Linewidth of BIC Lasers

Linewidth of lasers generally arises from phase fluctuations in their output from mainly two sources: spontaneous emission, which is inherent in all lasers, and carrier density fluctuations which is relevant in the case of semiconductor lasers such as the ones presented here. For carrier density fluctuations, there is a proportionality between the frequency shift of the laser due to a change in carrier density, ΔN , termed the linewidth enhancement factor, α [31].

We report, in Figure 4.8a below, linewidths well above lasing threshold as a function of varying radii. There is evidence to suggest that lasers operating close to the BIC singularity also have a minima in their linewidths similar to their threshold powers (*i.e.* diverging Q) in agreement with the modified Schawlow–Townes formulation for semiconductor lasers [32, 33] (see equation below). The contribution from carrier density fluctuations is represented by α^2 and 1 represents the spontaneous emission contribution from the original Schawlow–Townes formulation [32].

$$\Delta\nu \propto (1 + \alpha^2) \frac{(\Delta\nu_c)^2}{P_{out}}$$

Here the laser linewidth, $\Delta\nu$, is directly proportional to the resonator bandwidth, $\Delta\nu_c$, which is reciprocally related to the cold-cavity, Q , with P_{out} being the output power. Hence, we expect the lasing linewidths to be minimal near the BIC point as evident from Figure 4.8a. Here lasers away from BIC point (~ 525 nm) with radii 505 and 550 nm have larger linewidths than the lasers operating near the BIC point. However, the measured

linewidths near the BIC point reach the resolution limit (~ 0.33 nm) of the monochromator. This can be seen in Figure 4.8b for linewidth evolution as a function of pump power for a device of radius 525 nm. Below threshold, when spontaneous emission is predominant, the linewidth narrows as the inverse of output power in agreement with Schawlow-Townes [32]. Around threshold, the rapid increase of the coupling between the gain coefficient and the refractive index of the gain medium slows down the narrowing of the linewidth [33, 34]. Above threshold, we once again reach the detection limit for this particular sample.

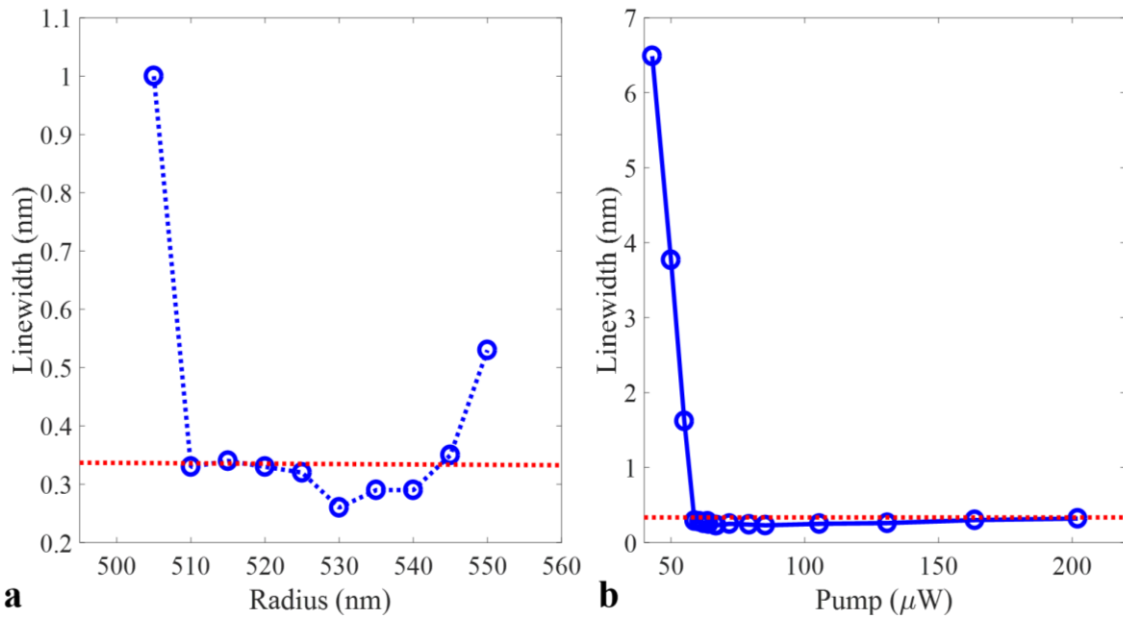


Figure 4.8: (a) Lasing linewidths for devices with varying radii at pump powers above threshold (blue markers). Laser linewidths near the BIC singularity have reached the resolution limit of ~ 0.33 nm indicated by the dotted line (red). (b) Lasing linewidth for device with $R \approx 525$ nm as a function of pump power below and above threshold (blue markers). The lasing threshold of this device is 56μ W. Below threshold, the linewidth narrows as you approach the lasing threshold in agreement with Schawlow-Townes linewidth formula. Lasing linewidths measured above threshold have reached the resolution limit of ~ 0.33 nm. These linewidth measurements are detection limited by a combination of the grating period, entrance/exit slit width of the monochromator, and resulting signal-to-noise ratio.

The above threshold linewidth behavior can be observed in a BIC laser sample operating far away from the BIC point as seen in Figure 4.9. Note that this sample is from

a separate fabrication run and was not included in the previous data set. Here, the above threshold laser linewidth is ~ 0.5 nm which is well above the detection limit of 0.33 nm. With increased pump power above threshold, there is only a slight increase in the laser linewidth as seen in Figure 4.9b. An exact relationship between carrier density fluctuations, α^2 , and output power, P_{out} , needs to be investigated to gain insight into the above threshold linewidth behavior of BIC lasers.

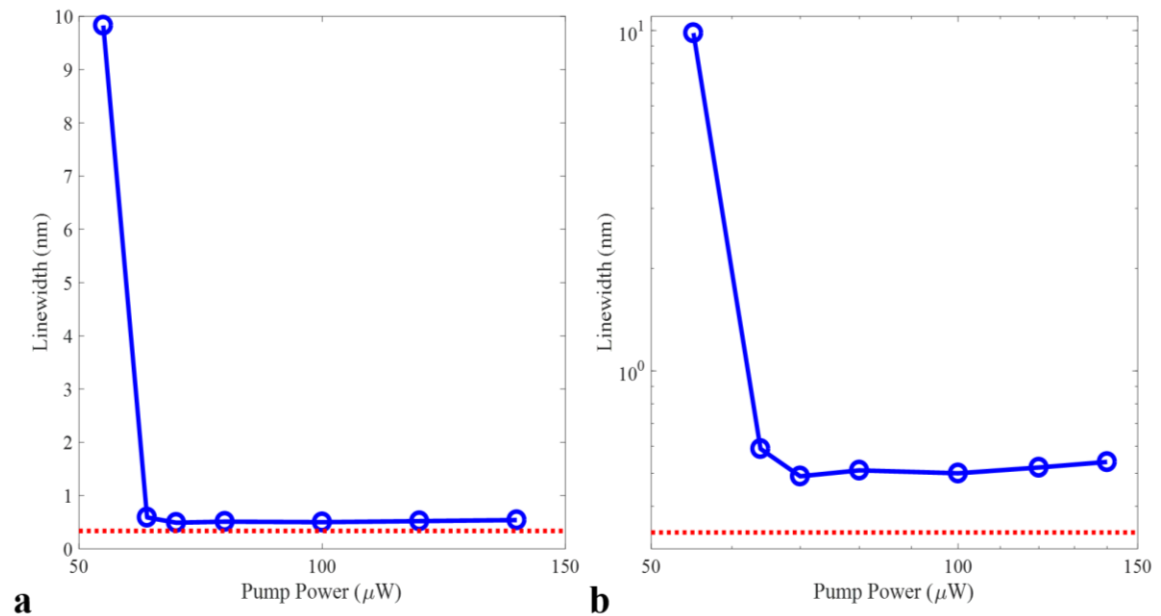


Figure 4.9: (a) Linewidth evolution of a laser away from BIC point as a function of pump power in linear scale and (b) log scale with a threshold of $\sim 62 \mu\text{W}$. The dotted line is the detection limit of ~ 0.33 nm. Laser linewidth above threshold is well above the detection limit.

An unambiguous linewidth measurement for cases below the current detection limit requires experimental modifications and is currently in progress.

4.10 Concluding Remarks

In this chapter, we have reported an optically pumped BIC laser operating at room temperature from a cavity mode that can, surprisingly, have arbitrarily high quality factors

despite being embedded in the continuum of radiation modes. This cavity, made of an array of suspended cylindrical nanoresonators, shows persistent single-mode lasing for various radii and array sizes. The lasing wavelength follows the theoretical prediction of the BIC mode and the inverse relationship between quality factor and lasing threshold is experimentally demonstrated. These results demonstrate the robustness and scalability of the system. The ability to confine light within the radiation continuum opens up the study of the intriguing topological physics of BICs and the realization of non-standard photonic devices, sensors and sources. Moreover, the development of an electrically pumped BIC laser, currently in progress, will help achieve these goals.

Chapter 4, in part, is a reprint of the material as it appears in A. Kodigala, T. Lepetit, Q. Gu, B. Bahari, Y. Fainman and B. Kanté, "Lasing action from photonic bound states in the continuum," *Nature* **541**, 196 (2017). The dissertation author was the primary researcher and author of this paper.

References

1. J. von Neumann and E. Wigner, "On some peculiar discrete eigenvalues," *Phys. Z* **30**, 467 (1929).
2. D. R. Herrick, "Construction of bound states in the continuum for epitaxial heterostructure superlattices," *Physica B* **85**, 44-50 (1977).
3. F. H. Stillinger, "Potentials supporting positive-energy eigenstates and their application to semiconductor heterostructures," *Physica B* **85**, 270-276 (1977).
4. H. Friedrich and D. Wintgen, "Interfering resonances and bound states in the continuum," *Phys. Rev. A* **32**, 3231 (1985).

5. C. W. Hsu, B. Zhen, A. Douglas Stone, J. D. Joannopoulos, and M. Soljacic, "Bound states in the continuum," *Nat. Rev. Mater.* **1**, 16048 (2016).
6. C. M. Linton and P. McIver, "Embedded trapped modes in water waves and acoustics," *Wave Motion* **45**, 16 (2007).
7. T. Lepetit and B. Kanté, "Controlling multipolar radiation with symmetries for electromagnetic bound states in the continuum," *Phys. Rev. B* **90**, 241103(R) (2014).
8. D. C. Marinica, A. G. Borisov, and S. V. Shabanov, "Bound states in the continuum in photonics," *Phys. Rev. Lett.* **100**, 183902 (2008).
9. E. N. Bulgakov and A. F. Sadreev, "Bound states in the continuum in photonic waveguides inspired by defects," *Phys. Rev. B* **78**, 075105 (2008).
10. F. Dreisow, A. Szameit, M. Heinrich, R. Keil, S. Nolte, A. Tunnermann, and S. Longhi, "Adiabatic transfer of light via a continuum in optical waveguides," *Opt. Lett.* **34**, 2405-2407 (2009).
11. Y. Plotnik, O. Peleg, F. Dreisow, M. Heinrich, S. Nolte, A. Szameit, and M. Segev, "Experimental observation of optical bound states in the continuum," *Phys. Rev. Lett.* **107**, 183901 (2011).
12. S. Weimann, Y. Xu, R. Keil, A. E. Miroshnichenko, A. Tunnermann, S. Nolte, A. A. Sukhorukov, A. Szameit, and Y. S. Kivshar, "Compact surface Fano states embedded in the continuum of waveguide arrays," *Phys. Rev. Lett.* **111**, 240403 (2013).
13. C. W. Hsu, B. Zhen, J. Lee, S-L. Chua, S. G. Johnson, J. D. Joannopoulos, and M. Soljacic, "Observation of trapped light within the radiation continuum," *Nature* **499**, 188-191 (2013).
14. F. Monticone and A. Alù, "Embedded photonic eigenvalues in 3D nanostructures," *Phys. Rev. Lett.* **112**, 213903 (2014).
15. M. Molina, A. E. Miroshnichenko, Y. S. Kivshar, "Surface Bound States in the Continuum," *Phys. Rev. Lett.* **108**, 070401 (2012).
16. M. Zhang and X. Zhang, "Ultrasensitive optical absorption in graphene based on bound states in the continuum," *Sci. Rep.* **5**, 8266 (2015).
17. B. Zhen, C. W. Hsu, L. Lu, A. Douglas Stone, and M. Soljacic, "Topological nature of optical bound states in the continuum," *Phys. Rev. Lett.* **113**, 257401 (2014).
18. E. Miyai, K. Sakai, T. Okano, W. Kunishi, D. Ohnishi, S. Noda, "Photonics: Lasers producing tailored beams," *Nature* **441**, 946 (2006).

19. A. F. Sadreev, E. N. Bulgakov, and I. Rotter, "Bound states in the continuum in open quantum billiards with a variable shape," *Phys. Rev. B* **73**, 235342 (2006).
20. J. Wiersig, "Formation of long-lived, scarlike modes near avoided resonance crossings in optical microcavities," *Phys. Rev. Lett.* **97**, 253901 (2006).
21. E. Persson, I. Rotter, H.-J. Stockmann, and M. Barth, "Observation of resonance trapping in an open microwave cavity," *Phys. Rev. Lett.* **85**, 2478 (2000).
22. K. Sakoda, *Optical Properties of Photonic Crystals*, 2005.
23. S. Fan and J. D. Joannopoulos, "Analysis of guided resonances in photonic crystal slabs," *Phys. Rev. B* **65**, 235112 (2002).
24. Y. Yang, C. Peng, Y. Liang, Z. Li, and S. Noda, "Analytical perspective for bound states in the continuum in photonic crystal slabs," *Phys. Rev. Lett.* **113**, 037401 (2014).
25. H. Kogelnik and C. V. Shank, "Stimulated emission in a periodic structure," *Appl. Phys. Lett.* **18**, 152 (1971).
26. M. Meier, A. Mekis, A. Dodabalapur, A. Timko, R. E. Slusher, J. D. Joannopoulos, O. Nalamasu, "Laser action from two-dimensional distributed feedback in photonic crystals," *Appl. Phys. Lett.* **74**, 7 (1999).
27. M. Imada, S. Noda, A. Chutinan, T. Tokuda, M. Murata, and G. Sasaki, "Coherent two-dimensional lasing action in surface-emitting laser with triangular lattice photonic crystal structure," *Appl. Phys. Lett.* **75**, 316 (1999).
28. T. Xu, S. Yang, S. V. Nair, and H. E. Ruda, "Confined modes in finite-size photonic crystals," *Phys. Rev. B* **72**, 045126 (2005).
29. A. F. Koenderink, A. Alu, and A. Polman, "Nanophotonics: Shrinking light-based technologies," *Science* **348**, 516-521(2015).
30. A. Taghizadeh and I-S. Chung, "Quasi bound states in the continuum with few unit cells of photonic crystal slabs," *Appl. Phys. Lett.* **111**, 031114 (2017).
31. L. A. Coldren, S. W. Corzine, and M. L. Mashanovitch, *Diode Lasers and Photonic Integrated Circuits*, Wiley (2nd Edition), 2012.
32. A. L. Schawlow, and C. H. Townes, "Infrared and optical masers," *Phys. Rev.* **112**, 1940 (1958).
33. C. H. Henry, "Theory of the linewidth of semiconductor lasers," *IEEE J. Quant. Electron.* **18**, 259-264 (1982).

34. M. Lax, "Classical noise. V. Noise in self-sustained oscillators," Phys. Rev. **160**, 290 (1958).

Chapter 5

Nanofabrication of Suspended PhC Lasing Membranes of InGaAsP Cylinders

5.1 Introduction

Membrane structures have attracted ample interest over the years from many disciplines with applications in micro-electro-mechanical systems (MEMS) [1], cavity opto-mechanics [2-4], and optical lasing [5, 6]. Depending on the application, diverse membrane materials are used with most applications resorting to silicon (Si) or dielectrics such as silicon nitride (Si_3N_4) and silicon dioxide (SiO_2) [7-11]. The fabrication process differs for each. Nevertheless, the processes are established, and standard membrane types are commercially available. However, applications pertaining to lasing require intricately patterned membranes and typically employ alloyed semiconductor gain material such as InGaAsP with quantum wells [12]. These membranes are periodically patterned into photonic crystals (PhCs) to highly confine light of certain wavelengths or, in other words, sustain high quality factor (Q) modes required for lasing [13, 14]. Thus, these membrane PhCs serve as optical cavities for lasers. Here, we construct photonic crystal cavities with InGaAsP that employ bound states in the continuum (BIC) for lasing [15-19]. Bound states in the continuum (BICs) are waves that exist within a continuum of radiating waves and

yet do not radiate or decay. Contrary to conventional wisdom, these states remain localized or bound to the cavity [20].

Unlike conventional PhCs that most often take the complimentary form, *i.e.* periodic array of holes, these suspended PhC cavities are composed of periodically spaced and interconnected cylinders. Furthermore, because the cylinders' radii are critical to the lasing mode in BIC lasers, stringent requirement is placed on fabrication precision. Hence, the fabrication of these new devices offers its own unique challenges which include maintaining pattern dimensionality while realizing a fully suspended and mechanically stable membranes. Here, we describe two different approaches of fabricating these BIC membrane lasers and their effect on device performance. One approach involves a hydrogen silsesquioxane (HSQ) electron beam lithography resist serving as a dry etch mask and another with an added chromium (Cr) hard mask. We find that the performance of these devices is sensitive to the fabrication quality and is hampered by deviations in the device dimensions from those intended. Moreover, we elaborate on dry etch requirements in conjunction with the optimization of etching window geometry for a quick membrane release by selectively wet etching the substrate. We investigate etch windows that have either rectangular or trapezoidal openings which offer different etch overlaps among crystal planes of the InP substrate. An etch window that has the maximum etch overlap results in the quickest membrane release given the same dry etch depth.

5.2 Device Fabrication

In this work, BIC membrane lasers are fabricated using standard nanofabrication techniques. We choose the active medium to be epitaxially grown multiple quantum wells of InGaAsP material lattice-matched to InP substrate and tailored to emit in the telecommunication band (1.5-1.6 μm). The gain material consists of nine $\text{In}_{x=0.564}\text{Ga}_{1-x}\text{As}_{y=0.933}\text{P}_{1-y}$ quantum well layers of 10 nm thickness (bandgap of 1.6 μm) and $\text{In}_{x=0.737}\text{Ga}_{1-x}\text{As}_{y=0.569}\text{P}_{1-y}$ barrier layers of 20 nm thickness (bandgap of 1.3 μm). An additional top barrier layer of 30 nm makes the total height of the gain 300 nm (Figure 5.1a). All finished samples are composed of a system of periodic cylindrical resonators interconnected by bridges for mechanical stability (Figure 5.1b-c). The patterns including the interconnecting bridges are defined by dry etching with the help of a hard etch mask. In what follows, we employ two fabrication approaches each with different etch masks to realize these structures. One (Method I) involves a HSQ electron beam lithography resist and another (Method II) with an added Cr hard mask. The etch resistance of the two masks differ drastically and thus directly affect the final dimensions of the patterns.

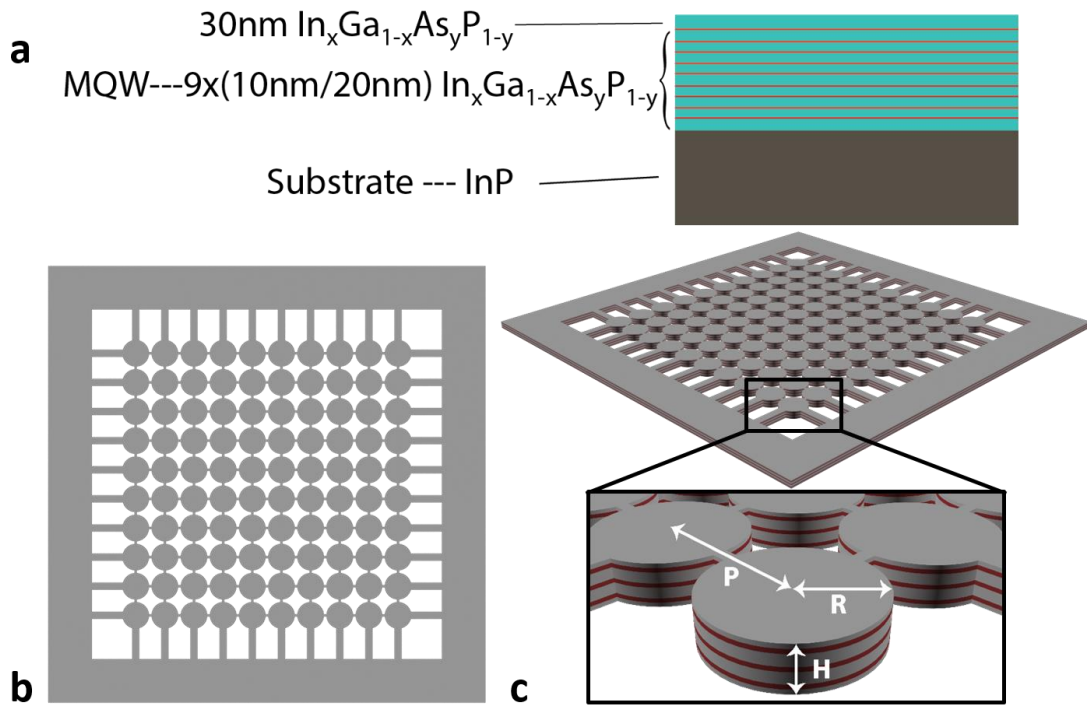


Figure 5.1: (a) Schematic of epitaxially grown InGaAsP layers on InP substrate with nine quantum wells (in red). (b) Top view of laser membrane with cylindrical resonators arranged in a square lattice interconnected by bridges and a secondary outer pad. (c) Tilted view of the membrane with a magnified view of the cylindrical resonators with radius (R), thickness ($H = 300 \text{ nm}$), and period ($P = 1.2 \mu\text{m}$).

A. Method I (HSQ Hard Mask)

Figure 5.2 shows the process flow for the fabrication of BIC membrane lasers using a HSQ negative tone resist acting as the hard mask for reactive-ion etching (RIE). Starting with the epitaxially grown wafer (Figure 5.2a), 6% HSQ in methyl isobutyl ketone (MIBK) is spin-coated at 2500 rpm for 60 s and soft-baked at 180 °C for 60 s to yield a film thickness of 130 nm. Subsequently, the HSQ is exposed at 100 kV and 3 nA beam current with 800 $\mu\text{C}/\text{cm}^2$ dose using a Vistec EBPG5200 electron beam lithography machine. The sample is developed using 25% tetramethylammonium hydroxide (TMAH) in water developer for 60 s (Figure 5.2b). In step c, a purely RIE process is performed at a base pressure of 30

mTorr and a temperature of 35 °C with a RF power of 150 W using a Trion RIE/ICP Dry Etcher. The etch is carried out with 10 sccm (standard cubic centimeter per minute) of methane (CH₄) flow, 40 sccm of hydrogen (H₂), and 7 sccm of argon (Ar) combination for 680 s with an estimated etch rate of 70 nm/min to yield an etch depth of 800 nm [21]. Here, the etch time is chosen such that all of the 300nm of InGaAsP would be etched in addition to a considerable thickness of InP for easy membrane release. Next, residual organic contamination and polymer buildup during RIE are removed with a microwave oxygen (O₂) plasma treatment with an O₂ flow rate of 120 sccm (150 W) for 15 min. The HSQ layer is removed with 30 s of buffered oxide etchant (BOE) with a ratio of 6:1 (H₂O:HF) (Figure 5.2d). Next, with the help of photolithography and a hydrochloric acid (HCl) based wet-etching solution, we remove a substantial amount of InP substrate below InGaAsP [22-24]. In step e, the areas to be wet-etched are opened in the negative-tone NR9-1500PY photoresist spun at 3500 rpm for 40 s to yield a thickness of 1.5 μm. After a 20 s UV exposure with the Karl Suss MA6 Mask Aligner and a reversal bake at 100 °C for 60 s, the resist is developed for 35 s with RD6 developer. Lastly, a diluted solution of hydrochloric acid (HCl:H₂O::3:1) with three parts acid to one part water by volume is used to selectively and anisotropically etch InP while minimally etching InGaAsP for a total etch time of 3 min (Figure 5.2f-g). Radii of the final cylindrical resonators are smaller than the radii defined after e-beam lithography mainly due to the eroding (i.e. narrowing) HSQ hard mask during RIE [25, 26]. Consequently, the InGaAsP sidewalls are also eroded. This reduction in dimensions is exacerbated with increased etch depth or etch time. The reduction in radii for an etch depth of 800 nm was ~70 nm. The reduction in dimensions also applies to the interconnecting bridges, and consequently, the mechanical stability of the membrane is

drastically weakened. To compensate for this reduction, the dimensions can be over defined by the e-beam lithography mask. However, for a periodic structure the maximum radii of the cylinders defined by the lithography mask is limited to half the period ($P/2$). Hence, dimensions close to $P/2$ cannot be realized with the current fabrication process with HSQ as the etch mask. Therefore, a tougher etch mask is needed to preserve the dimensions defined by e-beam lithography during the dry etching process.

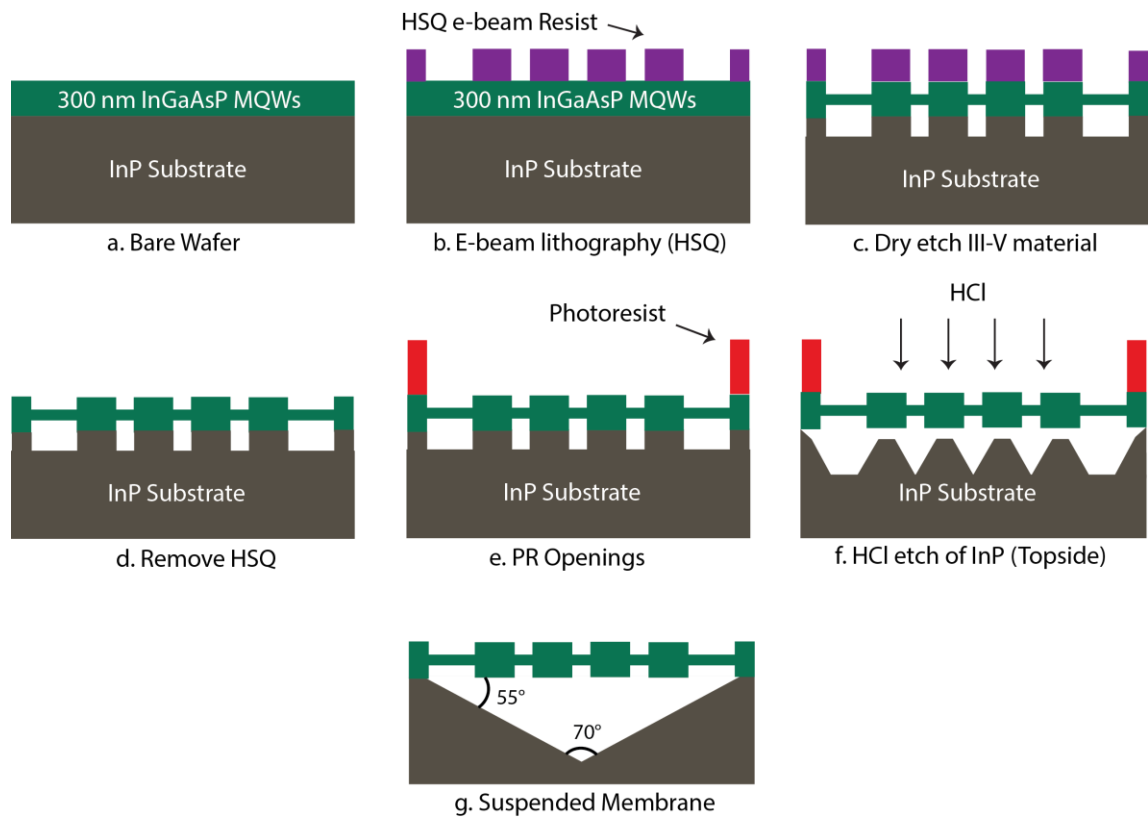


Figure 5.2: Device fabrication process without a metal hard mask starting with the epitaxially grown multiple quantum wells on InP substrate and ending with the nanocylinders suspended membrane (a-g). Note that the bridges connecting the cylinders are intentionally drawn thinner as a guide to the eye. Both the bridges and the cylinders are of the same thickness.

B. Method II (HSQ with Chrome Hard Mask)

To address the issue of reduced dimensions during the RIE step, we modify the above fabrication process to include a metal hard mask in addition to the HSQ. However, this process requires some initial preparation of the wafer (see Figure 5.3). A 100 nm of 950 PMMA A2 is spin coated at 1500 rpm for 60 s and soft-baked at 180 °C for 60 s. Subsequently, 30 nm of Cr is thermally deposited on top at a rate of 0.4 Å/s using a Denton 502 Thermal Evaporator. The Cr layer serves as a dry etch hard mask to attain and preserve the critical dimensions of the membrane. The PMMA layer serves as a sacrificial layer for the final and easy removal of the Cr (Figure 5.3b). The Cr is not directly deposited on the InGaAsP as it is extremely difficult to remove and adds significant losses to the optical device. Similar to method I, the wafer is spin-coated with 130 nm of HSQ resist. However, it is critical that the HSQ not be soft-baked at this step as the PMMA underneath will reflow and cause the Cr layer to crack extensively. Not soft-baking HSQ resist has been shown to avoid thermally induced contrast reduction [27, 28]. Hence, in comparison, not soft-baking slightly improves the contrast but does not significantly affect the cylinder definition. Next, the HSQ is exposed at 100 kV and 3 nA beam current with 800 $\mu\text{C}/\text{cm}^2$ dose and developed using 25% tetramethylammonium hydroxide (TMAH) in water developer for 60 s (Figure 5.3c). In step d, RIE processes are performed using the Oxford Plasmalab 80+ to sequentially etch the Cr and PMMA layers. First, the Cr layer is etched with a base pressure of 90 mTorr and a temperature of 15 °C with a RF power of 30 W. The etch is carried out with a combination of 3 sccm of O₂ flow and 50 sccm of chlorine (Cl₂) for 7 min with an estimated etch rate for Cr being 10 nm/min. Note that the Cr is over-etched to ensure that

all Cr residue on the surface of the PMMA is removed, as any remaining Cr will block the subsequent dry etching of the PMMA. Next, the PMMA layer is etched with a base pressure of 50 mTorr and a temperature of 20 °C with a RF power of 50 W. The etch is carried out with only 50 sccm of O₂ flow for 2 min 40 sec. It is worth noting that in addition to etching PMMA, the oxygen plasma extensively undercuts the PMMA below the Cr (black arrows in Figure 5.3d). Thus, the etch needs to be tightly controlled such that all the PMMA is removed from the InGaAsP surface and yet the undercut is minimal [29]. The PMMA undercut ultimately contributes to rough sidewalls in the patterned InGaAsP. Both the Cr and PMMA dry etch steps were thoroughly optimized. Following the Cr/PMMA etch, we dry etch the InGaAsP/InP as described in method I except with a longer etch time of 16 min for a total etch depth of 1200 nm (Figure 5.3e). This etch depth is deeper compared to method I (800 nm). Here, in contrast to method I, the higher etch resistance of the metal hard mask allows for a deeper etch into the InP substrate with minimal reduction in pattern dimensions. The deeper etch is required and is conducive for an easy membrane release discussed below. Next, the HSQ/Cr/PMMA stack is removed (Figure 5.3f). Starting with top layer, HSQ is easily removed with the help of BOE (6:1). To lift-off Cr, the sample is submerged in acetone for 2 hours with slight sonication so all the PMMA is attacked and the Cr layer is lifted off. Following the lift-off, the same wet etching recipe described in method I is used to suspend the membranes (Figure 5.2e-g). However, in comparison with the sole HSQ hard mask, we now etch for a shorter 2 min 18 sec for complete membrane suspension due to the deeper dry etch of the III-V material. Ultimately, the reduction of cylinders' radii is minimized with the use of the Cr metal mask.

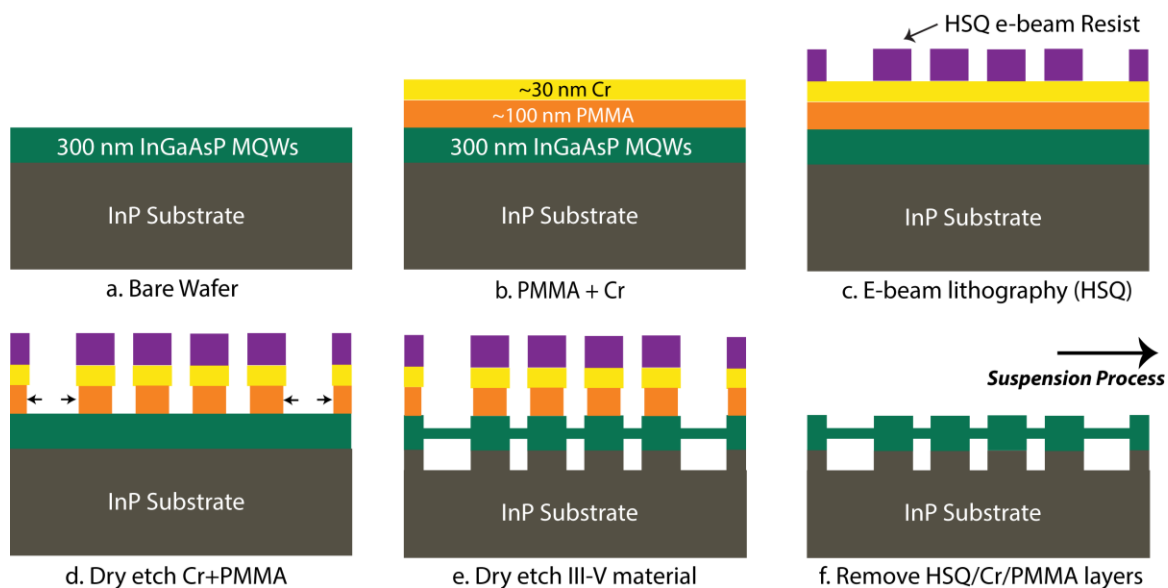


Figure 5.3: Device fabrication process involving a metal hard mask, starting with the epitaxially grown multiple quantum wells on InP substrate (a-f). The subsequent membrane release process is the same for both processes: with and without a metal hard mask (Fig. 5e-g). Note that the bridges connecting the cylinders are intentionally drawn thinner as a guide to the eye. Both the bridges and the cylinders are of the same thickness.

5.3 Results and Discussion

Figure 5.4 is a direct comparison of the dry etch quality of InGaAsP/InP with a HSQ hard mask (Method I) and an added Cr hard mask (Method II). A control pattern was etched for both cases while aiming for similar etch depths. With HSQ serving as the hard mask and its narrowing during the dry etch, the InGaAsP sidewalls have eroded inward directly resulting in the reduction of lateral dimensions as seen in Figure 5.4a and in Figure 5.4b with the HSQ removed. However, with the added Cr layer, the patterns etched in InGaAsP experience minimal reduction in the lateral dimensions as seen in Figure 5.4c and in Figure 5.4d with the mask removed. This comparison is further apparent from the analysis of bridge reduction of the finished devices shown in Figure 5.5. In Figure 5.4c, the undercut in PMMA due to the oxygen plasma is clearly visible underneath the Cr layer.

After the initial etch over the PMMA thickness, the undercut rate was estimated to be 20 nm/min [29]. A PMMA layer that is not undercut below Cr during its etch has rough edges and consequently this roughness is transferred to the InGaAsP layer thereby degrading the devices. On the other hand, a PMMA layer that is heavily undercut will once again lead to a reduction in lateral dimension, i.e. cylinder radius and bridge width. The dimension of the radius directly affects the cavity mode of the laser and the widths of the bridges affect the mechanical stability of the eventually suspended membrane.

We show in Figure 5.5 the reduction in bridge widths from their nominal or defined values as a function of the nominal radius of the cylinders for Method I (HSQ mask) and Method II (added Cr mask). The two processes have different original bridge widths, as seen in Table 5.1, since the bridges are expected to shrink dramatically for the HSQ process compared to the Cr. Hence, it is more appropriate to look at the ‘width reduction’ of the bridges from the original. With a HSQ mask, the bridge reduction is worse than with an added Cr mask. As seen in the image insets of Figure 5.5, HSQ mask yields visibly thinner bridges. However, in both cases, the bridge reduction is greatest when the cylinder radii are small and lowest when the radii are large. With small radii cylinders and for a fixed periodicity, there is more access to the sides of the bridges for the dry etch gases. This contributes to an increased sidewall erosion and thus thinner bridges. Overall, the Cr mask and its increased etch resistance help alleviate the erosion in the membrane’s most critical elements: the bridges. The etch selectivity of HSQ is ~7-8 and in comparison, the selectivity for Cr is greater than ~50.

Table 5.1: Original dimensions of bridge widths and radii defined for HSQ and Cr processes

	HSQ (W)	Cr (W)
R555 to 580 nm	240 nm	200 nm
R585 to 600 nm	180 nm	200 nm

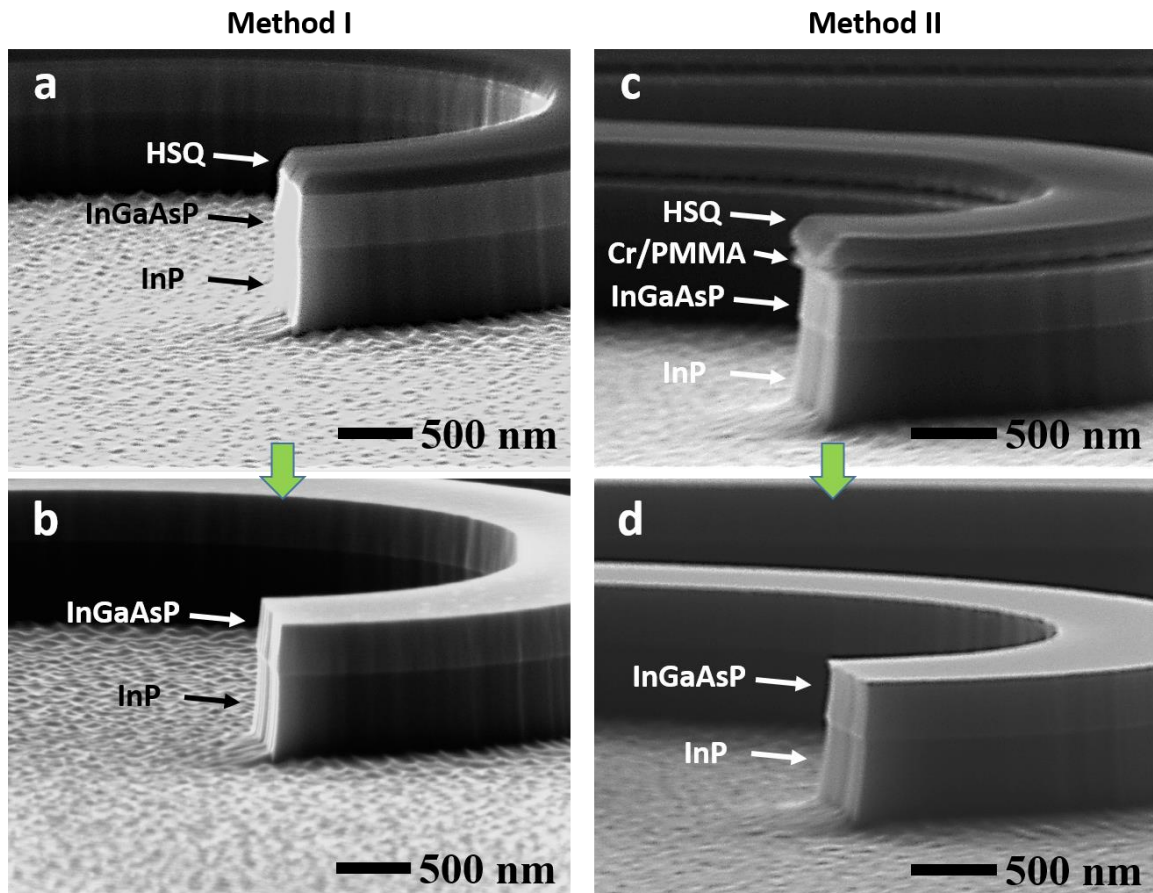


Figure 5.4: Electron micrograph images of Reactive Ion Etching (RIE) of InGaAsP/InP test patterns. Method I: Side view after dry etch with HSQ as etch mask (a) and after HSQ removal (b). Method II: Side view after dry etch with an added Cr hard mask (c) and after mask removal (d). Both were dry etched to a depth of 950 nm. The sidewall erosion is visible with a HSQ hard mask (a) compared to an added Cr hard mask (b). An undercut in the PMMA layer below the Cr is also observed.

For method I, it is worth noting that the etching resistance of HSQ could not be improved significantly with an oxygen plasma post-treatment as previously suggested [30].

This is mainly due to the drastic variation in system conditions and in the gases used for the dry etch. As for method II, to alleviate the need for a PMMA spacer, selective wet etching of the Cr layer directly deposited on InGaAsP were explored including CR-7 (perchloric acid based) and CR-1020 (nitric acid based) etchants, however all etchants significantly attack and damage InGaAsP [31].

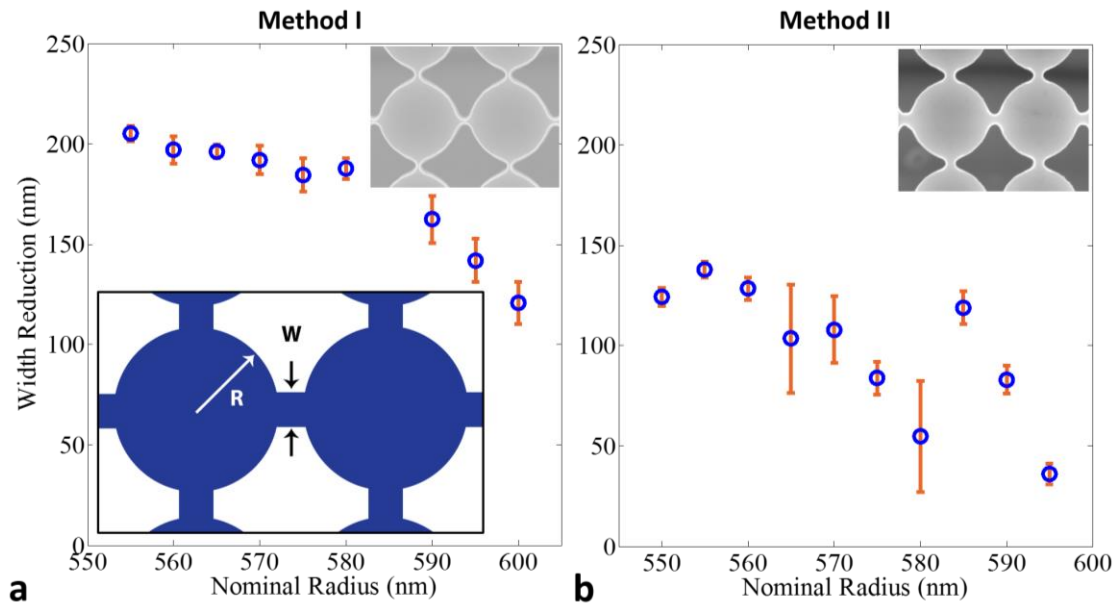


Figure 5.5: Reduction in bridge widths, W , from the nominal bridge widths as a function of the nominal radius for (a) Method I: HSQ mask and (b) Method II: added Cr mask. Left inset is a schematic of cylindrical resonators of radius, R , with interconnected bridges with widths, W . Right insets are images of the finished devices. The vertical error bars are the standard error in the measurement of the bridge widths. With a HSQ mask, the bridge reduction is worse than with an added Cr mask. However, in both cases, the bridge reduction is greatest (lowest) when the cylinder radius is small (large). With small radii cylinders and for a fixed periodicity, there is more access to the sides of the bridges for the dry etch gases. This contributes to an increased sidewall erosion and thus thinner bridges.

Following the dry etch of InGaAsP/InP material, the InGaAsP patterns are suspended by selectively removing the InP underneath with the help of HCl solution. The successful suspension of the InGaAsP patterns is contingent on the dry etch depth into InP and the geometry of the surrounding etching window as seen from Figure 5.6. There is a

strong crystallographic dependence on the etch rates of InP with HCl solution [22]. As seen in Figure 5.6a, the etch is halted by the indium (In)-rich {111} planes sloped at 55° from the plane of InGaAsP forming etch pits [23]. If the InP dry etch depth is shallow, adjoining {111} planes of neighboring openings do not meet, and the suspension process is completely halted by the etch pits. Therefore, the total dry-etch depth (h) required for adjoining {111} planes to meet and fully suspend the InGaAsP membrane of thickness (t) is: $h \geq R \tan(55^\circ) + t$ where R is the radius of the cylinders. Hence, it is imperative that the dry etch of InP be sufficiently deep in addition to the use of an appropriate etch window. As seen in Figure 5.6b and listed in Table 5.2, we employ three different etching windows for the square patterns: i. Rectangular with opening widths ($2P$) and supporting arms ($2.5P$), ii. Trapezoidal with thick supporting arms ($3P$) and opening widths ($4P$), iii. Trapezoidal with thinner supporting arms (P) and opening widths ($4P$) where $P = 1.2 \mu\text{m}$ [32]. All three etch windows lead to suspended structures given the appropriate dry etch depth is reached. The less efficient the geometry of the etch window, the more the dry etch depth required. In our case, the rectangular etch window is the least efficient. It is worth highlighting that a longer etch depth leads to a reduction in lateral dimensions even with a Cr metal mask. Therefore, it is prudent to optimize the geometry of the wet etch window for a quick membrane release. For a given geometry of the etch window such as the rectangular one, we see both a suspended array which subsequently collapsed (Figure 5.6c. i) and an etch-halted array (Figure 5.6c. ii). The two samples were processed together where both are dry-etched for an etch depth of 600 nm and subsequently wet-etched for 1 min 30 sec in HCl:H₂O (3:1) solution. The only difference being the cylindrical resonators in one array have smaller radii than the other. The array in Figure 5.6c. i with a measured

radius of 440 nm, allows for larger dry-etched openings in-between the cylinders compared to the array in Figure 5.6c. ii with a larger radius of 540 nm. The larger openings make it easier for the neighboring $\{111\}$ -InP planes to meet for a given dry etch depth. Hence, the smaller radii membrane is easily released whereas the other is halted by the formation of etch pits. It is worth noting that only a HSQ hard mask was used for these two samples. Therefore, the released membrane collapsed due to the reduction of the supporting bridge widths past their breaking point during the dry etch process. Similarly, wet etch of an array with a trapezoidal geometry is halted by the formation of etch pits due to thick supporting arms as seen in Figure 5.6d. Even prolonging the wet etch to 4 min did not break the etch pits. However, a trapezoidal etch window with thin supporting arms allows for a quick (2 min 18 sec) membrane release leaving a visibly large V-groove that runs underneath as seen in Figure 5.6e. Larger arrays were also fabricated and, as expected, required longer wet-etching times for complete suspension.

Table 5.2: Summary of wet etch windows and their dimensions for membrane release

Etch Window	Opening Widths (white)	Supporting Arms (blue)
Rectangular	2P (2.4 μm)	2.5P (3.0 μm)
Trapezoidal I	4P (4.8 μm)	3P (3.6 μm)
Trapezoidal II	4P (4.8 μm)	P (1.2 μm)

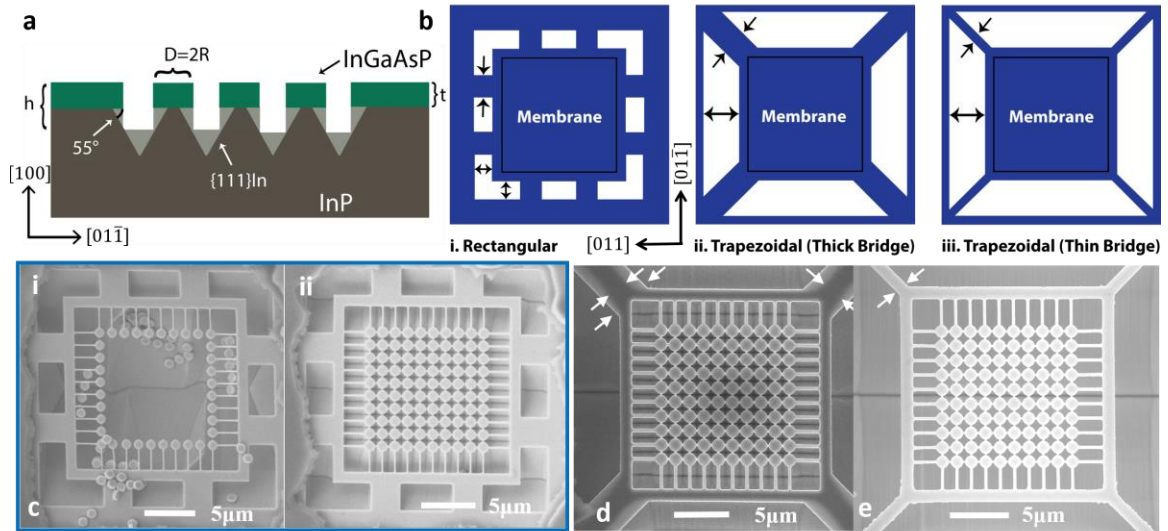


Figure 5.6: Etch requirements and optimization of membrane release. (a) Dependence of InP dry-etch depth on the crystallographic selective wet-etching of InP. The etch is halted by the slowest set of etch planes, indium (In)-rich $\{111\}$ planes of InP sloped at 55° . Therefore, the total dry-etch depth (h) required for adjoining $\{111\}$ planes to meet and fully suspend the InGaAsP membrane of thickness (t) is: $h \geq R \tan(55^\circ) + t$ (b) Three different wet-etch windows for membrane release: i. rectangular windows with opening widths ($2P$) in white and supporting arms ($2.5P$) in blue, both indicated by black arrows, ii. trapezoidal windows with thick supporting arms ($3P$) and trapezoidal opening widths ($4P$), iii. trapezoidal windows with thin supporting arms (P) and opening widths ($4P$) with $P = 1.2 \mu\text{m}$. (c-f) Electron micrograph images of completed fabrication for different etch windows and etch conditions. (c) Two 10×10 arrays with rectangular etching windows where both are dry-etched for an etch depth of 600 nm and subsequently wet-etched for 1 min 30 sec in HCl:H₂O (3:1) solution. (i.) Collapsed array with measured cylindrical radii of 440 nm after wet etching and (ii.) equivalent array with larger measured radii of 540 nm with halted etch due to formation of etch pits along $\{111\}$ plane of InP. (d) Array with trapezoidal etch window with a halted etch due to thick supporting arms of InGaAsP indicated by outer white arrows and halted InP etch underneath indicated by second pair of white arrows. There are visible etch pits between the cylindrical resonators. All the etch pits remain even after a prolonged wet-etch of 4 min. (e) Successfully suspended array with trapezoidal etch window due to the thinner supporting arms (white arrows) which was wet-etched for a total of 2 min 18 sec. A visibly large V-groove runs underneath the fully released membrane along the $\{011\}$ direction.

Both method I with a HSQ mask and method II with an added Cr metal-mask yield functional devices. However, the metal mask offers a tighter control over the finest dimensions of the pattern, i.e. radius and bridge widths (see Figure 5.7). A completed 10×10 array with HSQ as the hard mask can be seen in Figure 5.7a and a magnified view

in Figure 5.7b. Similarly, a 10x10 array with Cr hard mask can be seen in Figure 5.7c and a magnified view in Figure 5.7d. As seen, the cylinders fabricated with the Cr hard mask maintain the mask dimensions with straighter sidewalls whereas with the HSQ mask both the cylinders and bridges shrink drastically with sloped sidewalls. There is also some noticeable sidewall roughness when using a Cr/PMMA hard mask mainly due to the etch quality of the PMMA.

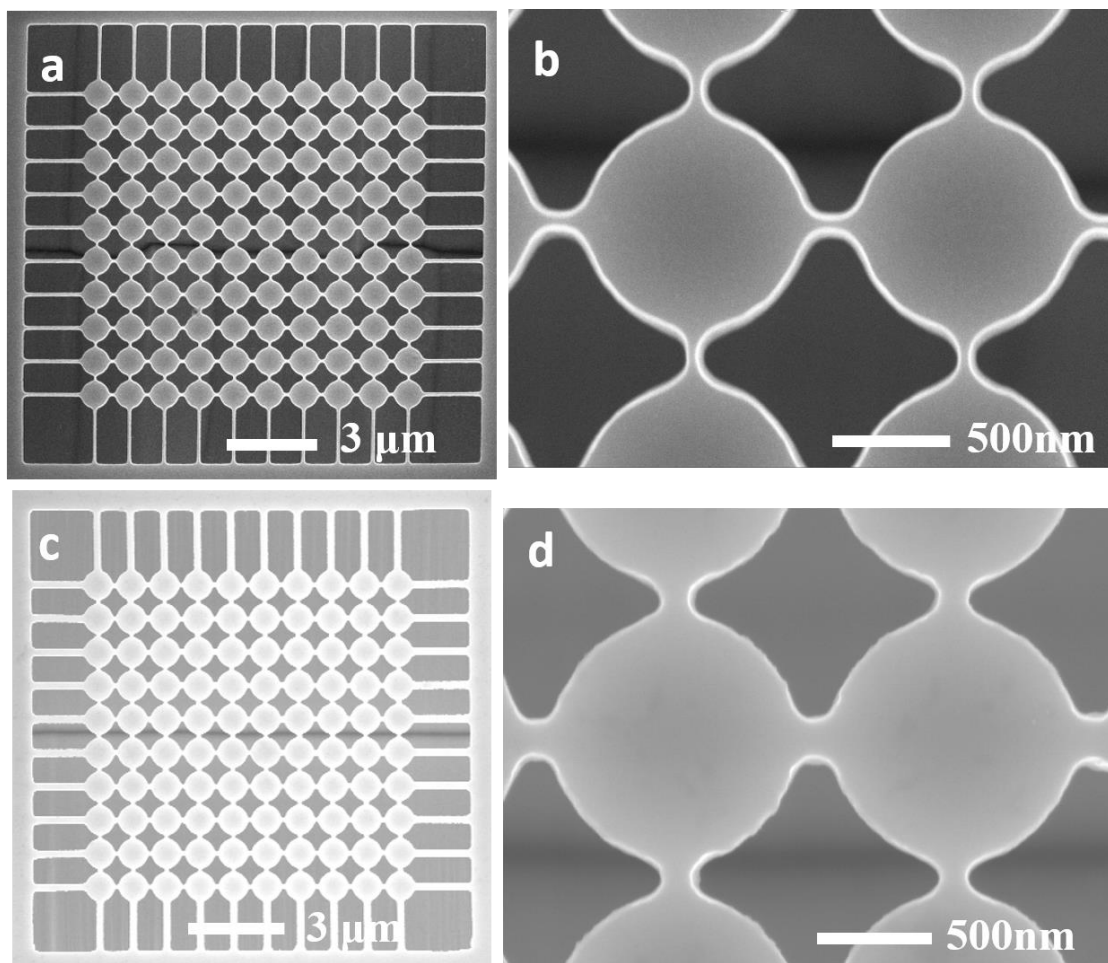


Figure 5.7: Electron micrograph images of completed membrane structures with 10x10 cylindrical resonators interconnected by a network of bridges with a visible etch pit below in the InP substrate for HSQ etch mask (a) and added Cr hard mask (c). Respective zoom-in images of two cylinders at the center of the array (b, d). As seen, the cylinders fabricated with the Cr hard mask maintain the mask dimensions with straighter sidewalls whereas with the HSQ mask both the cylinders and bridges shrink drastically with sloped sidewalls.

5.4 Device Performance

In Figure 5.8, we observe lasing from devices made using a HSQ hard mask and a Cr hard mask. In Figure 5.8a, we observe lasing from a fully suspended 10x10 array fabricated with a HSQ hard mask emitting at 1567 nm with a threshold power of 67 μW . Similarly, we also observe lasing from a 10x10 array fabricated with the help of a Cr hard mask but emitting at 1540 nm with a threshold power of 89 μW (Figure 5.8b). Both arrays are optically pumped by a 1064 nm laser with 12 ns pulse width at a repetition rate of 300 kHz (Figure 5.8c).

By design and in virtue of the limitation of the two fabrication methods, the dimensions within the laser array (radius and bridge widths) are different which influences the lasing mode and thus dictates the lasing wavelength and threshold power. Hence, the two lasers emit at different wavelengths and have different thresholds. It is also worth noting that different etch windows were used for the two devices shown here. A rectangular etch window was used for the HSQ hard mask and a trapezoidal window with thin supporting arms for the Cr hard mask. The etch window has no effect on laser results but rather a considerable effect on the release of the lasing membranes during fabrication. The lasing mode is strictly dictated by the dimensions of the cylinders and bridges in the array. An optimized etch window such as the trapezoidal maximizes the etch overlap among crystal planes resulting in a quicker membrane release time for a given dry etch depth [32]. This also allows for a shorter dry etch time (or etch depth) thereby preserving dimensionality of the cylinders and bridges.

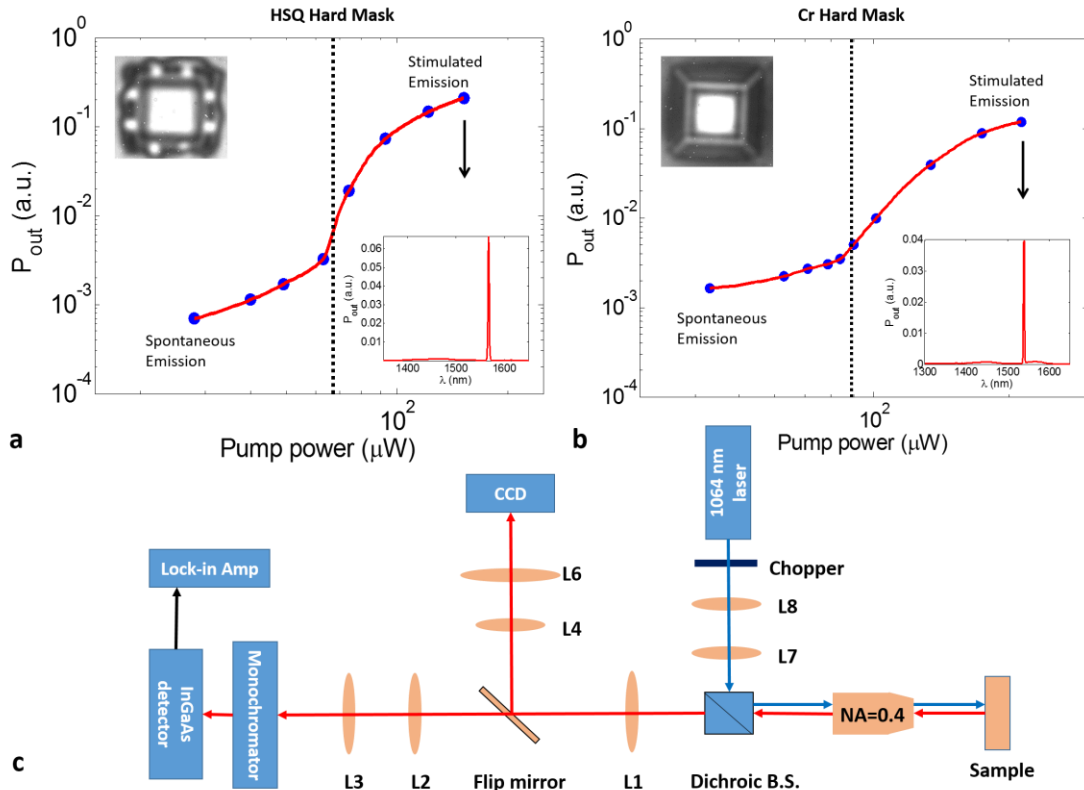


Figure 5.8: Lasing from fully suspended devices fabricated using a HSQ hard mask (a) and a Cr hard mask (b). Both devices are 10×10 arrays optically pumped at 1064 nm and operating at room temperature as seen by IR camera during testing (left insets). (a) Light-Light (LL) curve of the laser fabricated using a HSQ hard mask emitting at 1567 nm (right inset) with a threshold of $67 \mu\text{W}$ (vertical dotted line). (b) LL curve for a laser fabricated using a Cr hard mask emitting at 1540 nm (right inset) with a threshold of $89 \mu\text{W}$. (c) Schematic of photoluminescence setup for the characterization of membrane lasers with a pulsed pump (1064 nm) path in blue and emission/imaging path in red with a CCD camera, a monochromator, and an InGaAs detector tied to a lock-in amplifier. A microscope objective (NA=0.4) and L1 to L8 correspond to the lens assembly to the sample.

5.5 Concluding Remarks

In this chapter, we have described two different approaches of fabricating suspended membrane lasers composed of periodic cylindrical nanoresonators on an InGaAsP/InP platform. One approach involves HSQ as a dry etch hard mask and the other uses a Cr metal hard mask. The HSQ mask leads to significant reduction in dimensions

during the dry etching process. We observe that this reduction affects the mechanical stability of the membrane by eroding the bridges that keep the cylindrical resonators suspended. It also affects the cylinders' radii which are critical to the lasing mode. We have shown that using a metal hard mask significantly minimizes the lateral reduction in the dimensions of the pattern in comparison to the HSQ hard mask. A metal mask allows for a precise fabrication of patterns defined by e-beam lithography. Moreover, we have discussed dry etch requirements to avoid etch pit formation in InP and the importance of an optimized wet etching window. A trapezoidal etching window with thin supporting arms was found to be the optimal window for a quick membrane release. We have shown that device functionality was unimpaired by either fabrication method. However, in the case of the metal hard mask, device performance such as a reduction in threshold power can be further improved with the reduction in sidewall roughness. Hence, a better alternative to PMMA spacer is needed: one that can be anisotropically etched straight with smooth sidewalls. The techniques outlined here will be of practical interest in the design and construction of novel membrane based devices with applications ranging from microfluidic biosensors to lasers on flexible substrates.

Chapter 5, in part, is a reprint of the material as it appears in A. Kodigala, Q. Gu, T. Lepetit, B. Bahari, and B. Kanté, "Mechanically stable conjugate and suspended lasing membranes of bridged nano-cylinders," *Optical Materials Express* **7**, 2980 (2017). The dissertation author was the primary researcher and author of this paper.

References

1. D. V. Dao, K. Nakamura, T. T. Bui, and S. Sugiyama, "Micro/nano-mechanical sensors and actuators based on SOI-MEMs technology," *Adv. Nat. Sci.: Nanosci. Nanotechnol.* **1**, 013001 (2010).
2. T. J. Kippenberg and K. J. Vahala, "Cavity optomechanics: Back-action at the mesoscale," *Science* **321**, 5893 (2008).
3. J. D. Thompson, B. M. Zwickl, A. M. Jayich, F. Marquardt, S. M. Girvin, J. G. E. Harris, "Strong dispersive coupling of high-finesse cavity to a micromechanical membrane," *Nature* **452**, 71 (2008).
4. I. Favero and K. Karrai, "Optomechanics of deformable optical cavities," *Nature Photonics* **3**, 201 (2009).
5. O. Painter, R. K. Lee, A. Scherer, A. Yariv, J. D. O'Brien, P. D. Dapkus, I. Kim, "Two-dimensional photonic band-gap defect mode laser," *Science* **284**, 5421 (1999).
6. H. Kahle, C. M. N. Mateo, U. Brauch, P. Tatar-Mathes, R. Bek, M. Jetter, T. Graf, and P. Michler, "Semiconductor membrane external-cavity surface-emitting laser (MECSEL)," *Optica* **3**, 1506 (2016).
7. D. G. Johnson, T. S. Khire, Y. L. Lyubarsakaya, K. J. P. Smith, J-P. S. DesOrmeaux, J. G. Taylor, T. R. Gaborski, A. A. Shestopalov, C. C. Striemer, and J. L. McGrath, "Ultrathin Silicon Membranes for Wearable Dialysis," *Adv. Chronic Kidney Dis.* **20**, 508 (2013).
8. A. Shchepetove, M. Prunnila, F. Alzine, L. Schneider, J. Cuffe, H. Jiang, E. I. Kauppinen, C. M. Sotomayor Torres, and J. Ahopelto, "Ultra-thin free-standing single crystalline silicon membranes with strain control," *Appl. Phys. Lett.* **102**, 192108 (2013).
9. I. Vlassioux, P. Y. Apel, S. N. Dmitriev, K. Healy, and Z. S. Siwy, "Versatile ultrathin nanoporous silicon nitride membranes," *Proc. Natl. Acad. Sci.* **106**, 21039 (2009).
10. S. Chakram, Y. S. Patil, L. Chang, and M. Vengalattore, "Dissipation of ultrahigh quality factor SiN membrane resonators," *Phys. Rev. Lett.* **112**, 127201 (2014).
11. A. Tserepi, C. Tsamis, G. Kokkoris, E. Gogolides, and A. G. Nassiopoulou, "Fabrication of suspended thermally insulating membranes using frontside micromachining of the Si substrate: characterization of the etching process," *J. Micromech. Microeng.* **13**, 323 (2003).
12. L. A. Coldren, S. W. Corzine, and M. L. Mashanovitch, *Diode Lasers and Photonic Integrated Circuits*, 2nd Ed, Hoboken (N.J.), Wiley, Chapter 1 (2012).

13. Y. Akahane, T. Asano, B-S. Song, and S. Noda, "High-Q photonic nanocavity in a two-dimensional photonic crystal," *Nature* **425**, 944 (2003).
14. J. D. Joannopoulos, S. G. Johnson, J. N. Winn, and R. D. Meade, *Photonic Crystals – Molding the Flow of Light*, 2nd Edition, Princeton (N.J.), Princeton University Press, 2008.
15. J. von Neumann and E. Wigner, "On some peculiar discrete eigenvalues," *Phys. Z.* **30**, 467 (1929).
16. D. C. Marinica, S. V. Shabanov, and A. G. Borisov, "Bound states in the continuum in photonics," *Phys. Rev. Lett.* **100**, 183902 (2008).
17. C. W. Hsu, B. Zhen, J. Lee, S-L. Chua, S. G. Johnson, J. D. Joannopoulos, and M. Soljagic, "Observation of trapped light within the radiation continuum," *Nature* **499**, 188 (2013).
18. T. Lepetit and B. Kanté, "Controlling multipolar radiation with symmetries for electromagnetic bound states in the continuum," *Phys. Rev. B* **90**, 241103(R) (2014).
19. A. Kodigala, T. Lepetit, Q. Gu, B. Bahari, Y. Fainman, and B. Kanté, "Lasing action from photonic bound states in continuum," *Nature* **541**, 196-199 (2017).
20. C. W. Hsu, B. Zhen, A. D. Stone, J. D. Joannopoulos, and M. Soljagic, "Bound states in the continuum," *Nat. Rev. Mater.* **1**, 16048 (2016).
21. C. Youtsey and I. Adesida, *Dry Etching of InP and Related Materials*, in *Handbook of Advanced Plasma Processing Techniques* (Springer, Berlin, 2000), pp. 479-483.
22. S. Adachi and H. Kawaguchi, "Chemical etching characteristics of (001) InP," *J. Electrochem. Soc.* **128**, 1342 (1981).
23. K. Srinivasan, P. E. Barclay, and O. Painter, "Fabrication of high-quality-factor photonic crystal microcavities in InAsP/InGaAsP membranes," *J. Vac. Sci. Technol. B* **22**, 875 (2004).
24. P. Mounaix, P. Delobelle, X. Melique, L. Bornier, and D. Lippens, "Micromachining and mechanical properties of GaInAs/InP microcantilevers," *Mater. Sci. Eng., B* **51**, 258 (1998).
25. B.-T. Lee, T. R. Hayes, P. M. Thomas, R. Pawelek, and P. F. Sciortino, Jr., "SiO₂ mask erosion and sidewall composition during CH₄/H₂ reactive ion etching of InGaAsP/InP," *Appl. Phys. Lett.* **63**, 3170 (1993).
26. K. Ding and C. Z. Ning, "Fabrication challenges of electrical injection metallic cavity semiconductor nanolasers," *Semicond. Sci. Technol.* **28**, 124002 (2013).

27. F. C. M. J. M. van Delft, "Delay-time and aging effects on contrast and sensitivity of hydrogen silsesquioxane," *J. Vac. Sci. Technol. B* **20**, 2932 (2002).
28. J. K. W. Yang, B. Cord, H. Duan, K. K. Berggren, J. Klingfus, S.-W. Nam, K.-B. Kim, and M. J. Rooks, "Understanding of hydrogen silsesquioxane electron resist for sub-5-nm-half-pitch lithography," *J. Vac. Sci. Technol., B* **27**, 2622 (2009).
29. H. Yang, A. Jin, Q. Luo, J. Li, C. Gu, and Z. Cui, "Electron beam lithography of HSQ/PMMA bilayer resists for negative tone lift-off process," *Microelectronic Engineering* **85**, 814 (2008).
30. D. Lauvernier, S. Garidel, C. Legrand, J-P. Vilcot, "Realization of sub-micron patterns on GaAs using a HSQ etching mask," *Microelectronic Engineering* **77**, 210 (2005).
31. K. R. Williams, K. Gupta, and M. Wasilik, "Etch rates for micromachining processing part II" *J. Microelectromech. Syst.* **12**, 6 (2003).
32. S. Mendoza-Acevedo, M. A. Reyes-Barranca, E. N. Vazquez-Acosta, J. A. Moreno-Cadenas, and J. L. Gonzalez-Vidal, 'Micromachining techniques for fabrication of micro and nano structures,' Ch 9, InTech (2012).

Chapter 6

Summary and Outlook

In this dissertation, we have explored two special types of singularities, Exceptional Points (EPs) and Bound States in the Continuum (BICs), as they pertain to open photonic systems with applications for enhanced sensing and low-threshold lasing respectively. An intrinsically lossy plasmonic platform was quantitatively studied and designed to exhibit mode coalescence or EPs. In contrast, a semiconductor gain material was structured to support resonance trapped BIC modes which were experimentally demonstrated to lase. The first chapter of this dissertation served as an appropriate introduction to the topics of EPs and BICs while motivating the present research in their respective material platforms.

Chapter 2 of this dissertation provided the much-needed background for describing open systems, such as the plasmonic shift-bar system, which are free to interact with their environment via radiation with an effective Hamiltonian formalism derived from Coupled Mode Theory (CMT) and non-Hermitian quantum mechanics. This allowed for the quantitative estimate of resonance information (*i.e.* eigenmodes) from the scattering parameters of a plasmonic system. Using this method, resonance dynamics of coupled plasmonic bars were thoroughly investigated and as predicted. This chapter laid the foundation for the work presented in Chapter 3.

Chapter 3 presents an EP singularity in a 3D plasmonic nanostructure. The systems were composed of coupled plasmonic nanoresonators and were judiciously and systematically driven to EPs by controlling symmetry-compatible modes via their near-field and far-field interactions. Moreover, diverging residues near EPs were shown. The proposed platform opens the way to the investigation of EPs for enhanced light-matter interactions and applications in sensing.

Chapter 4 showed the experimental demonstration of the first resonance-trapped BIC lasers on an InGaAsP material platform operating at room temperature. The design, characterization and analysis of these optically pumped BIC lasers were described. These BIC lasers, made of an array of suspended cylindrical nanoresonators, carry some truly unique properties. They are fairly robust and can be scaled down in size to arrays as small as 8-by-8 unit cells. Similarly, they can also be scaled up for higher emission powers. The lasing wavelength was shown to follow the theoretical prediction of the BIC mode and the inverse relationship between quality factor and lasing threshold was also experimentally demonstrated. Moreover, operating near the BIC singularity, these lasers have very low threshold powers limited mainly by material losses. Topological properties of these BIC lasers remain to be explored.

Chapter 5 is dedicated to the fabrication of these suspended membrane BIC lasers and the challenges therein. Two different fabrication approaches were presented in an effort to optimize and finely control the dimensions of the patterns. This is crucial for laser operation near the BIC singularity. A chromium (Cr) metal hard mask during dry etching was shown to offer finer control over pattern dimensions such as the cylinder radius.

Moreover, a thorough discussion on the suspension process and the mechanical stability of these lasers was presented.

Throughout this dissertation, we have described several areas subject to future research. First, experimental realization of EPs on a plasmonic platform such as the shift-bar system is a challenging task both in terms of fabrication and the accurate characterization of loss mechanisms to reach an EP. Not just scattering amplitudes but also their phase information may be needed to observe an EP. Once achieved, its successful implementation as an enhanced sensor requires further work with system integration and the addition of specificity. Further theoretical inquiries into loss mechanisms are also needed. As per BIC lasers, the immediate focus being the realization of an electrically pumped BIC laser. As expected, there are a few challenges to surmount. Mainly, the difficulty in maintaining current uniformity across the laser array especially when scaling up in size for higher emission power. Since these structures are suspended membranes, heat dissipation during device operation is also a concern and needs to be mitigated. With these issues addressed, BIC lasers may soon see various applications including solid-state LIDAR for autonomous vehicles amongst others.

Appendix A (Ch 2)

A.1 S-parameters and eigenvalues of shift-bar (two-bar) system

This appendix consists of full scattering parameter and the eigenvalues determined for the shift-bar system described in Chapter 2. It serves as an expansion to the data provided in Figure 2.5a, b, and its inset describing the maximum inversion between the symmetric (ω_+) and anti-symmetric (ω_-) modes at a shift, dx , of half-period ($p_x/2$) as a function of p_x and h_{sub} . To begin, Figure A.1 displays the reflection, transmission, and absorption spectra as a function of shift, dx , for $p_x=600$ nm and $h_{\text{sub}}=75$ nm. For a given periodicity, the full spectra for varying oxide spacer thicknesses ($h_{\text{sub}}=50, 75, 100$ nm) are displayed in Figure A.2 ($p_x=600$ nm), Figure A.4 ($p_x=700$ nm), Figure A.6 ($p_x=800$ nm), Figure A.8 ($p_x=900$ nm), and Figure A.10 ($p_x=1000$ nm). Correspondingly, their respective complex eigenvalues with resonance frequencies and linewidths are displayed in Figure A.3 ($p_x=600$ nm), Figure A.5 ($p_x=700$ nm), Figure A.7 ($p_x=800$ nm), Figure A.9 ($p_x=900$ nm), and Figure A.11 ($p_x=1000$ nm). Here, the effect of periodicity and spacer thickness is clearly seen as described by the static dipole approximation in Chapter 2.

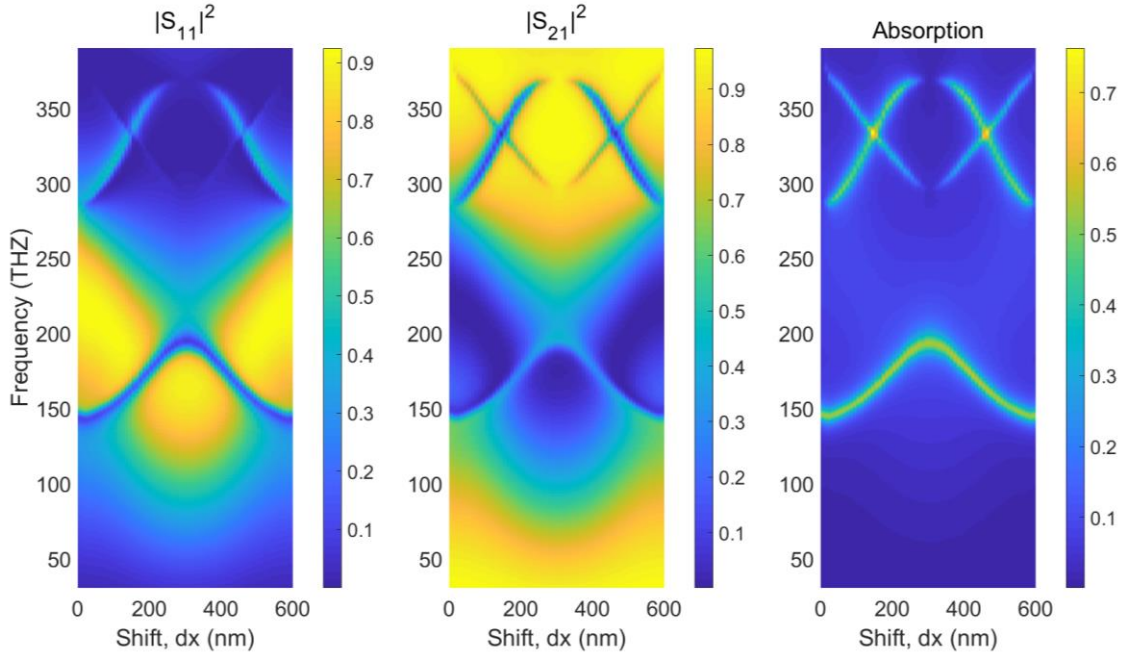


Figure A.1: (left to right) Reflection, $|S_{11}|^2$, transmission, $|S_{21}|^2$, and absorption, $1-|S_{11}|^2-|S_{21}|^2$, spectra as a function of shift, dx , for $p_x=600$ nm and $h_{sub}=75$ nm. The non-radiative anti-symmetric (ω_-) mode is clearly visible in the absorption spectra whereas the symmetric (ω_+) mode is visible in the reflection and transmission spectra as a broad or highly radiative mode.

$P_x = 600$ nm

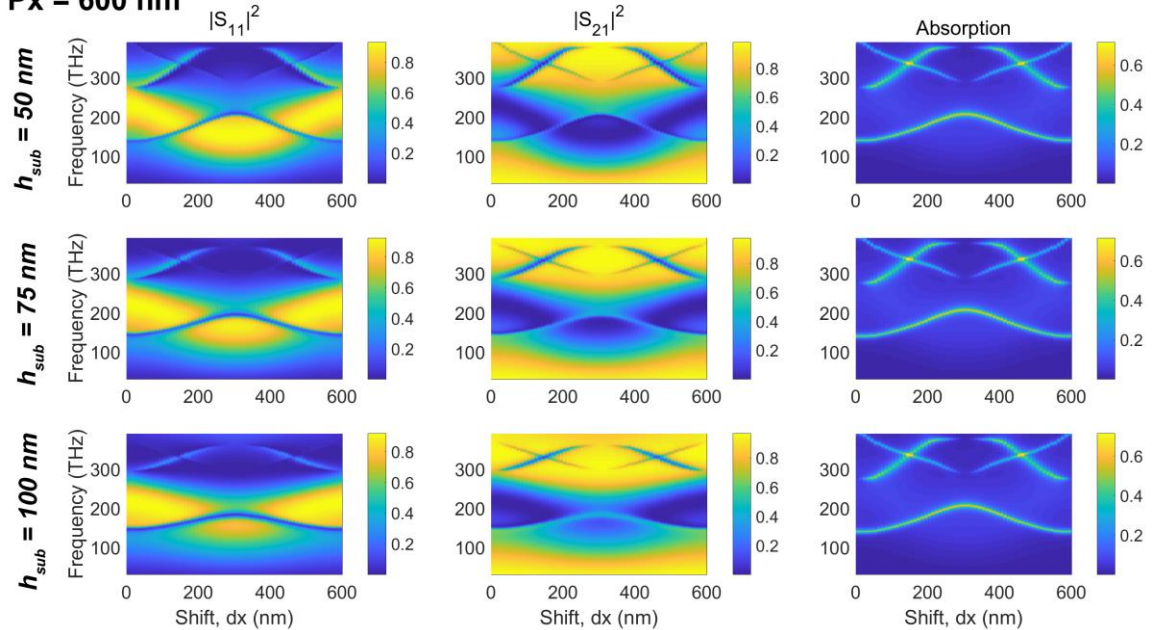


Figure A.2: (left to right) Reflection, $|S_{11}|^2$, transmission, $|S_{21}|^2$, and absorption, $1-|S_{11}|^2-|S_{21}|^2$, spectra as a function of shift, dx , for $p_x=600$ nm and $h_{sub}=50, 75, 100$ nm (top to bottom) with non-radiative anti-symmetric (ω_-) and radiative symmetric (ω_+) modes.

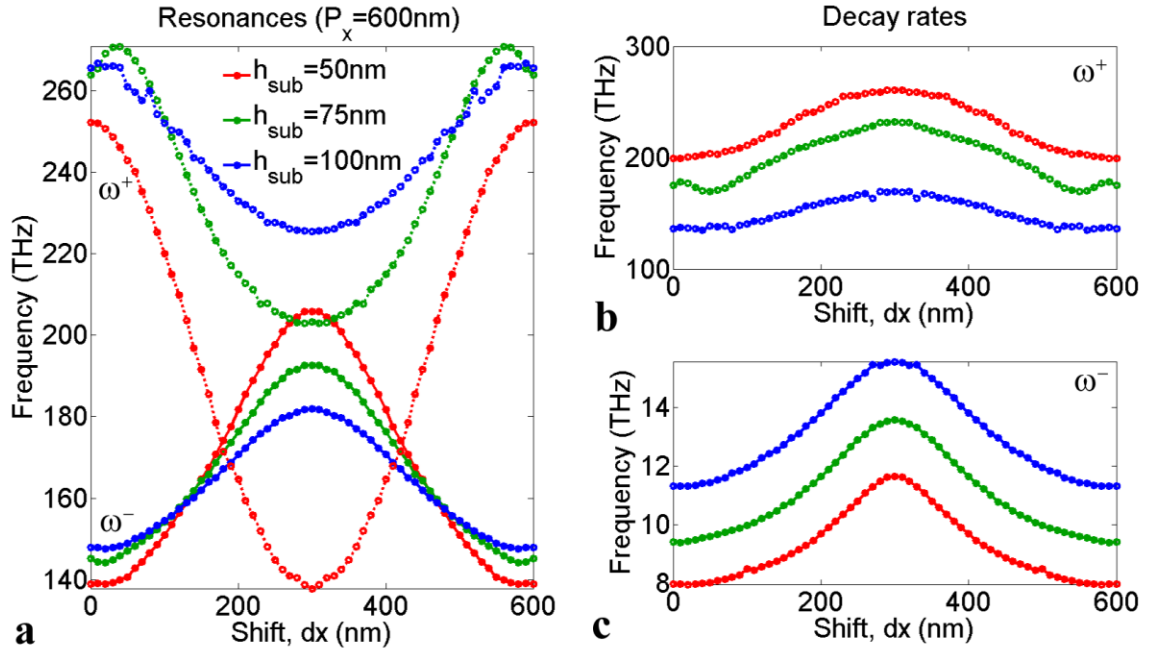


Figure A.3: (a) Evolution of resonant frequencies as a function of shift, dx , with linewidths pertaining to (b) symmetric (ω_+) and (c) anti-symmetric (ω_-) modes for $p_x = 600$ nm and $h_{sub} = 50, 75, 100$ nm.

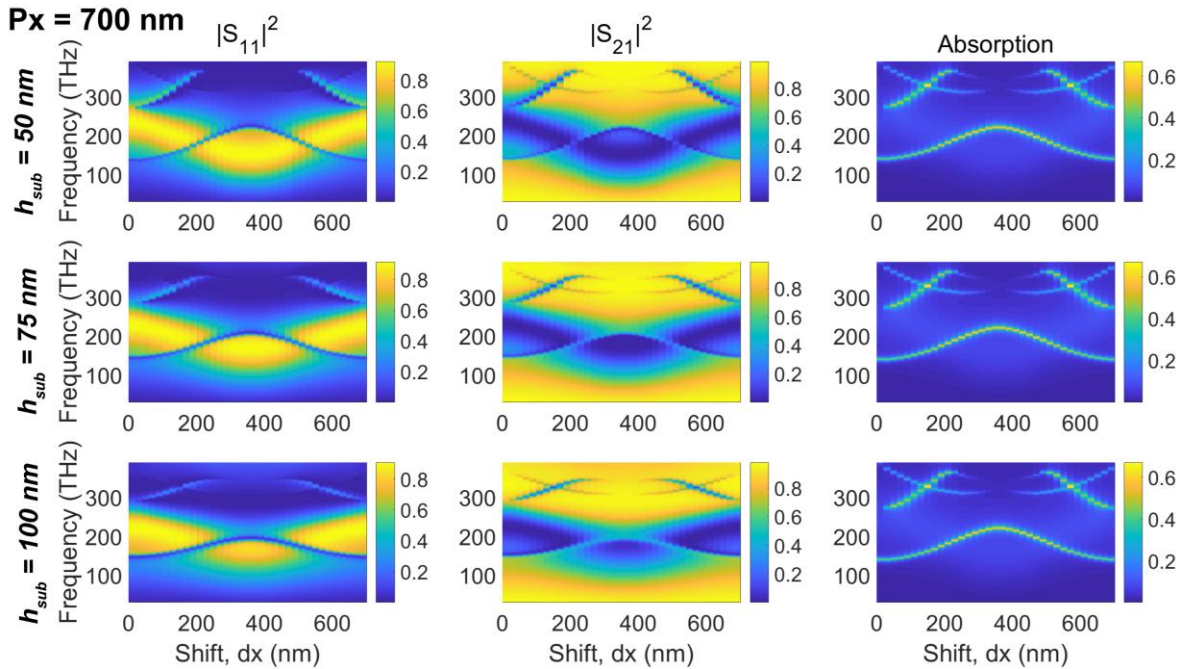


Figure A.4: (left to right) Reflection, $|S_{11}|^2$, transmission, $|S_{21}|^2$, and absorption, $1 - |S_{11}|^2 - |S_{21}|^2$, spectra as a function of shift, dx , for $p_x = 700$ nm and $h_{sub} = 50, 75, 100$ nm (top to bottom) with non-radiative anti-symmetric (ω_-) and radiative symmetric (ω_+) modes.

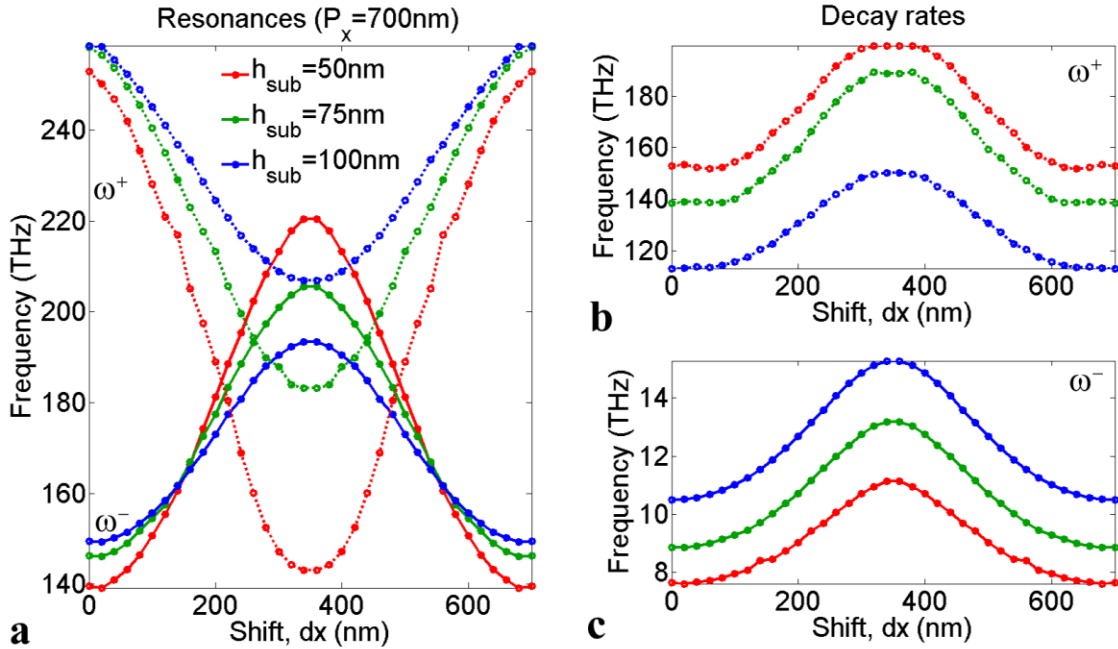


Figure A.5: (a) Evolution of resonant frequencies as a function of shift, dx , with linewidths pertaining to (b) symmetric (ω_+) and (c) anti-symmetric (ω_-) modes for $p_x=700$ nm and $h_{sub}=50, 75, 100$ nm.

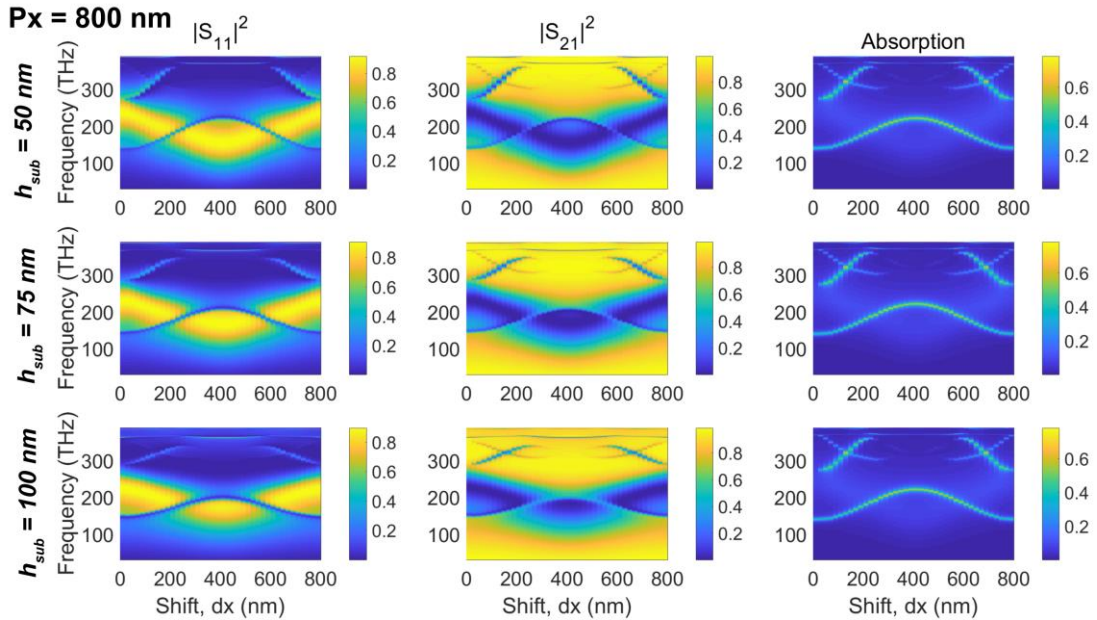


Figure A.6: (left to right) Reflection, $|S_{11}|^2$, transmission, $|S_{21}|^2$, and absorption, $1 - |S_{11}|^2 - |S_{21}|^2$, spectra as a function of shift, dx , for $p_x=800$ nm and $h_{sub}=50, 75, 100$ nm (top to bottom) with non-radiative anti-symmetric (ω_-) and radiative symmetric (ω_+) modes.

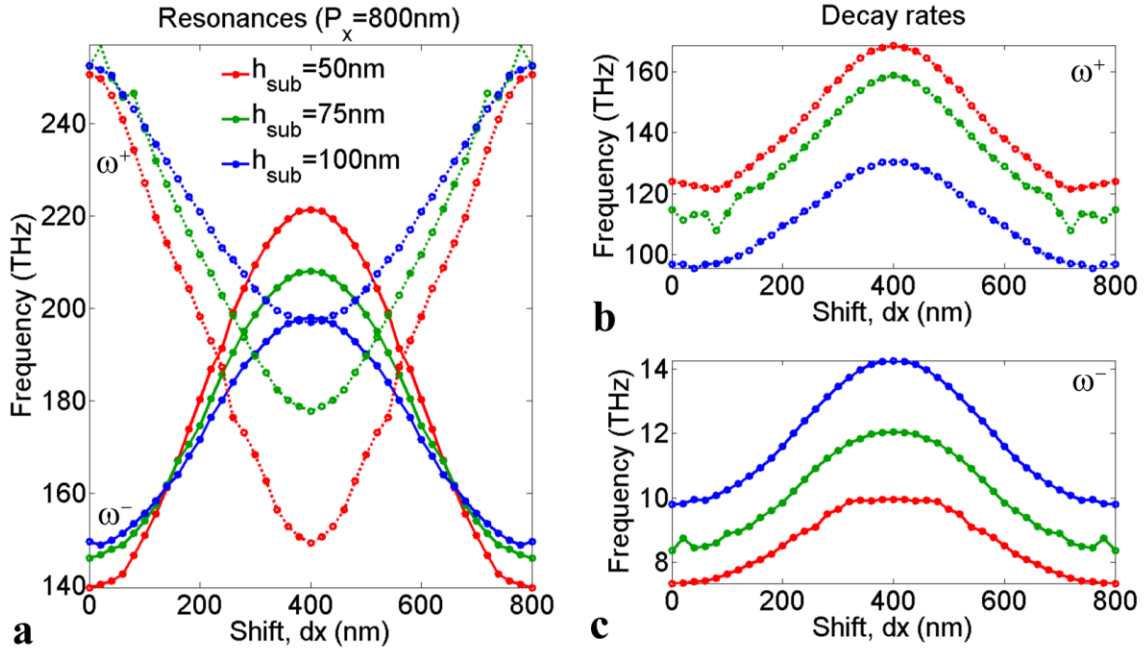


Figure A.7: (a) Evolution of resonant frequencies as a function of shift, dx, with linewidths pertaining to (b) symmetric (ω_+) and (c) anti-symmetric (ω_-) modes for $p_x=800$ nm and $h_{\text{sub}}=50, 75, 100$ nm.

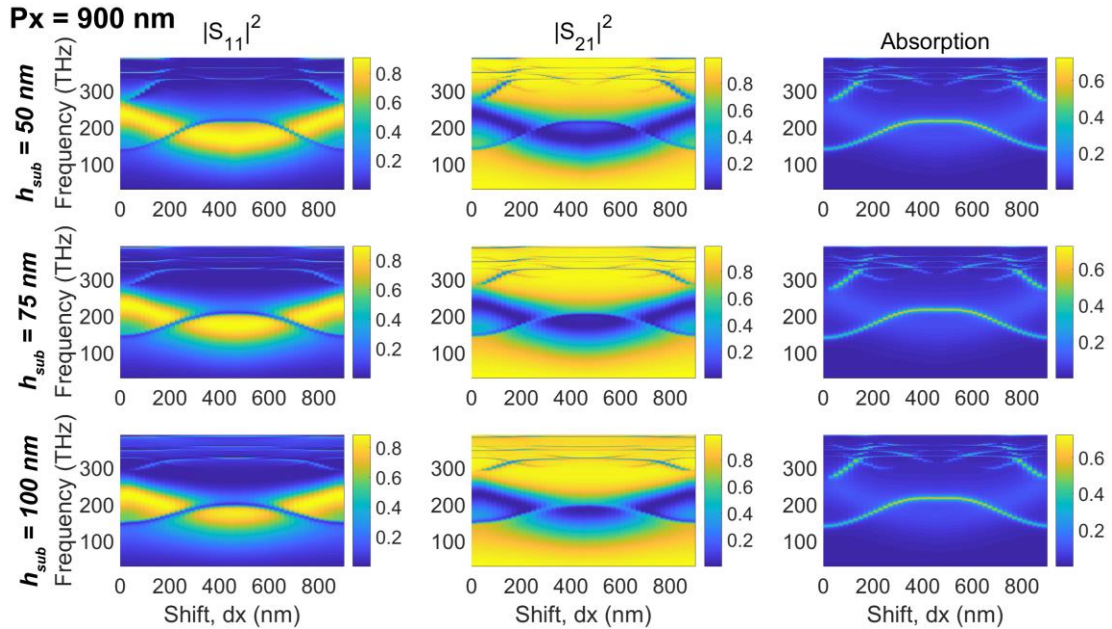


Figure A.8: (left to right) Reflection, $|S_{11}|^2$, transmission, $|S_{21}|^2$, and absorption, $1-|S_{11}|^2-|S_{21}|^2$, spectra as a function of shift, dx, for $p_x=900$ nm and $h_{\text{sub}}=50, 75, 100$ nm (top to bottom) with non-radiative anti-symmetric (ω_-) and radiative symmetric (ω_+) modes.

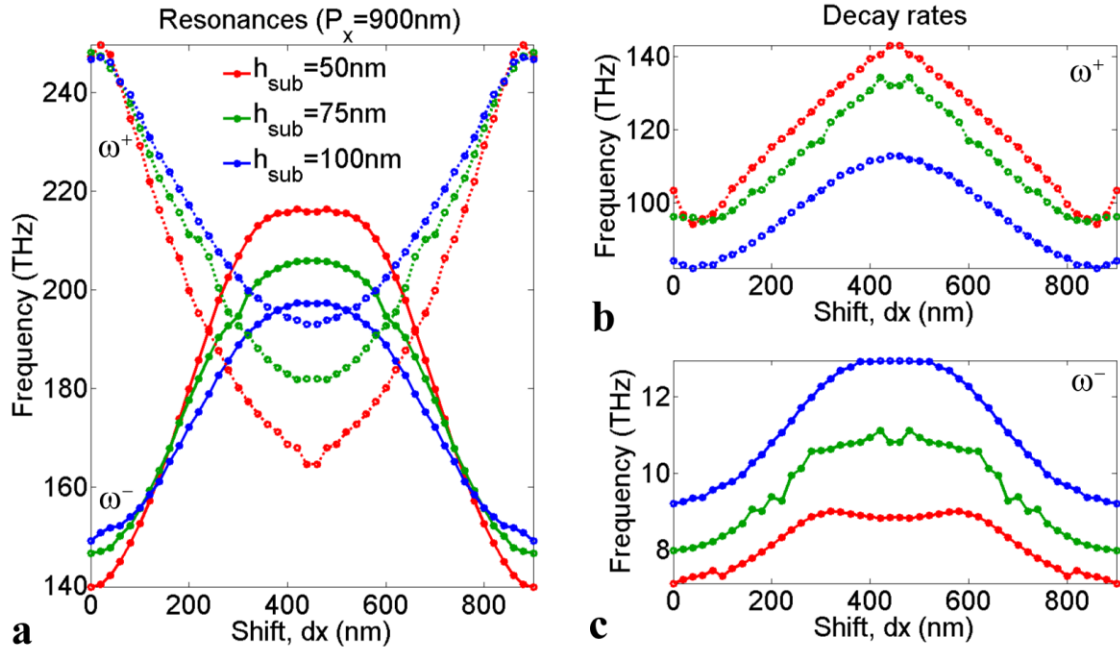


Figure A.9: (a) Evolution of resonant frequencies as a function of shift, dx, with linewidths pertaining to (b) symmetric (ω_+) and (c) anti-symmetric (ω_-) modes for $p_x=900$ nm and $h_{\text{sub}}=50, 75, 100$ nm.

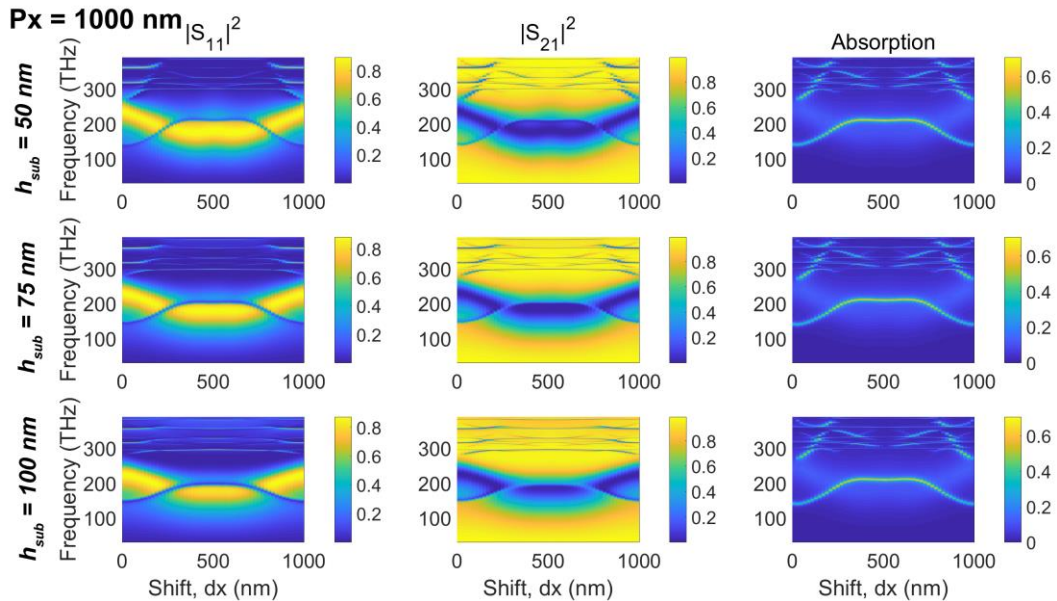


Figure A.10: (left to right) Reflection, $|S_{11}|^2$, transmission, $|S_{21}|^2$, and absorption, $1-|S_{11}|^2-|S_{21}|^2$, spectra as a function of shift, dx, for $p_x=1000$ nm and $h_{\text{sub}}=50, 75, 100$ nm (top to bottom) with non-radiative anti-symmetric (ω_-) and radiative symmetric (ω_+) modes.

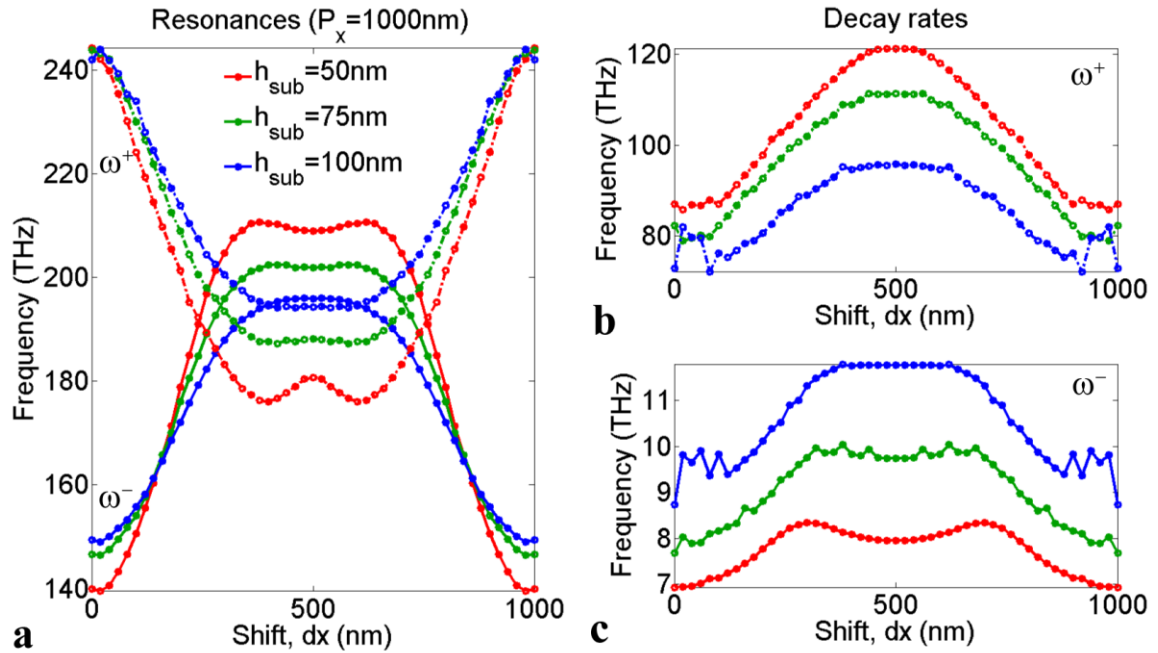


Figure A.11: (a) Evolution of resonant frequencies as a function of shift, dx , with linewidths pertaining to (b) symmetric (ω_+) and (c) anti-symmetric (ω_-) modes for $p_x=1000$ nm and $h_{sub}=50, 75, 100$ nm.

Appendix B (Ch 3)

B.1 S-parameters and eigenvalues of three and five-bar systems with EPs

The following appendix provides scattering spectra for the three and five-bar systems both of which have been shown to possess an EP in Chapter 3. For the two-bar case, we simply referred to the fundamental modes as being either symmetric (even) or anti-symmetric (odd) with respect to the bisecting plane as seen in Figure B.1a. However, for a system with more than two resonators there is more than one mode of shared symmetry. For example, the three-bar system has two fundamental symmetric (even) modes (A, C) and one fundamental anti-symmetric (odd) mode (B) as seen in Figure B.1b. Since, even and odd modes are non-interacting, the behavior of these modes can be easily observed individually with the help of symmetry planes: perfect electric conductor (PEC) for odd modes and perfect magnetic conductor (PMC) for even modes. To begin, Figure B.2 below displays the 1-port reflection spectra as a function of shift, dx , for $p_x=800$ nm and $dz=60$ nm which is close to an EP as can be seen in Figure 3.2 of Chapter 3.

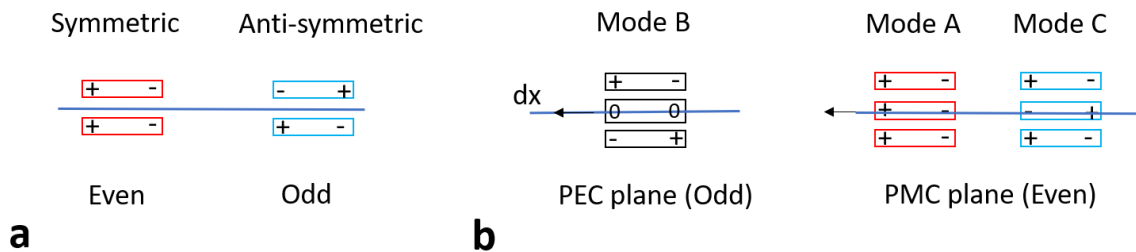


Figure B.1: (a) Schematic depiction of symmetric (even) and anti-symmetric (odd) modes of two-bar system with a bisecting symmetry plane (blue line). (b) Depiction of even (PEC plane) and odd (PMC plane) modes of three-bar system with bisecting symmetry planes (blue lines) for easy analysis.

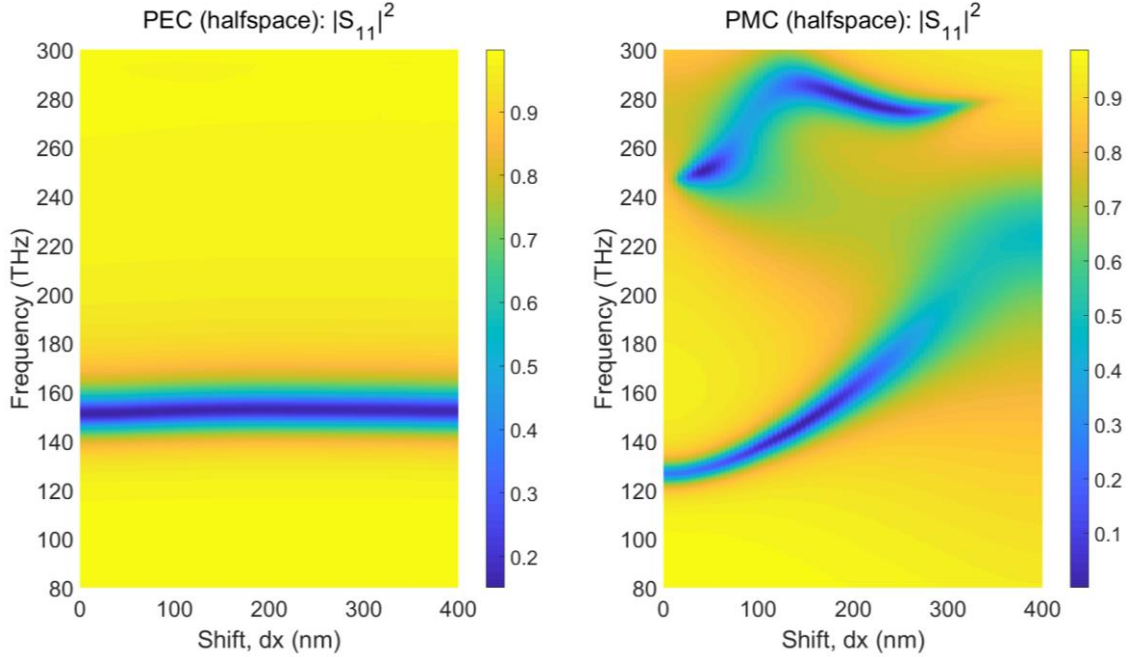


Figure B.2: (left) 1-port reflection, $|S_{11}|^2$, spectra with PEC plane showing odd mode (B) and (right) spectra with PMC plane even modes (A, C, and D) for the three-bar system at $p_x=800$ nm and $d_z=60$ nm. The EP is in the vicinity of a shift, dx , of 345 nm and 212 THz as seen in Figure 3.3 with Modes A and C.

The above half-space (PEC and PMC) 1-port scattering spectra can be combined to yield the full 2-port spectra with the following relationship below [1] which is seen in Figure B.3:

$$S_{11}^{2port} = \frac{1}{2}(S_{11}^{even} + S_{11}^{odd})$$

$$S_{21}^{2port} = \frac{1}{2}(S_{11}^{even} - S_{11}^{odd})$$

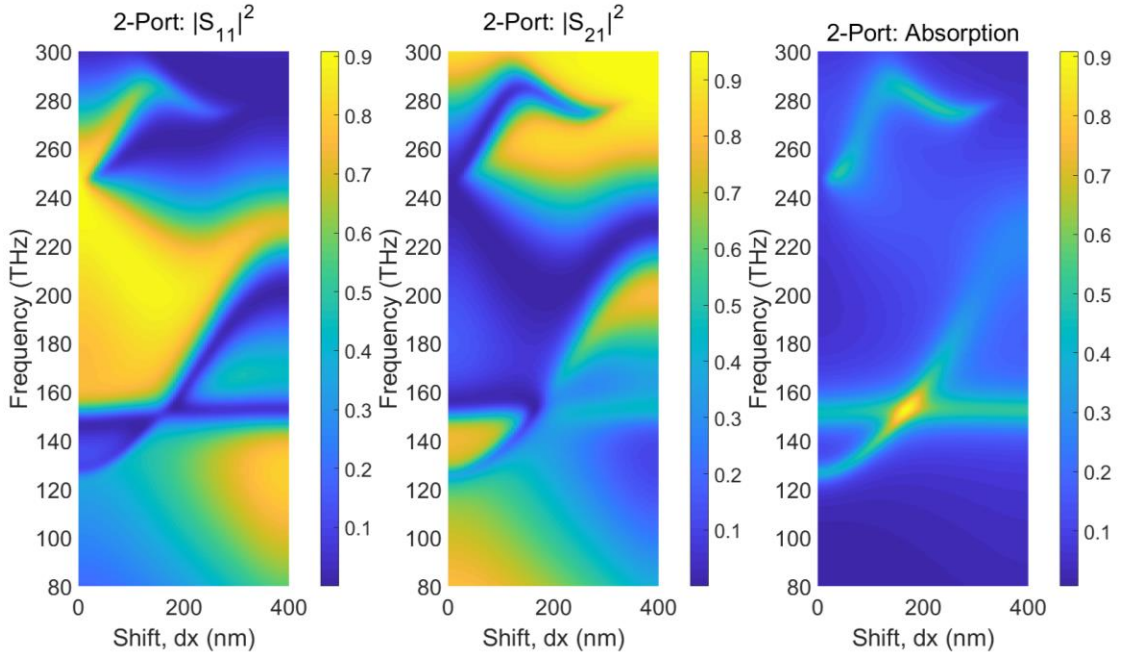


Figure B.3: (left to right) Combined half-space (PEC and PMC) 2-port reflection, $|S_{11}|^2$, transmission, $|S_{21}|^2$, and absorption, $1-|S_{11}|^2-|S_{21}|^2$, spectra as a function of shift, dx , for $p_x=800$ nm and $dz=60$ nm with both visible even and odd modes for three-bar system.

The previous approach is also applied to the five-bar system to isolate either even or odd modes of the systems as seen in Figure B.4 and combined spectra in Figure B.5 below.

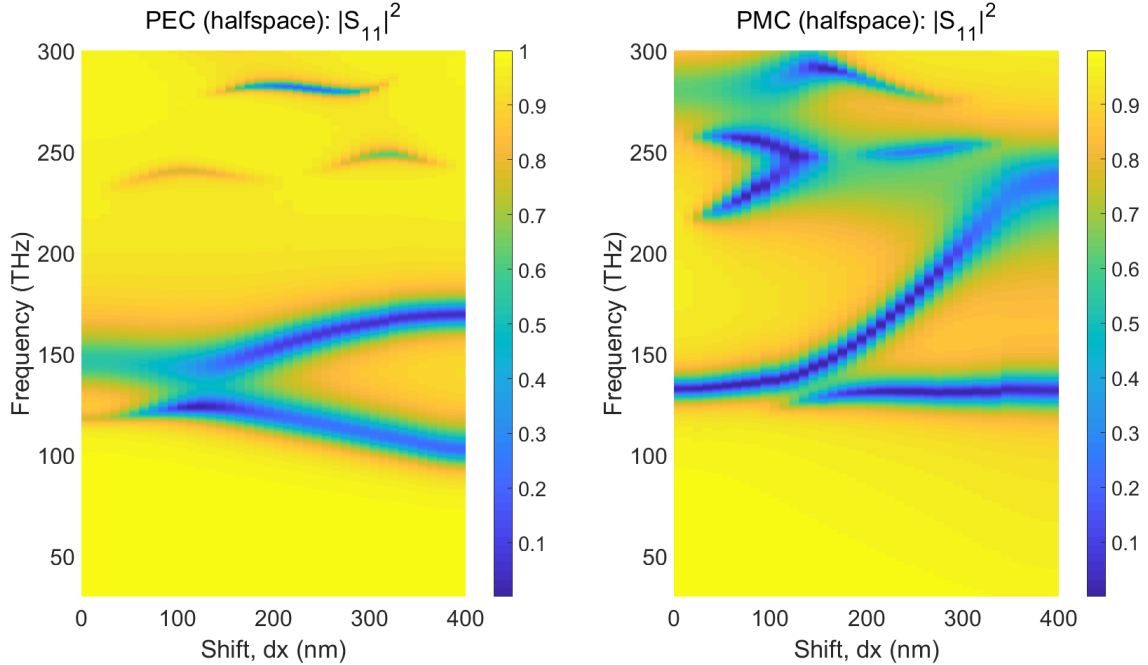


Figure B.4: (left) 1-port reflection, $|S_{11}|^2$, spectra with PEC plane showing two fundamental odd modes and (right) spectra with PMC plane with three fundamental even modes (A, C, and D) for the five-bar system at $p_x=800$ nm and $d_z=40$ nm. The EP is in the vicinity of a shift, dx , of 345 nm and 228 THz as seen in Figure 3.5.

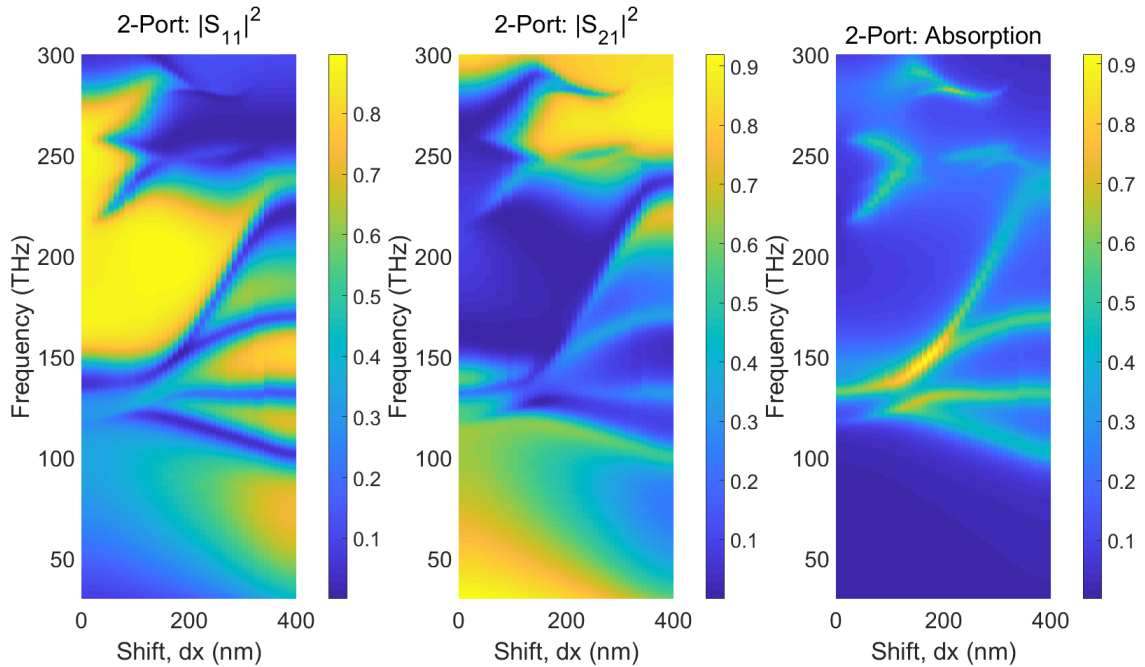


Figure B.5: (left to right) Combined half-space (PEC and PMC) 2-port reflection, $|S_{11}|^2$, transmission, $|S_{21}|^2$, and absorption, $1-|S_{11}|^2-|S_{21}|^2$, spectra as a function of shift, dx , for $p_x=800$ nm and $d_z=40$ nm with both visible even and odd modes for five-bar system.

References

1. J-S. Hong, *Microstrip Filters for RF/Microwave Applications*, New York: Wiley, 2nd Edition, page 20 (2011).

Appendix C (Ch 4)

C.1 Odd and Even Modes

We plot the complex dispersion relation for both odd and even modes (membrane mirror plane), in the wavelength range from 1.45 μm to 1.67 μm , in Figure C.1.

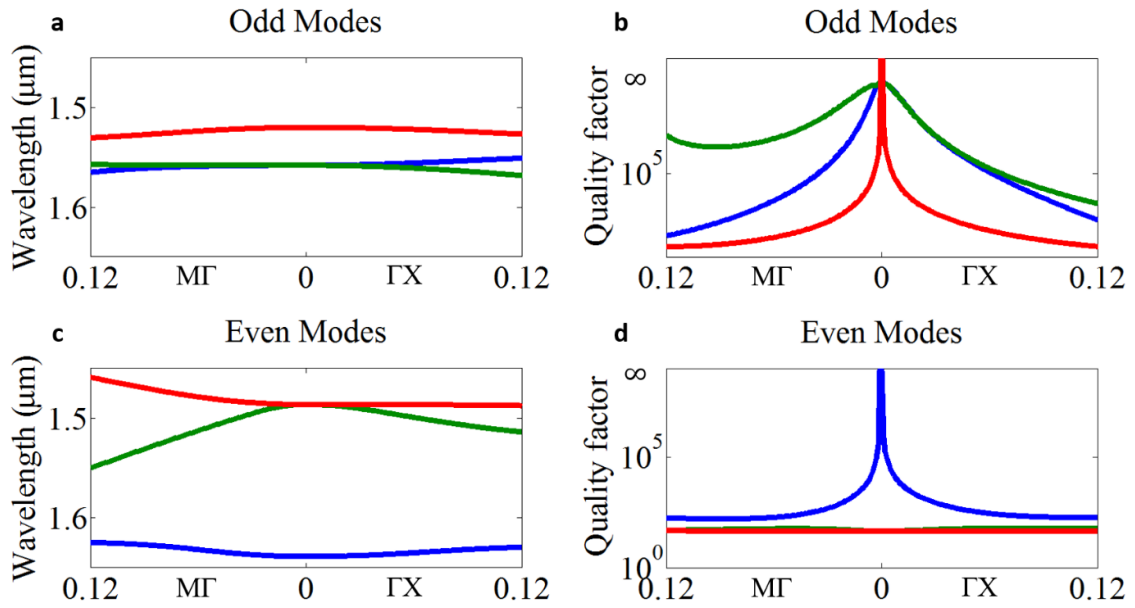


Figure C.1: Complex dispersion relation as function of k ($a/2\pi$) of the structure along $M\Gamma$ and ΓX in the wavelength range from 1.45 μm to 1.67 μm and for a BIC radius of 528.4 nm. Odd modes, (a) Frequency vs. phase (b) Quality factor vs. phase. Even modes, (c) Frequency vs. phase (d) Quality factor vs. phase.

As can be seen, there are three odd modes and three even modes in this wavelength range. No mode has a higher overall quality factor than the two odd modes (doubly degenerate at Γ) around 1.55 μm , which are the BIC modes (Figure C.1b, blue and green lines). In addition, there are two symmetry-protected modes, one odd and one even, whose quality factors are high only at Γ (Figure C.1b, red and Figure C.1d, blue). Finally, there is

a pair of even modes that are degenerate at Γ with a low quality factor (Figure C.1d, red and green).

C.2 Group Theory and Tunable off- Γ BICs

The distinction between the ‘resonance-trapped’ and ‘symmetry-protected’ modes is further evident in the context of group theory [1]. In brief, spatial symmetries of a periodic membrane can be used to classify its modes. The point group of a square-lattice membrane suspended in air is the direct product of point groups C_{4v} and C_{1h} . Accordingly, its modes can be classified using the irreducible representations of both point groups. The two character tables below summarize how each irreducible representation behaves with respect to each symmetry operation.

C_{1h}	E	C_2
A	+1	+1
B	+1	-1

C_{4v}	E	$2C_4$	C_2	$2\sigma_v$	$2\sigma_d$
A_1	+1	+1	+1	+1	+1
A_2	+1	+1	+1	-1	-1
B_1	+1	-1	+1	+1	-1
B_2	+1	-1	+1	-1	+1
E	2	0	2	0	0

There are ten different modes that can exist in such a lattice (two times five). Since we restrict consideration to modes with an odd symmetry with respect to the membrane plane, only five are left: (B, A_1), (B, A_2), (B, B_1), (B, B_2), and (B,E). At Γ , plane waves in free space admit an E representation and can thus only couple to (B,E) modes. Such modes have a low Q-factor on account of their radiative nature. In contrast, all other modes are

uncoupled by virtue of symmetry, *i.e.*, they form symmetry-protected BICs, and thus have an infinite Q-factor. This was first reported by Paddon and Young [2].

Furthermore, (B,A₁), (B,A₂), (B,B₁), and (B,B₂) modes are all singly degenerate while the (B,E) mode is doubly degenerate. In our band diagram (Figure C.1a), we see clearly one singly degenerate mode at 1520 nm and one doubly degenerate mode at 1558 nm. From the above symmetry considerations, we would thus expect only the lower wavelength mode to have an infinite Q-factor. However, we clearly see that this is not the case. This means that the doubly degenerate mode is not a BIC by virtue of symmetry-protection, *i.e.*, it must be a resonance-trapped BIC. Unlike previous works [3, 4], we show here that such BICs do not always happen away from high-symmetry points but can also occur at Γ . As such, our lasing structure fundamentally differs from the work by Bo Zhen *et al.* [5] where lasing originates from a symmetry-protected mode.

Moreover, the “resonance-trapped” BIC exploited in this work can be placed *by design* at either a high-symmetry point, such as the Γ -point, or at a generic point in k-space. In this work, we chose to exploit the BIC at Γ because many applications rely on surface emitting lasers. In this sense, compared to “symmetry-protected” BICs that have to operate at Γ , “resonance-trapped” BICs are more versatile. We show in Figure C. below that the diverging quality factor associated with the “resonantly-trapped” BIC modes (modes 1-2) can be placed off- Γ by choosing a membrane thickness of 290nm, *i.e.*, differing from the current 300nm used to fabricate all our BIC lasers. As seen in Figure C.a, modes 1-2 are the doubly degenerate BIC modes and mode 3 is the symmetry-protected mode. As seen in Figure C.b, for a thickness of 290nm, the diverging Q of the symmetry-protected mode

remains at Γ whereas the diverging Q for modes 1-2 are now off- Γ . For the experiments, this membrane thickness is predefined during the finely controlled epitaxial growth.

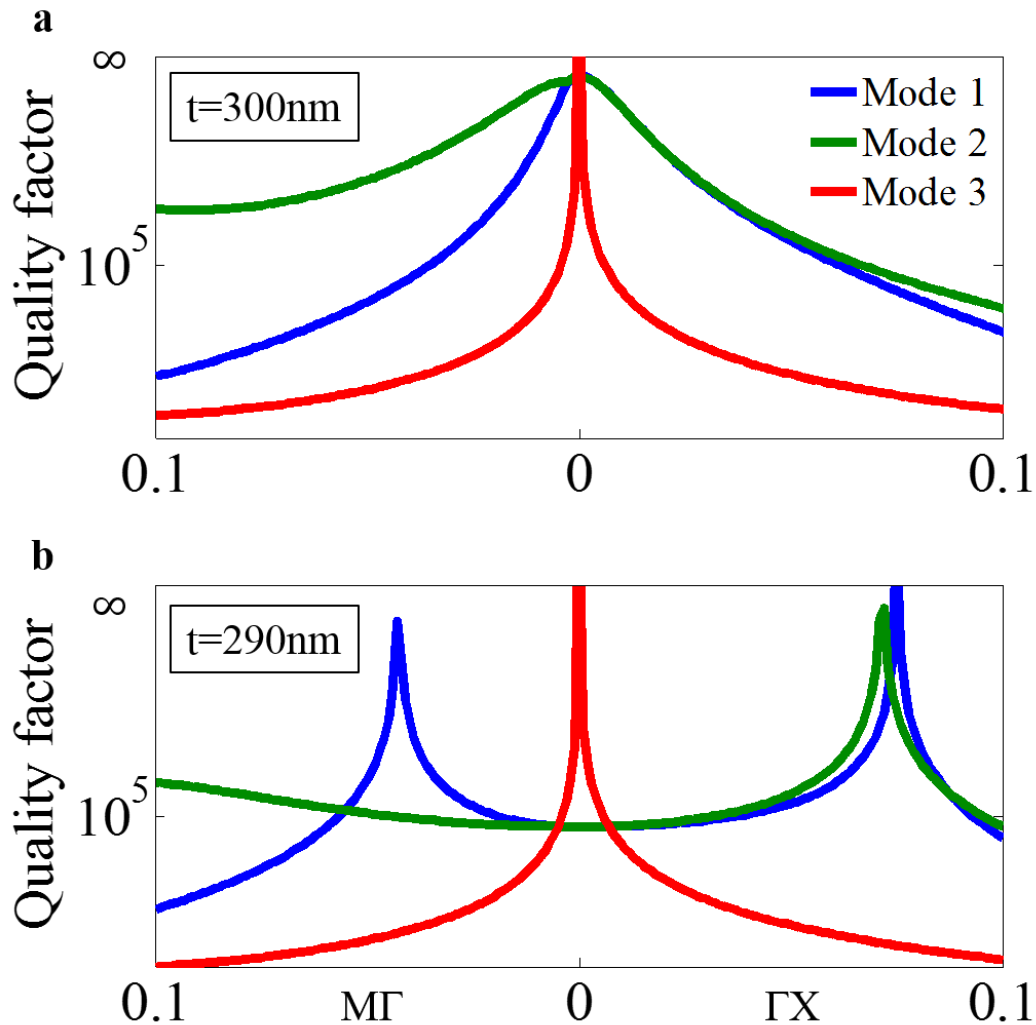


Figure C.2: **a**, Quality factor of modes 1-3 as a function of phase at optimal radius of 528.4 nm and a membrane thickness of 300 nm. **b**, Quality factor as a function of phase for a varied membrane thickness of 290 nm. Modes 1-2 are the doubly degenerate BIC modes and mode 3 is the symmetry-protected mode whose diverging Q remains at Γ whereas the diverging Q for modes 1-2 can be placed off- Γ .

C.3 Far-field Emission and Polarization of BIC Lasers

Figure C.3 shows the calculated normalized far-field intensity profile for the lasing BIC mode with superimposed electric field [6]. The IR CCD images of a suspended laser

array in operation and its corresponding far-field emission can be seen in Figure C.4 and Figure C.5. The pump beam neatly overlaps the laser array (Figure C.4b) and the resulting emission collected over the camera bandwidth is presented in Figure C.4c. Far-field emission of the laser array operating above threshold is filtered around the lasing wavelength using a bandpass filter (FWHM of 40nm) as seen in Figure C.5. Here, a bandpass filter with a FWHM of 40nm is utilized so as to only collect emission around the lasing wavelength and to avoid camera saturation. The emission profile is more prominent as the pump power is increased. The non-uniform pattern is partly a consequence of back reflections from the etched substrate below the laser array (*i.e.*, V-groove etch pit as seen in Figure C.6). Light emitted towards the bottom is reflected by the V-groove once or several times before passing through the suspended membrane. This leads to scattering in other directions and contributes to the experimentally observed far-field. Moreover, the finiteness of the array also leads to some in-plane emission.

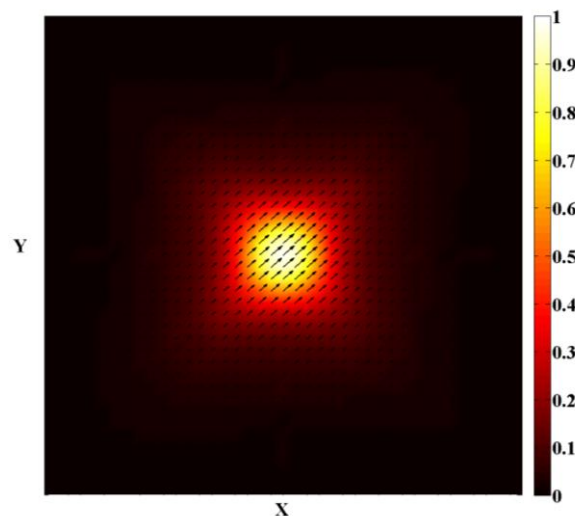


Figure C.3: Normalized far-field intensity profile for the lasing BIC mode with superimposed electric field.

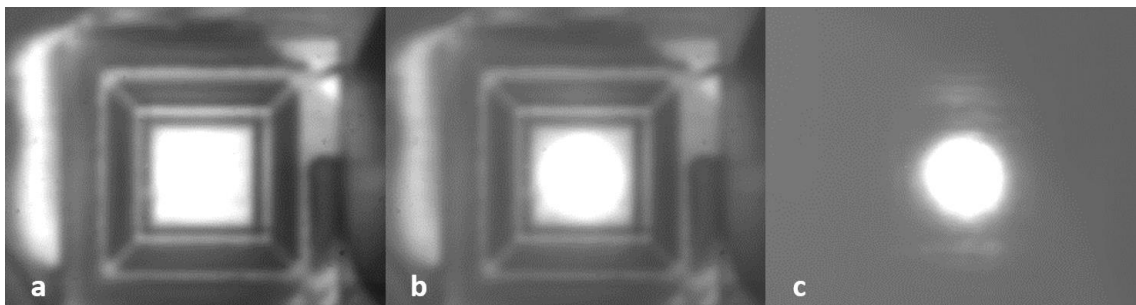


Figure C.4: (a) IR CCD image of suspended laser array. (b) Image of the array with overlapping pump beam. (c) Image of emission from the laser array collected over the camera bandwidth.

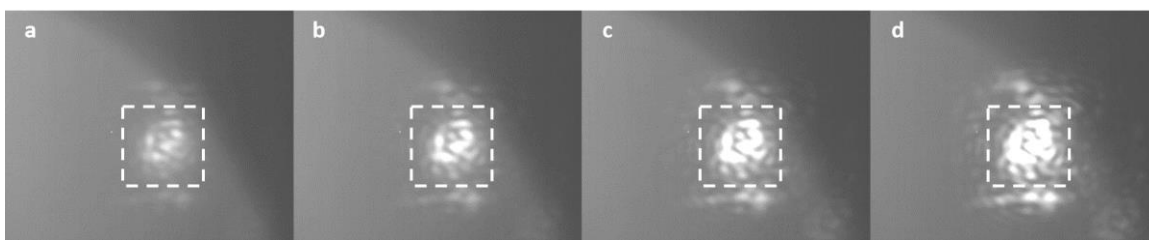


Figure C.5: Far-field emission of laser array over multiple pump powers with dotted outline indicating the physical size and location of the array. Emission profiles of lasers operating above threshold with increasing pump power: (a) $82 \mu\text{W}$, (b) $98 \mu\text{W}$, (c) $111 \mu\text{W}$, (d) $135 \mu\text{W}$.

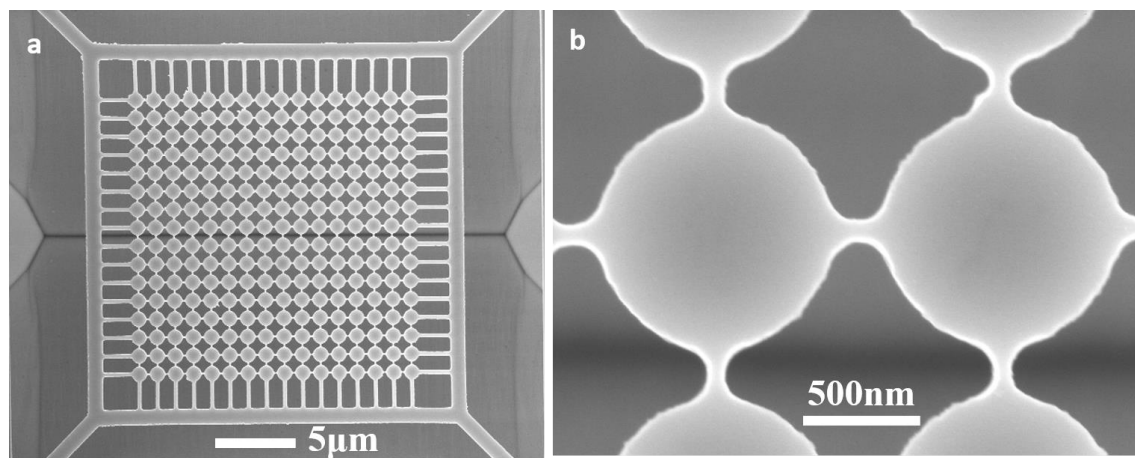


Figure C.6: (a) Electron micrograph image of a fully suspended membrane structure with 16×16 cylindrical resonators interconnected by a network of bridges with a visible etch pit in the InP substrate [7] and large openings for easy membrane release. (b) Zoom-in image of two cylinders at the center of the array.

As further identification of the lasing mode, we have conducted polarization measurements of our laser arrays operating above threshold (see Figure C.7 below). There

is agreement between the measured and calculated polarization ellipses as seen in Fig. Figure C.7b and c. There is observable pinching in the measured ellipse corresponding to the predicted polarization ellipse. Note that the predicted ellipse does not account for the finiteness of the laser array. Furthermore, experimentally one of the degenerate modes wins mode competition and lases. Modes 1-2 are degenerate at Γ for infinitely large samples. Individually, the polarization ellipses for each of the two modes are orthogonal. Ideally, without imperfections, the two modes would be truly degenerate; thus the resulting polarization ellipse from the laser emission would be a circle.

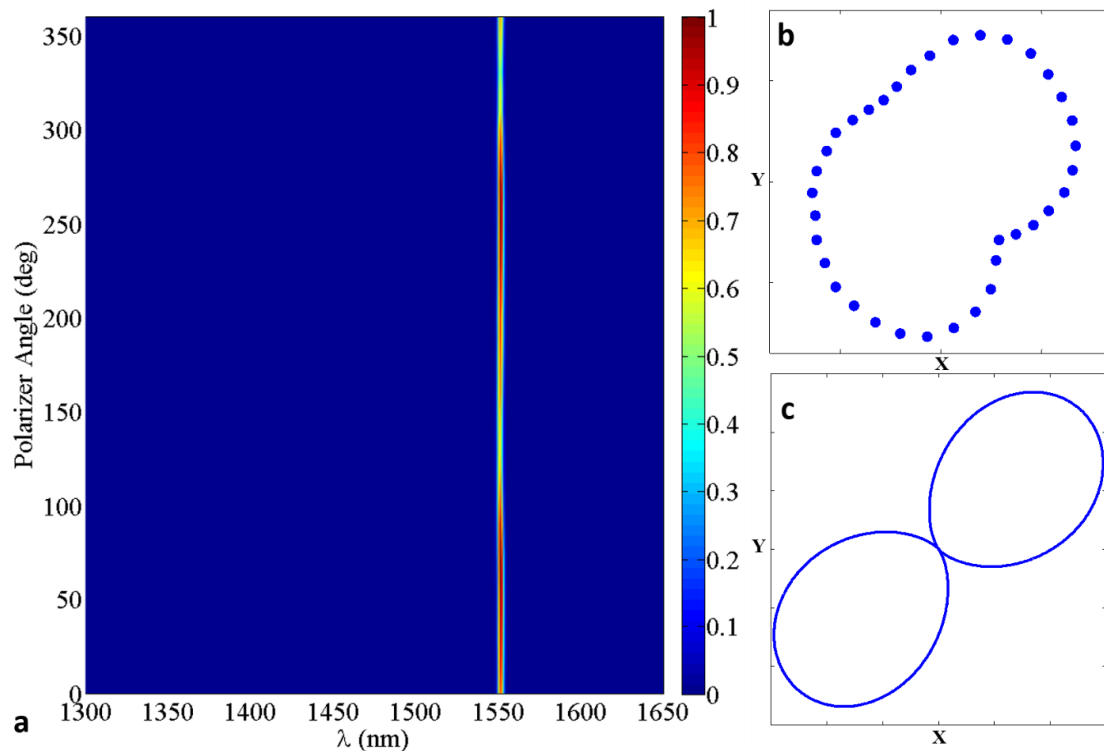


Figure C.7: Polarization measurement of laser operating above threshold. (a) Photoluminescence spectra of a 16-by-16 laser array with a nanoresonator radius of 525 nm as a function of the polarizer angle. (b) Measured polarization ellipse and (c) predicted polarization ellipse not accounting for the finiteness of the lasing array. There is observable pinching in the measured ellipse corresponding to the ideal polarization ellipse.

C.4 Emission Power Estimate

We have carried out additional measurements for a quantitative estimate of the emission power from our laser devices. In our case, the pump laser is pulsed with a 12 nSec pulse width at $f=300$ kHz (period $\approx 3\mu$ Sec) in conjunction with a 1 kHz chopper reference for the lock-in amplifier. Hence, the emission from our laser devices is also emitting with a 300 kHz repetition rate with a 1 kHz modulation. However, the present photodiode detector has a bandwidth of 2 kHz with a single pole roll-off (-20 dB/dec) in its frequency response which is far shorter than the 300kHz repetition rate (see Figure C.8a and b below). Consequently, the power estimated while compensating for the single pole roll-off is an indirect measurement (see Figure C.8 below).

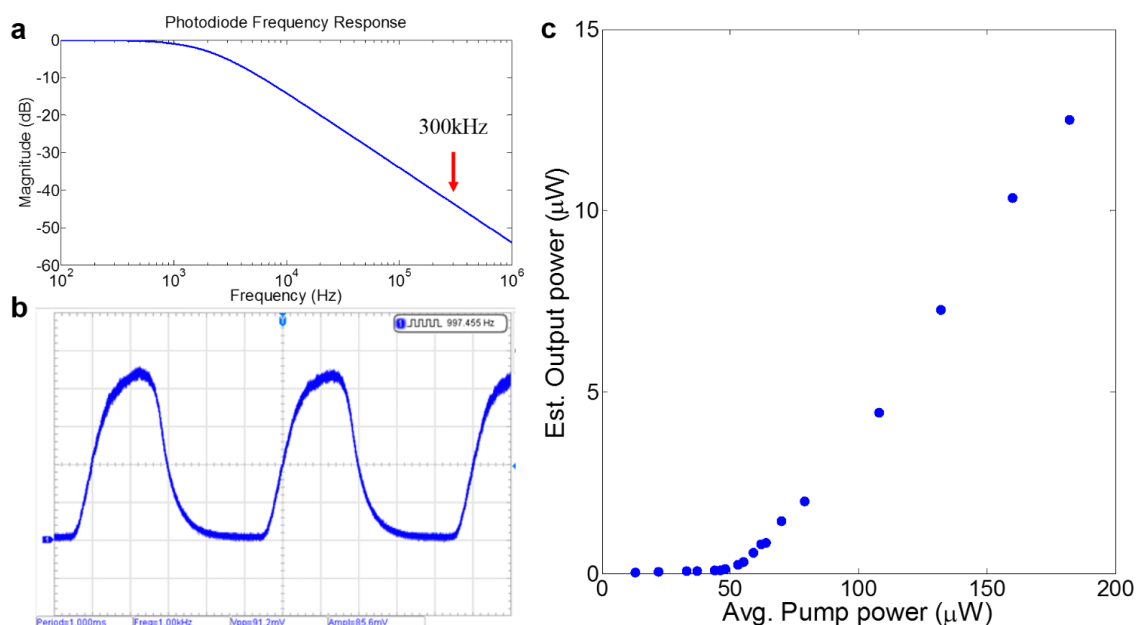


Figure C.8: (a) Normalized single-pole frequency response of the photodiode detector with a red arrow indicating the repetition rate of 300 kHz which is outside the 2kHz bandwidth of the detector. (b) Laser emission recorded off the photodiode where the 1kHz reference for lock-in amplifier is apparent but the higher frequency signal of 300kHz is not present. (c) Estimated emission power of laser device (R525 16x16) in the micro-watt range as a function of average pump power.

Appendix C, in part, is a reprint of the material as it appears in the supplement of A. Kodigala, T. Lepetit, Q. Gu, B. Bahari, Y. Fainman and B. Kanté, "Lasing action from photonic bound states in the continuum," *Nature* **541**, 196 (2017). The dissertation author was the primary researcher and author of this paper.

References

1. K. Sakoda, *Optical Properties of Photonic Crystals*, 2nd Edition, Springer (2005).
2. P. Paddon and J. F. Young, "Two-dimensional vector-coupled-mode theory for textured planar waveguides," *Phys. Rev. B* **61**, 2090 (2000).
3. C. W. Hsu, B. Zhen, A. D. Stone, J. D. Joannopoulos, and M. Soljacic, "Bound states in the continuum," *Nat. Rev. Mater.* **1**, 16048 (2016).
4. C. W. Hsu, B. Zhen, J. Lee, S-L. Chua, S. G. Johnson, J. D. Joannopoulos, and Marin Soljacic, "Observation of trapped light within the radiation continuum," *Nature* **499**, 188-191 (2013).
5. B. Zhen, S-L. Chua, J. Lee, A. W. Rodriguez, X. Liang, S. G. Johnson, J. D. Joannopoulos, M. Soljacic, and O. Shapira, "Enabling enhanced emission and low-threshold lasing of organic molecules using special Fano resonances of macroscopic photonic crystals," *Proc. Natl. Acad. Sci.* **110**, 13711-13716 (2013).
6. C. A. Balanis, *Antenna Theory: Analysis and Design*, 3rd Edition, Wiley (2005).
7. K. Srinivasan, P. E. Barclay, and O. Painter, "Fabrication of high-quality-factor photonic crystal microcavities in InAsP/InGaAsP membranes," *J. Vac. Sci. Technol. B* **22**, 875 (2004)